A Thesis for the Degree of Ph.D. in Science

Magnetic resonance of bismuth donors in silicon detected by spin dependent recombination

August 2014

Graduate School of Science and Technology

Keio University

Pierre-André Mortemousque

Pour mon oncle, Marc.

À ma famille.

Pour Jean-Claude et Béatrice.

Abstract

Realization of quantum information processing devices including quantum computers is one of the most highlighted projects physicists are pursuing today. When realized, quantum computers will be composed of multiple elements such as processors, memories, communication lines, etc. just like today's computers. While superconducting qubits are excellent candidates as quantum processors, hydrogenic donors in silicon are considered very promising as quantum memory qubits. Among them, bismuth (Bi) donors in silicon are important since they demonstrate long coherence (quantum memory) time and, in the low enough magnetic field needed by the superconducting qubits to operate, the energy separation between $|0\rangle$ and $|1\rangle$ states is compatible with that of superconducting qubits making them connectible to each other.

The present thesis shows the successful manipulation and the electrical detection of Bi donor spins in silicon at arbitrarily chosen magnetic fields, establishing a novel way to readout electron and nuclear spins of Bi in the zero-field limit. Moreover, the hyperfine clock transitions of Bi that are extremely robust against external electric field noise are identified experimentally for future applications to quantum memories.

The present thesis is composed of six chapters. Chapter 1 introduces the motivation of the research. Chapter 2 describes the basics of spin systems utilized in this work. Chapter 3 summarizes the experimental techniques including sample preparations and measurements. Chapter 4 describes the low-field ($6 - 110$ mT) magnetic resonance spectroscopy of Bi in silicon. It is performed by monitoring the change in photoconductivity of the sample induced by the spin dependent recombination. Spectra at various resonance frequencies show signal intensity distributions drastically different from those observed by the conventional electron paramagnetic resonance spectroscopy. A theoretical model considering the recombination rates for

the forty possible combinations of spin states of a pair of a Bi donor and a paramagnetic recombination center is shown to describe the experimental observation well. Moreover, excellent tunability of the Bi excitation energy for the future coupling with superconducting qubits at low fields is demonstrated. Chapter 5 presents comparison of Bi spectra in ^{28}Si and ^{nat}Si crystals. The hyperfine clock transition, at which the linewidth is significantly narrowed, is observed. The experimental results are modeled quantitatively by the effect of hyperfine and Zeeman interactions in the context of molecular orbital theory for the pair of a Bi donor and a spin dependent recombination center. Chapter 6 provides summary and outlook.

Acknowledgements

It has been nearly five years spent in Itoh group and I would like to acknowledge of the people who directly or indirectly contributed to the completion of this thesis.

I sincerely thank my supervisor Professor Kohei M. Itoh for giving me an opportunity to pursue this work under his guidance and for the fruitful discussions that we had on the topics related to this work. His useful comments and criticisms has certainly helped me in becoming a better researcher and motivated me to keep the pace of my research. He was the person without his support, it would have been nearly impossible to achieve this feat. The second person who comes to mind when I talk about my guidance in my Ph.D. is certainly Dr. Takeharu Sekiguchi. My interaction with him really helped me in understanding my research and get some exciting results.

I would also like to thank Dr. Jaw Shen Tsai and Dr. Fumiki Yoshihara from NEC for my stay in their laboratory and teaching me the basics of superconducting flux qubit technology.

My deepest thanks to Dr. John J. L. Morton and Gary Wolfowicz for their warm welcome in London, and for our exciting discussions about our on going quantum error correction project.

I am really thankful to the Professor Hayase, Professor Ohta and Professor Yamamoto for reviewing this research work and for their kind comments for improving this thesis.

I would like to thank Aizawa-san for her unconditional support as well as Kuroda-san for his invaluable help. I also would like to thank Prof. Uematsu for his help while performing ion implantation simulations.

My special thanks to Prof. Leonid S. Vlasenko and his wife Dr. Marina P. Vlasenko for teaching me the basis of electron spin resonance and spin dependent

recombination techniques.

I would like to acknowledge Dr. Toyofumi Ishikawa and Katsuhiko Naito for guiding me during the first period of my stay in Japan, and also for teaching me the experimental techniques used in photoluminescence studies.

Although few of the group members were directly involved in my project, their research activities, spirits, and other right things affected me in several ways, and all the other past and present group members are worthy of acknowledgements. I sincerely acknowledge the support from the laboratory members namely, Dr. Satoru Miyamoto, Dr. Toyofumi Ishikawa, Dr. Mohammad Waseem Akthar, Dr. Hiroki Morishita, Dr. Mohammad Rizwanur Rahman, Dr. Yoko Kawamura, Dr. Rii Hirano, Dr. Shinchan Hong Agung, Alain Truong, Michihiro Yamada, Michihisa Tanaka, Taiga Isoda, Hiroki Tezuka, Katsuhiko Naito, Go Tsuchiya, Takashi Matsuoka, Erika Kawakami, Itaru Arikawa, Fangfang Yang, Eri Sato, and Hajime Shinohara.

One person who has always been very helpful, supportive, and really entertainer is Alain Truong, a Ph.D. candidate. I wish him and all others the best for their future endeavors.

Contents

Chapter 1

Introduction

Ever since Richard Feynman proposed the idea of a quantum computer in 1982, the progress made in the field of quantum information is astonishing. The work presented in this thesis is a building block for understanding of the quantum phenomena for the realization of quantum information devices.

1.1 Background

Since the work of Shor on the quantum factorization of large prime numbers [1] and the work of Grover on the search algorithm for large unstructured data sets [2], research in quantum information processing has witnessed a fabulous rise. This formidable enthusiasm was triggered by the development of fault-tolerant algorithm [3] that has relaxed the very demanding constrains on the physical quantum information devices. The original idea of Feynman was to realize a quantum computer that could solve mathematical problems unsolvable by any of its classical counterpart by making use of non-classical bits referred to as quantum bits (qubits). The subsequent exponential speed-up provided by quantum algorithms [4] is made possible by the use of two typically non-classical phenomena: the quantum parallelism and the entanglement [5].

1.1.1 Hybrid quantum computers

The long path towards the realization of a fault-tolerant quantum computer can be divided into several steps, each one of them requiring the mastery of the previous ones. The first two steps together are the so-called DiVicenzo criteria [6]. First, a quantum system defined as the qubit needs to hold one piece of quantum information long enough for it to be written, manipulated and read out without alteration [7, 8, 9]. Naturally, the second step consists in scaling up this system in order to implement quantum algorithms on multiple physical qubits. The third step is about reinforcing the *robustness* of the qubits against the loss of the quantum information. This is done by encoding the logical qubit into n physical qubits. Then, quantum error correction codes [3, 10, 11] can actively protect the information of the logical qubits.

The proof-of-concept of the quantum error correction code has been recently achieved in diamond with 3+1 qubits. Here, the three physical qubits are ^{13}C and ^{14}N nuclear spins and they are coupled with the electron spin of a negatively charged nitrogen-vancacy center in diamond [NV^-] [12]. Among these correction techniques lies the quantum feedback correction of a qubit, that forces a qubit to stay in an arbitrarily defined, even dynamical, state. It has been demonstrated in the past three years for several systems such as Rydberg atoms [13], trapped ions [14], and superconducting qubits [15, 16, 17].

The concept of a hybrid quantum computer is born from the need to combine quantum systems of different natures to make use of their respective qualities (processing speed, scalability, coherence time, etc . . .). In the following, I will describe the architecture of a hybrid quantum computer that combines the relatively long coherence time and scalability of the transmon superconducting qubits (section 1.1.1) and the exceptionally long coherence time of the electron and nuclear spins of bismuth donors in silicon (section 1.1.2).

The transmon superconducting qubits make use of *dissipationless* classical electric components such as capacitors and inductors, and of a non-classical non-linear inductors known as the Josephson junctions [18]. While electrical circuits are restricted to harmonic oscillators in the "classical" world, the non-linearity of the Josephson junction shifts some of the degenerate transition energies of the harmonic oscillator. This property leads to a finite number of anharmonic states that can be isolated and used as qubits. The transmon qubit is characterized by a large ratio of the charging energy to the Josephson energy E_C/E_J, designed to reduced the sensitivity of the qubit to the charge noise.

Using such performant qubits, a primitive version of the von-Neumann architec-

ture [19], the implementation of the three-qubit Toffoli gate [15, 20] and the deterministic teleportation [21] have been demonstrated. Even small quantum algorithms such as the Deutsch-Jozsa algorithm [22, 23], Shor's prime number factorization [24] and quantum error corrections [15] were implemented.

For quantum information processing, one of the most challenging tasks is to hold the very volatile quantum coherence onto the physical qubits. Therefore, maintaining the quantum coherence lies at the heart of current research. The state-of-the-art superconducting qubits, in terms of coherence time and number of realizable operations per qubit coherence time and lifetime, is the transmon type, coupled to a three-dimensional cavity [25]. They exhibit coherence times as long as $T_2^* = 92$ μs and lifetimes of $T_1 = 70$ μs. This transmon qubit + 3D cavity outclasses the original designs of coplanar transmon [26], fluxonium [27], circuit quantum electro-dynamics [28], and quantronium [29] qubits by at least one order of magnitude when comparing the coherence times.

Even with these great improvements made on the Cooper pair box system [7], the figure-of-merit of the desired number of operation per qubit lifetime of 10^4 [30] is not yet achieved. A very promising alternative to this coherence time challenge is currently under investigation by several research groups around the world. It consists of coupling a superconducting circuit to either a single spin or to an ensemble of spins hosted by a solid state system. The physical qubits can be of different nature, such as the electrons of erbium ions in YSO [31, 32, 33], the electrons spins of a NV^- [34, 35, 36, 37] or donor spins in silicon [38, 5, 39, 40]. Moreover, the realization of a holographic quantum register using a mesoscopic ensemble of spins has been proposed by Tordrup *et al* [41] and has been achieved in a $N@C_{60}$ sample by Wu *et al* [42]. This opens up the way for storage of multiple pieces of quantum

information in a single ensemble of electron and nuclear spins. An example of the holographic quantum register coupled to four transmon superconducting qubits via a superconducting resonator is shown in Fig. 1-1.

1.1.2 Donor spins in silicon as quantum memories

During the past half century, silicon based electronic devices have dominated the classical microelectronic technology. In parallel to this remarkably fast development, it has become more and more evident that silicon can also be a host material for quantum information devices. The two main reasons for this are its weak spin-orbit coupling and the existence of nuclear spin free silicon isotopes, leading to extremely long coherence time of electron and nuclear spins [43, 40].

There are four elements among group V donors in silicon: ^{31}P, ^{75}As, ^{121,123}Sb and ^{209}Bi. Phosphorus (P) was the first element of the group V donors to be studied for applications in quantum information devices. At low enough temperature ($\lesssim 5$ K), the electron-phonon coupling becomes negligible and the electron spin coherence time of an ensemble of phosphorus donors, written $T_{2e}(P)$, becomes independent of the host crystal temperature [43]. In this regime, $T_{2e}(P)$ depends on the relative orientation of the static magnetic field and the crystal axes. It ranges from 200 μs for $\vec{B}//[111]$ to 330 μs for $\vec{B}//[100]$ [44]. As it is possible to coherently transfer quantum information between the donor electron spin and its nuclear spin, one can make use of the much longer coherence time of the nuclear spin $I = 1/2$ of phosphorus $T_{2n}(P) =$ 1.2 s. These coherence times are limited by the presence of ^{29}Si nuclear spins naturally present in Si [45, 46]. As Si has nuclear spin free isotopes (see Table 1.1), researchers have used isotopically purified silicon samples to reach even longer coherence times. In ^{28}Si, electron spin coherence time as long as $T_{2e}(P) = 20$ ms [43], and nuclear spin

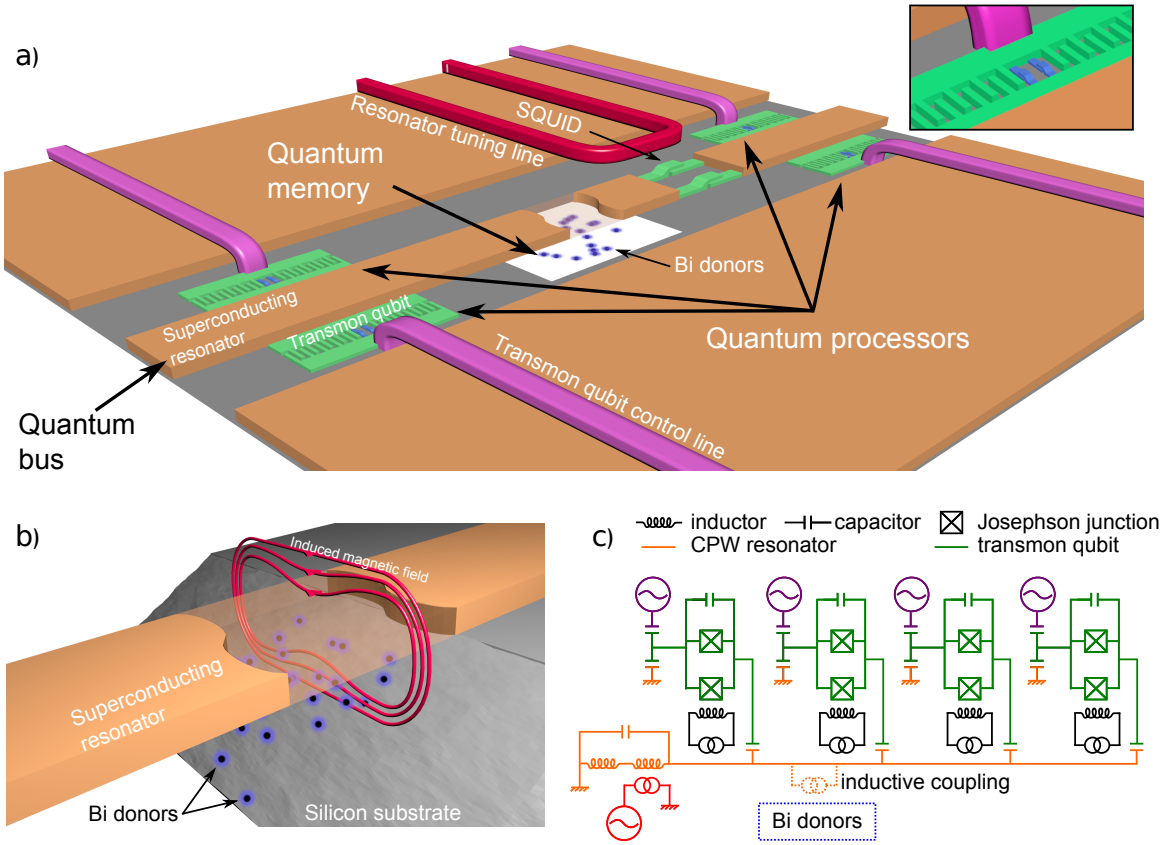

Figure 1-1: (a) Schematic representation of a single coplanar waveguide (CPW) resonator (inner orange line) coupled to four transmon qubits. The center frequency of the resonator can be tuned by adjusting the magnetic field going through the superconducting quantum interference device (SQUID, in green in the central line), used as an adjustable inductor. The large capacitor of the transmon qubits (interdigitated) is represented in green, and the Josephson junctions are represented in blue. The purple lines are the control lines capacitively coupled to each superconducting qubit. The Bi donors are represented by blue points and the Bi doped silicon region is represented in white. The inset is an enlarged view of the central part of a transmon qubit, in which the two Josephson junctions are represented in blue. The schematic representation of magnetic coupling between the Bi donors and the superconducting resonator is shown in (b): the magnetic field flux (red lines) generated by the microwave photon in the CPW resonator can induce the magnetic dipole transition of the Bi donors spins. The static magnetic field $B_z < 50$ Oe (see section 1.1.3) is not represented. (c) Schematic of the equivalent circuit shown in (a).

Table 1.1: Natural abundance of the three different silicon isotopes, with their respective nuclear spin I and gyromagnetic ratio.

	^{28}Si	^{29}Si	^{30}Si
^{nat} isotopic composition	92.2 %	4.7 %	3.1 %
Nuclear spin	$I = 0$	$I = 1/2$	$I = 0$
Gyromagnetic ratio		-8.4655 MHz/T	

coherence time of ionized P $T_{2n}(P^+) = 27$ s at 1.9 K and $T_{2n}(P^+) = 8$ s at room temperature [40] have been measured using the conventional two-pulse Hahn echo.

1.1.3 Advantages of bismuth donors in silicon as quantum memories

The bismuth donor in silicon is the deepest of the group V shallow donors in silicon. It has a remarkably large hyperfine interaction between its electron and nuclear ($I = 9/2$) spins. This makes the electron spin resonance (ESR) frequency of bismuth donors $\approx$ 7.5 GHz similar to the operating frequency of superconducting qubits in their operatable magnetic field regime (below 50 Oe for aluminum superconducting qubits [47, 48]). This unique coincidence has attracted much attention on the possibility to couple superconducting circuits to bismuth donors in silicon [49, 50].

In addition to the potential coupling with a superconducting circuit, the electron spin resonance of bismuth donors in the microwave regime ($5 \sim 10$ GHz) presents a *low field* behavior, in which the hyperfine coupling of the donor is equivalent or larger than the Zeeman energy of both the electron and nuclear spins. In this low field regime, the existence of clock transitions (CTs), where the electron spin resonance frequency is insensitive to the static magnetic field and to magnetic field fluctuations caused by other donor spins, has been demonstrated. At these CTs, the already long

electron spin coherence time becomes even longer: Wolfowicz *et al* [51] have measured using the conventional two-pulse Hahn echo bismuth donor electron coherence times as long as $T_{2e}(Bi) = 93$ ms in ^{nat}Si and $T_{2e}(Bi) = 2.7$ s in ^{28}Si .

1.1.4 Possible quantum computer architecture

When considering a quantum computer with a vast number of qubits, the sheer space needed to accommodate the quantum computer becomes an issue. Recently, a qubit-resonator system has been designed in a space of 400×800 μm [52]. This miniaturization makes the electrical control lines very close the the spin ensemble (see Fig. 1-1). The long range electric field generated by such lines [53, 54, 55, 56, 57, 58, 59], together with inevitable strain at the substrate surface [60], may cause fluctuations in the bismuth donor hyperfine coupling, causing decoherence in the spin memory. Therefore, in this work, we have undertaken the objective of characterizing the bismuth donor spins sensitivity to such fluctuations in effective electric field.

1.2 Organization of this thesis

Chapter 1 provides the background and the motivation for the research presented in this thesis. This is followed by a general description of the spin properties of group V donors in silicon.

Chapter 2 introduces the basics of solid state physics required for the description of energy levels of bismuth in silicon. I also discuss the fundamentals of the donor spin Hamiltonians.

Chapter 3 presents the experimental techniques and sample preparation used in this work.

Chapter 4 and 5 focus on the main results of this thesis.

Chapter 4 discusses the magnetic resonance detection based on the spin dependent recombination (SDR) of a bismuth donor electron in silicon. I show that with the creation of crystal defects during the ion implantation of bismuth ions into silicon, it is possible to probe the spin state of bismuth atoms using SDR spectroscopy. The unique spin properties of bismuth make it possible to study its low field SDR detection at X-band in a conventional ESR spectrometer. Furthermore, we reveal that the dipolar interaction between the readout centers and the bismuth electron spins leads to the demonstration of the SDR detection of cross relaxation signals in silicon.

Chapter 5 is devoted to the study of the hyperfine clock transitions (HCT) of bismuth donors in silicon. First, the SDR spectroscopies of bismuth donors in ^{28}Si and in ^{nat}Si demonstrate the existence of such HCT where the sensitivity to the effective electric field perturbations is minimized. Then, the experimental results are modeled quantitatively by molecular orbital theory for a coupled pair consisting of a bismuth donor electron and the electron of the readout center.

Chapter 6 is the summary of the present thesis.

Bibliography

[1] P. W. Shor, J. Sci. Stat. Comput. **26**, 1484 (1997). (Cited on pages 2.)

[2] L. K. Grover, in ACM, editor, "28th Annual ACM Symposium on the Theory of Computing (STOC)," page 212. (Cited on pages 2.)

[3] P. W. Shor, Phys. Rev. A **52**, R2493 (1995). (Cited on pages 2.)

[4] R. Van Meter and K. M. Itoh, Phys. Rev. A **71**, 052320 (2005). (Cited on pages 2.)

[5] S. Simmons, R. M. Brown, H. Riemann, N. V. Abrosimov, P. Becker, H. J. Pohl, M. L. W. Thewalt, K. M. Itoh, and J. J. L. Morton, Nature **470** (2011). (Cited on pages 2 and 4.)

[6] D. DiVincenzo, Fortschr. Phys. **48**, 771 (2000). (Cited on pages 2.)

[7] Y. Nakamura, Y. A. Pashkin, and J. S. Tsai, Nature **398**, 786 (1999). (Cited on pages 2 and 4.)

[8] J. E. Mooij, T. P. Orlando, L. Levitov, L. Tian, C. H. van der Wal, and S. Lloyd, Science **285**, 1036 (1999). (Cited on pages 2.)

[9] I. Chiorescu, Y. Nakamura, C. Harmans, and J. E. Mooij, Science **299**, 1869 (2003). (Cited on pages 2, 46, and 65.)

[10] A. Steane, Proc. R. Soc. London Ser. A **452**, 2551 (1996). (Cited on pages 2.)

[11] E. Knill and R. Laflamme, Phys. Rev. A **55**, 900 (1997). (Cited on pages 2.)

[12] G. Waldherr, Y. Wang, S. Zaiser, M. Jamali, T. Schulte-Herbruggen, H. Abe, T. Ohshima, J. Isoya, J. F. Du, P. Neumann, and J. Wrachtrup, Nature **506**, 204 (2014). (Cited on pages 3.)

[13] C. Sayrin, I. Dotsenko, X. Zhou, B. Peaudecerf, T. Rybarczyk, S. Gleyzes, P. Roucon, M. Mirrahimi, H. Amini, M. Brune, J. M. Raimond, and S. Haroche, Nature **477**, 73 (2011). (Cited on pages 3.)

[14] P. Schindler, J. T. Barreiro, T. Monz, V. Nebendahl, D. Nigg, M. Chwalla, M. Hennrich, and R. Blatt, Science **332**, 1059 (2011). (Cited on pages 3.)

[15] M. D. Reed, L. DiCarlo, D. Nigg, L. Y. Sun, L. Frunzio, S. M. Girvin, and R. J. Schoelkopf, Nature **482**, 382 (2012). (Cited on pages 3 and 4.)

[16] D. Riste, C. C. Bultink, K. W. Lehnert, and L. DiCarlo, Phys. Rev. Lett. **109**, 240502 (2013). (Cited on pages 3.)

[17] P. Campagne-Ibarcq, E. Flurin, N. Roch, D. Darson, P. Morfin, M. Mirrahimi, M. H. Devoret, F. Mallet, and B. Huard, Phys. Rev. X **3**, 021008 (2013). (Cited on pages 3.)

[18] B. D. Josephson, Phys. Lett. **1**, 251 (1962). (Cited on pages 3.)

[19] M. Mariantoni, H. Wang, T. Yamamoto, M. Neeley, R. C. Bialczak, Y. Chen, M. Lenander, E. Lucero, A. D. O'Connell, D. Sank, M. Weides, J. Wenner, Y. Yin, J. Zhao, A. N. Korotkov, A. N. Cleland, and J. M. Martinis, Science **333** (2011). (Cited on pages 4.)

[20] A. Fedorov, L. Steffen, M. Baur, M. P. da Silva, and A. Wallraff, Nature **481**, 170 (2012). (Cited on pages 4.)

[21] L. Steffen, Y. Salathe, M. Oppliger, P. Kurpiers, M. Baur, V. Lang, C. Eichler, G. Puebla-Hellmann, A. Fedorov, and A. Wallraff, Nature **500**, 319 (2013). (Cited on pages 4.)

[22] L. DiCarlo, J. M. Chow, J. M. Gambetta, L. S. Bishop, B. R. Johnson, D. I. Schuster, J. Majer, A. Blais, L. Frunzio, S. M. Girvin, and R. J. Schoelkopf, Nature **460**, 240 (2009). (Cited on pages 4.)

[23] A. Dewes, R. Lauro, F. R. Ong, V. Schmitt, P. Milman, P. Bertet, D. Vion, and D. Esteve, Phys. Rev. B **85**, 140503(R) (2012). (Cited on pages 4.)

[24] E. Lucero, R. Barends, Y. Chen, J. Kelly, M. Mariantoni, A. Megrant, P. O'Malley, D. Sank, A. Vainsencher, J. Wenner, T. White, Y. Yin, A. N. Cleland, and J. M. Martinis, Nat. Phys. **8** (2012). (Cited on pages 4.)

[25] C. Rigetti, J. M. Gambetta, S. Poletto, B. L. T. Plourde, J. M. Chow, A. D. Corcoles, J. A. Smolin, S. T. Merkel, J. R. Rozen, G. A. Keefe, M. B. Rothwell, M. B. Ketchen, and M. Steffen, Phys. Rev. B **86**, 100506(R) (2012). (Cited on pages 4.)

[26] A. A. Houck, J. A. Schreier, B. R. Johnson, J. M. Chow, J. Koch, J. M. Gambetta, D. I. Schuster, L. Frunzio, M. H. Devoret, S. M. Girvin, and R. J. Schoelkopf, Phys. Rev. Lett. **101**, 080502 (2008). (Cited on pages 4.)

[27] V. E. Manucharyan, J. Koch, L. Glazman, and M. H. Devoret, Science **326**, 113 (2009). (Cited on pages 4.)

[28] A. Wallraff, D. I. Schuster, A. Blais, L. Frunzio, R. S. Huang, J. Majer, S. Kumar, S. M. Girvin, and R. J. Schoelkopf, Nature **431**, 162 (2004). (Cited on pages 4.)

[29] D. Vion, A. Aassime, A. Cottet, P. Joyez, H. Pothier, C. Urbina, D. Esteve, and M. H. Devoret, Science **296**, 886 (2002). (Cited on pages 4 and 66.)

[30] A. G. Fowler, M. Mariantoni, J. M. Martinis, and A. N. Cleland, Phys. Rev. A **86**, 032324 (2012). (Cited on pages 4.)

[31] P. Bushev, A. K. Feofanov, H. Rotzinger, I. Protopopov, J. H. Cole, C. M. Wilson, G. Fischer, A. Lukashenko, and A. V. Ustinov, Phys. Rev. B **84**, 060501 (2011). (Cited on pages 4.)

[32] M. U. Staudt, I. C. Hoi, P. Krantz, M. Sandberg, M. Simoen, P. Bushev, N. Sangouard, M. Afzelius, V. S. Shumeiko, G. Johansson, P. Delsing, and C. M. Wilson, J Phys B-at Mol Opt **45**, 124019 (2012). (Cited on pages 4.)

[33] S. Probst, H. Rotzinger, S. Wunsch, P. Jung, M. Jerger, M. Siegel, A. V. Ustinov, and P. A. Bushev, Phys. Rev. Lett. **110**, 157001 (2013). (Cited on pages 4.)

[34] D. Marcos, M. Wubs, J. M. Taylor, R. Aguado, M. D. Lukin, and A. S. Sorensen, Phys. Rev. Lett. **105**, 210501 (2010). (Cited on pages 4.)

[35] I. Diniz, S. Portolan, R. Ferreira, J. M. Gerard, P. Bertet, and A. Auffeves, Phys. Rev. A **84**, 063810 (2011). (Cited on pages 4.)

[36] Y. Kubo, F. R. Ong, P. Bertet, D. Vion, V. Jacques, D. Zheng, A. Dreau, J. F. Roch, A. Auffeves, F. Jelezko, J. Wrachtrup, M. F. Barthe, P. Bergonzo, and D. Esteve, Phys. Rev. Lett. **105**, 140502 (2010). (Cited on pages 4.)

[37] X. B. Zhu, S. Saito, A. Kemp, K. Kakuyanagi, S. Karimoto, H. Nakano, W. J. Munro, Y. Tokura, M. S. Everitt, K. Nemoto, M. Kasu, N. Mizuochi, and K. Semba, Nature **478** (2011). (Cited on pages 4, 46, and 59.)

[38] J. J. L. Morton, A. M. Tyryshkin, R. M. Brown, S. Shankar, B. W. Lovett, A. Ardavan, T. Schenkel, E. E. Haller, J. W. Ager, and S. A. Lyon, Nature **455** (2008). (Cited on pages 4.)

[39] A. Morello, J. J. Pla, F. A. Zwanenburg, K. W. Chan, K. Y. Tan, H. Huebl, M. Mottonen, C. D. Nugroho, C. Yang, J. A. van Donkelaar, A. D. C. Alves, D. N. Jamieson, C. C. Escott, L. C. L. Hollenberg, R. G. Clark, and A. S. Dzurak, Nature **467**, 687 (2012). (Cited on pages 4.)

[40] K. Saeedi, S. Simmons, J. Z. Salvail, P. Dluhy, H. Riemann, N. V. Abrosimov, P. Becker, H. J. Pohl, J. J. L. Morton, and M. L. W. Thewalt, Science **342**, 830 (2013). (Cited on pages 4, 5, and 7.)

[41] K. Tordrup, A. Negretti, and K. Molmer, Phys. Rev. Lett. **101**, 040501 (2008). (Cited on pages 4.)

[42] H. Wu, R. E. George, J. H. Wesenberg, K. Molmer, D. I. Schuster, R. J. Schoelkopf, K. M. Itoh, A. Ardavan, J. J. L. Morton, and G. A. D. Briggs, Phys. Rev. Lett. **105**, 140503 (2010). (Cited on pages 4.)

[43] A. M. Tyryshkin, S. Tojo, J. J. L. Morton, H. Riemann, N. V. Abrosimov, P. Becker, H. J. Pohl, T. Schenkel, M. L. W. Thewalt, K. M. Itoh, and S. A. Lyon, Nat. Mater. **11**, 143 (2012). (Cited on pages 5 and 66.)

[44] A. M. Tyryshkin, J. J. L. Morton, S. C. Benjamin, A. Ardavan, G. A. D. Briggs, J. W. Ager, and S. A. Lyon, J. Phys.: Condens. Matter **18**, S783 (2006). (Cited on pages 5.)

[45] E. Abe, A. M. Tyryshkin, S. Tojo, J. J. L. Morton, W. M. Witzel, A. Fujimoto, J. W. Ager, E. E. Haller, J. Isoya, S. A. Lyon, M. L. W. Thewalt, and K. M. Itoh, Phys. Rev. B **82**, 121201 (2010). (Cited on pages 5 and 66.)

[46] W. M. Witzel, M. S. Carroll, A. Morello, L. Cywinski, and S. Das Sarma, Phys. Rev. Lett. **105**, 187602 (2010). (Cited on pages 5 and 66.)

[47] J. F. Cochran and D. E. Mapother, Phys. Rev. **111**, 133 (1958). (Cited on pages 7, 46, and 65.)

[48] C. Reale, Acta Physica Academiae Scientiarum Hungaricae **37**, 53 (1974). (Cited on pages 7, 46, and 65.)

[49] G. W. Morley, M. Warner, A. M. Stoneham, P. T. Greenland, J. van Tol, C. W. M. Kay, and G. Aeppli, Nat. Mater. **9**, 725 (2010). (Cited on pages 7, 31, 46, 50, 65, 68, and 69.)

[50] R. E. George, W. Witzel, H. Riemann, N. V. Abrosimov, N. Noetzel, M. L. W. Thewalt, and J. J. L. Morton, Phys. Rev. Lett. **105**, 067601 (2010). (Cited on pages 7, 46, 50, 65, and 69.)

[51] G. Wolfowicz, A. M. Tyryshkin, R. E. George, H. Riemann, N. V. Abrosimov, P. Becker, H. J. Pohl, M. L. W. Thewalt, S. A. Lyon, and J. J. L. Morton, Nat. Nanotechnol. **8**, 561 (2013). (Cited on pages 8, 32, 65, 66, 68, 69, and 75.)

[52] M. Hatridge, S. Shankar, M. Mirrahimi, F. Schackert, K. Geerlings, T. Brecht, K. M. Sliwa, B. Abdo, L. Frunzio, S. M. Girvin, R. J. Schoelkopf, and M. H. Devoret, Science **339**, 178 (2013). (Cited on pages 8.)

[53] A. Fang, Y. C. Chang, and J. R. Tucker, Phys. Rev. B **66**, 155331 (2002). (Cited on pages 8.)

[54] C. J. Wellard, L. C. L. Hollenberg, F. Parisoli, L. M. Kettle, H. S. Goan, J. A. L. McIntosh, and D. N. Jamieson, Phys. Rev. B **68**, 195209 (2003). (Cited on pages 8.)

[55] M. Song, S. Lee, and D. J. Lockwood, Phys. Rev. A **82**, 012311 (2010). (Cited on pages 8.)

[56] Y. Yan, J. A. Mol, J. Verduijn, S. Rogge, J. Levine, and F. Remacle, J. Phys. Chem. C **114**, 20380 (2010). (Cited on pages 8.)

[57] R. Rahman, G. P. Lansbergen, S. H. Park, J. Verduijn, G. Klimeck, S. Rogge, and L. C. L. Hollenberg, Phys. Rev. B **80**, 165314 (2009). (Cited on pages 8.)

[58] R. Rahman, S. H. Park, G. Klimeck, and L. C. L. Hollenberg, Nanotechnology **22**, 225202 (2011). (Cited on pages 8.)

[59] H. T. Hui and H. Mirzaei, Ieee Transactions on Electron Devices **58**, 512 (2011). (Cited on pages 8.)

[60] L. Dreher, T. A. Hilker, A. Brandlmaier, S. T. B. Goennenwein, H. Huebl, M. Stutzmann, and M. S. Brandt, Phys. Rev. Lett. **106**, 037601 (2011). (Cited on pages 8 and 72.)

Chapter 2

Magnetic resonance of shallow donors in silicon

This chapter provides the necessary background for understanding of the energy levels of shallow donors in silicon. The theoretical content of section 2.1 will be utilized for modeling the bismuth-readout center molecular orbital in Chapter 5. Section 2.2 presents the spin properties of shallow donors in silicon.

2.1 Energy levels of shallow donors in silicon

Silicon band structure Silicon (Si) is the most widely used semiconductor in the industry. It is also the platform for several proposal of quantum information processing devices [1, 2, 3, 4]. The crystal structure is the diamond structure, that is to say each Si atom is surrounded by four others (four-fold coordinated) forming a tetrahedron. From a quantum mechanical point of view, the energy of a perfect Si crystal can be described with the following Hamiltonian [5, 6]:

$$\begin{aligned}\mathcal{H} = &\sum_i \frac{P_i^2}{2\,M_i} + \sum_j \frac{p_j^2}{2\,m_j} \\ &+ \frac{1}{2}\sum_{i\neq i'} \frac{Z_i\,Z_{i'}\,e^2}{4\pi\epsilon_0\left|\vec{R_i} - \vec{R_{i'}}\right|} + \frac{1}{2}\sum_{j\neq j'} \frac{e^2}{4\pi\epsilon_0\left|\vec{r_j} - \vec{r_{j'}}\right|} - \sum_{i,j} \frac{Z_i\,e^2}{4\pi\epsilon_0\left|\vec{r_j} - \vec{R_i}\right|},\end{aligned} \tag{2.1}$$

where $\vec{R_i}$ is the position of the i^{th} Si nucleus with the electric charge Z_i, $\vec{r_j}$ is the position of the j^{th} electron, and P_i and p_j are the momentum operators of the nuclei and electrons respectively. The mass of the nuclei and of the electrons are denoted by M_i and m_j, respectively. Solving this Hamiltonian for a crystal containing nearly 10^{23} atoms/cm^{-3} is impossible. Thus, it is necessary to make simplifying assumptions in order to solve Eq. (2.1). The first one consists of differentiating the valence electrons and the core electrons of the silicon atoms. The valence electrons are so strongly bound to the nucleus that they can be assumed to have the same motion. So, together with the nucleus, they form the ion core. This simplification results in a drastic reduction of the number of particles that need to be taken into account. The second approximation is the so called Born-Oppenheimer approximation in which it is assumed that the ion cores are much heavier than the electrons. It results from this approximation that the ionic motion is assumed to be much slower than the electronic

motion and electrons "follow" instantaneously the ion cores. As a consequence, the total wave function of the system {nuclei + electrons} can be separated into: $\phi_{\text{tot}} = \phi_{i.c.} \times \phi_e$. The Hamiltonian of Eq. (2.1) is written as $\mathcal{H} = \mathcal{H}_{i.c.} + \mathcal{H}_e + \mathcal{H}_{e-i.c.}$, where $\mathcal{H}_{i.c.}$ is the ionic motion Hamiltonian, $\mathcal{H}_e$ is the electronic Hamiltonian and $\mathcal{H}_{e-i.c.}$ is known as the electron-phonon interaction. The electronic Hamiltonian is then written as

$$\mathcal{H}_e = \sum_j \frac{p_j^2}{2\,m_j} + \frac{1}{2}\sum_{j\neq j'} \frac{e^2}{4\pi\epsilon_0 \left|\vec{r_j} - \vec{r_{j'}}\right|} - \sum_{i,j} \frac{Z_i\, e^2}{4\pi\epsilon_0 \left|\vec{r_j} - \vec{R_i}\right|}. \tag{2.2}$$

This Hamiltonian is not yet computable for a macroscopic crystal. Due to the periodicity of the crystal lattice, one can assume that all the electrons effectively feel the same periodic potential $V(\vec{r})$. Therefore, the many-particle problem is simplified to the one-electron Schrödinger equation

$$\left(\frac{p^2}{2m} + V(\vec{r})\right)\phi_n(\vec{r}) = E_n\phi_n(\vec{r}), \tag{2.3}$$

where E_n and Φ_n are the energy and a wave function associated with the n eigenstate of the one-electron Hamiltonian $\mathcal{H}_e = \frac{p^2}{2m} + V(\vec{r}) = -\frac{\hbar^2}{2m}\nabla^2 + V(\vec{r})$. The series expansion of the potential $V(\vec{r})$ around $\vec{r}$ is written as the sum of a symmetric and an antisymmetric parts [7, 8]

$$V(\vec{r}) = \sum_{\left|\vec{k}\right|\leq k_0} \left(\mathcal{S}(\vec{k})\, V_k^{\text{s.}} + i\,\mathcal{A}(\vec{k})\, V_k^{\text{a.s.}}\right) \exp\left(-i\,\vec{k}\cdot\vec{r}\right), \tag{2.4}$$

where $\mathcal{S}$ and $\mathcal{A}$ stand for the symmetric and antisymmetric forms of the crystal potential for the wavenumber k. Silicon is a homopolar cubic semiconductor that crystallizes into a diamond lattice with two atoms per unit cell. Therefore, taking the origin of the referential between the two atoms 1 and 2 of a unit cell, their positions

Table 2.1: Pseudopotential form factors of Si in eV [8]. These values were obtained by fitting the band diagram of Si measured by reflectivity and photoemission measurements with the pseudopotential model. The X-ray diffraction measurement of the Si lattice constant a_{Si} was measured by Shah and Straumanis [9].

a_{Si}	V_3^{s}	V_8^{s}	V_{11}^{s}
5.43 Å	-2.87 eV	0.54 eV	1.09 eV

are $r_1 = \frac{a_{\mathrm{Si}}}{8}(1,1,1) = \tau$ and $r_2 = -\tau$, where a_{Si} is the lattice constant of Si (see Table 2.1). The potential $V(\vec{r})$ is then given by

$$V(\vec{r}) = \sum_{\left|\vec{k}\right| \leq k_0} \left(\cos(\vec{k}\cdot\tau)\, V_k^{\mathrm{s}}\right) \exp\left(-i\,\vec{k}\cdot\vec{r}\right). \tag{2.5}$$

The crystal structure of Si has a face centered cubic (fcc) reciprocal lattice. The first five vectors of the reciprocal lattice are: $\vec{k_0} = (0,0,0)$, $\vec{k_3} = (1,1,1)$, $\vec{k_4} = (2,0,0)$, $\vec{k_8} = (2,2,0)$ and $\vec{k_1 1} = (3,1,1)$. As the form factor decreases as k^{-2} for large k, only the first five pseudopotential form factors with $k^2 < 11\,(2\pi/a_{\mathrm{Si}})$ are considered. As a consequence, only the five parameters $V_{0,3,4,8,11}^{\mathrm{s}}$ are sufficient [8] to describe the crystal potential of the Si lattice. V_0^s is a constant value baseline to all energy levels and is set at zero. Also, the symmetric form factor V_4^{s} vanishes. The three remaining form factors are listed in Table 2.1.

Using this pseudo-potential Hamiltonian, it is possible to simulate the Si band structure for any wavevector $\vec{k}$. The simulation of the light hole (light blue), heavy hole (dark blue) of the valence band and the conduction band (dark red) are shown in Fig. 2-1 (a). At the Γ point ($k_\Gamma = 0$), the valence band reaches a maximum in energy. As a convention, this point is taken as the zero of the energy. Silicon is an indirect band gap semiconductor and the minimum of the conduction band is not at

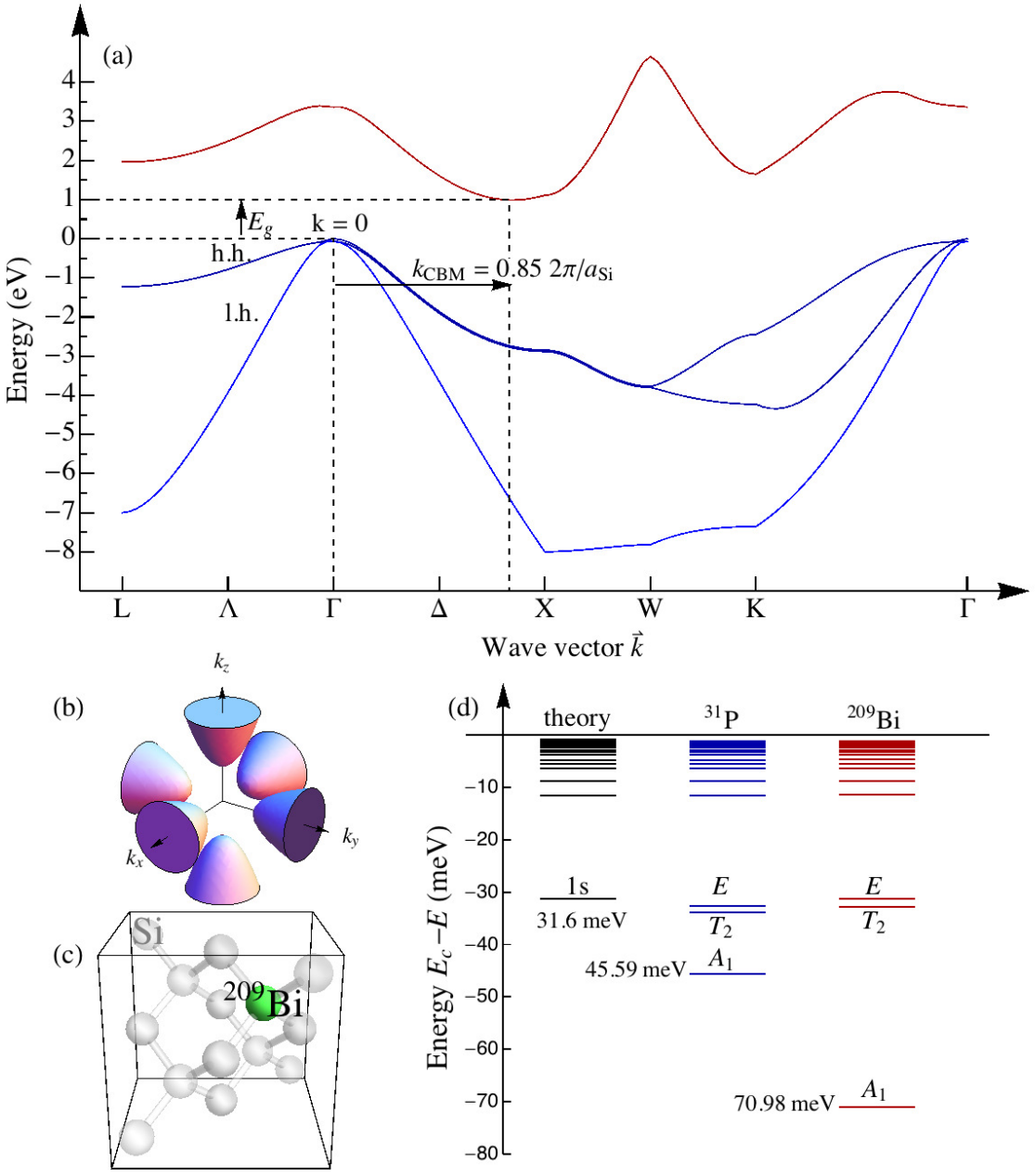

Figure 2-1: (a) Calculated first conduction band (dark red) and last three valence bands of Si. The x-axis is the wavevector $\vec{k}$. Only the main symmetry axis are labeled: $L = \frac{2\pi}{a_{\rm Si}}[1/2, 1/2, 1/2]$, $\Gamma = \frac{2\pi}{a_{\rm Si}}[0, 0, 0]$, $X = \frac{2\pi}{a_{\rm Si}}[1, 0, 0]$, $W = \frac{2\pi}{a_{\rm Si}}[1, 1/2, 0]$ and $K = \frac{2\pi}{a_{\rm Si}}[3/4, 3/4, 0]$. The separation in energy from the top of the heavy hole band (h.h.) at the Γ point to the bottom of the first conduction band defines the band gap energy $E_g = 1.1$ eV. As this minimum corresponds to a wavenumber $k_{\rm CBM} \approx 0.85(2\pi/a_{\rm Si})$, Si is said to be an indirect band gap semiconductor. Due to the cubic symmetry of the system there are six minima, plotted in (b), which are degenerate occurring at $\vec{k_{\rm CBM}} \approx \frac{2\pi}{a_{\rm Si}}[\pm 0.85, \pm 0.85, \pm 0.85]$. (c) Representation of the diamond structure of a Si (gray) crystal with one substitutional Bi donor (green).

the Γ point, but it is at $\vec{k_0} = (0.85, 0, 0)$, near the X point $\vec{k_X} = (1, 0, 0)$. Actually, the conduction band of Si has six minima at $\vec{k_{\rm CBM}} = (\pm 0.85, 0, 0), (0, \pm 0.85, 0)$ and $(0, 0, \pm 0.85)$. We have plotted in Fig. 2-1(b) the six conduction band minima assuming that the lowest conduction band is isotropic, non degenerate, and parabolic. The band gap energy is $E_g = 1.1$ eV at room temperature ($k_B T = k_B 300\,\mathrm{K} \approx 25$ meV).

Shallow donors in silicon The four (plus one) group V shallow donors in silicon are ^{31}P, ^{75}As, ^{121,123}Sb and ^{209}Bi. At a substitutional site (see Fig. 2-1(c)), they form four bonds with the nearest Si atoms and the remaining unpaired (paramagnetic) electron is bond to its nucleus by the Coulomb potential. To calculate the wave function and the energy of the $1s$ ground state of such shallow donors, the Coulomb potential of the substitutional donor ion core has to be added to the Hamiltonian of Eq. 2.3,

$$\left(\frac{p^2}{2m} + V(\vec{r}) + U(\vec{r}) \right) \phi(\vec{r}) = E_n \phi(\vec{r}), \tag{2.6}$$

where $U(\vec{r}) = -\frac{e^2}{4\pi\epsilon\epsilon_0 r}$, $\epsilon = 11.7$ being the relative dielectric constant of Si measured by Salzberg and Villa using refractive index measurements [10]. Due to this large reduction of the Coulomb field at the donor nucleus, the bound states of donor electron are expected to have a large spatial expansion compared to the lattice spacing. In this limit, the solutions of the Schrödingier equation (Eq. 2.6) can be written as the product

$$\phi^{(\vec{k_{\rm CBM}})}(\vec{r}) = \chi^{(\vec{k_{\rm CBM}})}(\vec{r})\ u(\vec{k_{\rm CBM}}, \vec{r}), \tag{2.7}$$

Table 2.2: Linear coefficients of the Bloch wave functions $\phi_{\vec{k_j}}$ for the three irreducible representations of the T_d group. The completely symmetric A_1 singlet is the only state having a finite electron density at the impurity site. Therefore, it is the most sensitive state to the attractive central cell perturbations. This is an intuitive explanation to the fact that it is usually the lowest energy state.

$\vec{k_j}$	$k_{\mathrm{CBM}}\,\vec{x}$	$-k_0\,\vec{x}$	$k_{\mathrm{CBM}}\,\vec{y}$	$-k_0\,\vec{y}$	$k_{\mathrm{CBM}}\,\vec{z}$	$-k_0\,\vec{z}$
A_1:	$1/\sqrt{6}$	$1/\sqrt{6}$	$1/\sqrt{6}$	$1/\sqrt{6}$	$1/\sqrt{6}$	$1/\sqrt{6}$
E:	$1/2$	$1/2$	$-1/2$	$-1/2$	0	0
	$-1/\sqrt{12}$	$-1/\sqrt{12}$	$-1/\sqrt{12}$	$-1/\sqrt{12}$	$2/\sqrt{12}$	$2/\sqrt{12}$
T_2:	$1/\sqrt{2}$	$-1/\sqrt{2}$	0	0	0	0
	0	0	$1/\sqrt{2}$	$-1/\sqrt{2}$	0	0
	0	0	0	0	$1/\sqrt{2}$	$-1/\sqrt{2}$

where $\Phi(\vec{k_{\mathrm{CBM}}}, \vec{r})$ is the free electron at the conduction band minimum k_{CBM} (solution of Eq. 2.3), and $F^{(k_{\mathrm{CBM}})}(\vec{r})$ satisfies the effective mass equation

$$\left(\frac{p_l^2}{2m_l} + \frac{p_{t_1,t_2}^2}{2m_t} - U(\vec{r})\right)\chi^{(k_{\mathrm{CBM}})}(\vec{r}) = E\,\chi^{(k_{\mathrm{CBM}})}(\vec{r}). \tag{2.8}$$

In this equation, p_l and p_t are the electron momentum operators associated with the longitudinal and transversal directions (relative to $\vec{k_{\mathrm{CBM}}}$), and $m_l = 0.98\,m_e$ and $m_t = 0.19\,m_e$ are the effective electron mass in these directions. In the hydrogenic limit, $m_l = m_t$ and the envelop function is

$$\chi^{(k_{\mathrm{CBM}})}(\vec{r}) = \frac{1}{\sqrt{\pi}a_0^{3/2}}\,\exp\left(-r/a_0\right) \tag{2.9}$$

where a_0 is the Bohr radius of the donor electron wave function. It is defined as $a_0 = \frac{4\pi\epsilon_0\hbar^2}{Z\,m_e\,e^2}$ for an hydrogenous atom with a charge Z in vacuum.

Table 2.3: Principal parameters for the description of the group V donors in silicon [11]: ionization energy (E_I) and Bohr radius (a_0).

	^{31}P	^{75}As	^{121}Sb	^{123}Sb	^{209}Bi
E_I (meV)	45.59	53.76	42.74	42.74	70.98
a_0 (Å)	16.8	15.5	17.3	17.3	11.5

The donor electron wave function in the ground state can be written

$$\Phi_i(\vec{r}) = \sum_{j=1}^{6} c_{i,j}\phi^{\vec{k_j}}(\vec{r}), \tag{2.10}$$

where the coefficients $c_{i,j}$ are listed in Table 2.2. Only the wave function corresponding to the A_1 symmetry has a non vanishing density probability at the nucleus site ($\vec{r} = \vec{0}$). The energy associated with the symmetry states A_1, E and T_2 are shown in Fig. 2-1(d) for the effective mass approximation. The experimental values of the energy for the shallow donor states are sensibly different from the results of the effective mass approximation [12, 13] [see Fig. 2-1(d)]. This is mainly due to central cell corrections that have to be taken into account for "small" electron orbits (e.g., $1s$ orbital). This energy discrepancy is larger for more confined donor electrons such as the Bi donor electron.

2.2 Magnetic resonance

2.2.1 Spin Hamiltonians

Electron Zeeman interaction An electron is an elementary particle with a spin $S = 1/2$ and can be associated with three different magnetic moments: the spin angular momentum $\boldsymbol{\mu_S}$, the orbital momentum $\boldsymbol{\mu_L}$ and the total angular momentum $\boldsymbol{\mu_J}$. The spin angular momentum is defined as

$$\boldsymbol{\mu_S} = g_e \frac{-e}{2m_e} \hbar \boldsymbol{S} = g_e \mu_B \boldsymbol{S}, \tag{2.11}$$

where e is the electron charge, m_e is the electron mass, $\hbar = h/2\pi$ is the reduced Planck constant, and $\mu_B = \frac{-e}{2m_e}\hbar = 9.274 \times 10^{-24}$ J/T is the Bohr magneton. The dimensionless factor $g_e = 2.0023193043622(15)$ is the electron spin g factor. It differs from 2 due to the anomalous magnetic dipole moment that can be calculated using quantum electrodynamics theory [14]. One can also define the orbital momentum as $\boldsymbol{\mu_L} = -\frac{g_L \mu_B}{\hbar}\boldsymbol{L}$, where $g_L = 1$ is the electron orbital g factor and $\boldsymbol{L}$ is the electron orbital angular momentum, and the total angular momentum as $\boldsymbol{\mu} = -\frac{g_J \mu_B}{\hbar}\boldsymbol{J}$, where $\boldsymbol{J} = \boldsymbol{S} + \boldsymbol{L}$ is the total angular momentum. Using the last definition, the energy of the magnetic moment $\boldsymbol{\mu}$ in a magnetic field $\boldsymbol{B}$ is

$$E_Z = -\boldsymbol{\mu} \cdot \boldsymbol{B}. \tag{2.12}$$

Actually, under a strong enough magnetic field (> 1 T) [15, 16], this expression becomes quadratic in magnetic field. This quadratic term appears in the expansion of $(\boldsymbol{p} + e/c\boldsymbol{A})^2$. In electron paramagnetic resonance (EPR), the spins of interest are the unpaired (paramagnetic) electron spins. Therefore, the spin quantum number

is aligned with the homogeneous magnetic field B_Z. From this point, we assume that the for a single spin, the operators $\boldsymbol{S}$ and S_Z form a complete set of commuting observables. Therefore, the spin quantum numbers S and m_S are sufficient to describe the complete state of an electron. Especially, it means that the electron spin state $|S, m_S\rangle$ is decoupled from its orbital. This assumption will be justified in the next paragraph. As a consequence, we can restrict ourselves to the spin angular momentum $\boldsymbol{\mu_S}$ to describe the electron Zeeman energy,

$$\mathcal{H}_Z = g\,\mu_B\,B_Z\,S_Z, \tag{2.13}$$

where the spin Hamiltonian is denoted by $\mathcal{H}$. The two trivial eigenstates are:

$$E_{1/2} = \frac{1}{2} g\,\mu_B\,B_Z \tag{2.14a}$$

$$E_{-1/2} = -\frac{1}{2} g\,\mu_B\,B_Z. \tag{2.14b}$$

These energies are plotted in Fig. 2-2(a) as a function of the magnetic field. The electron spin transition, defined as $|m_S = -1/2\rangle \leftrightarrow |m_S = 1/2\rangle$ [(red arrow in Fig. 2-2(a)], occurs for a microwave photon of energy $\hbar\omega = E_{1/2} - E_{-1/2} = g\mu_B B_Z$. Due to the finite coherence time of each state, the magnetic field sweep (resp. frequency) spectrum recorded at constant frequency (magnetic field), shown in Fig. 2-2(b), does not follow the Dirac distribution, but rather the Lorentzian distribution with a finite linewidth. The conventional magnetic dipole transition operator[1] is S_X and the transition probability between the $|-1/2\rangle$ and $|1/2\rangle$ states is $\langle 1/2|S_X|-1/2\rangle$.

In a solid-state system, the spin description of the paramagnetic species differs

[1] In conventional EPR spectrometers, the magnetic field B_1 generated by the microwave is perpendicular to the static magnetic field $B_0 = B_Z$. Thus, any linear combination of S_X and S_Y can describe the magnetic dipole transition used in such spectrometers.

in several ways from the free electron spin description. This is due to interactions, not taken into account until now, of the central spin with its environment. The first correction to consider is the spin orbit coupling of the electron. Then, the electron Zeeman Hamiltonian of Eq. (2.13) becomes

$$\mathcal{H}^{(1)} = -g_e\,\mu_B\,\boldsymbol{S}\cdot\boldsymbol{B} + \lambda\,\boldsymbol{L}\cdot\boldsymbol{S} - \mu_B\,\boldsymbol{L}\cdot\boldsymbol{B}, \tag{2.15}$$

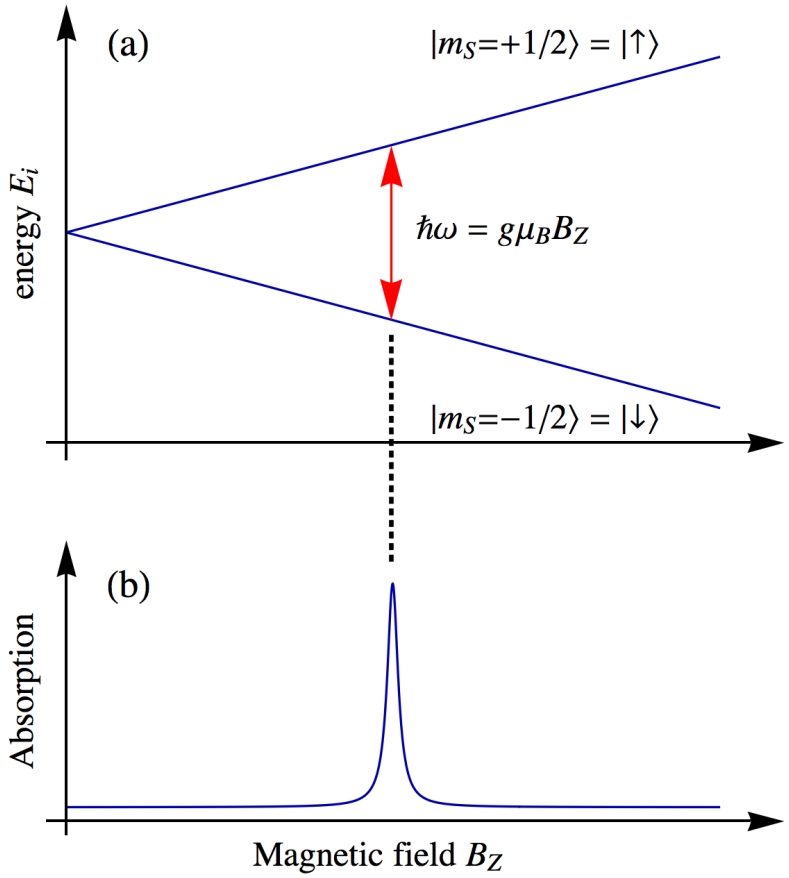

Figure 2-2: (a) Representation of the energy level of the electron spin up and down states as a function of magnetic field. The resonance condition is fulfilled when the microwave photon has a frequency corresponding to $g\mu_B B_Z$. (b) Typical magnetic field sweep spectrum of a two-level system, assuming a finite coherence time of each state.

Table 2.4: Values of the spin-orbit interaction for selected group IV and III-V semiconductors [18]. One can notice the strong dependence of the parameter λ on the atomic mass.

Group IV	C	Si	Ge	SiC
λ (meV)	9	29	197	9
Group III-V	GaN	GaP	GaAs	GaSb
λ (meV)	11	53	227	500

where λ is the spin-orbit interaction of the central electron in a given host material. We will restrict our discussion to the case of donors in silicon. To include this correction into an "effective" electron g factor $g_{i,j} = g_e\delta_{i,j} + \delta g_{i,j}$, we are only interested in the terms of $\mathcal{H}^{(1)}$ that are bilinear in spin operator and magnetic field so that:

$$\delta g_{i,j} = 2\lambda \sum_n \frac{\langle\psi_0|L_i|\psi_n\rangle\langle\psi_m|L_j|\psi_0\rangle}{E_0 - E_n}. \tag{2.16}$$

One can notice that the correction $\delta g_{i,j}$ may be anisotropic. However, for a donor electron in unstrained silicon [17], it appears not to be the case and $\delta g_{i,j} = \delta_g$. The effective g factor for the group V donors in silicon are listed in Table 2.5.

Nuclear Zeeman interaction All the group V donors in silicon have a half integer nuclear spin (see Table 2.5). Associated g factors, denoted g_n, are also listed in Table 2.5. As a nucleus is the "extreme" case of wave function localization, its spin g factor is independent of the host material and spin-orbit corrections.

Spin-spin couplings There are two kinds of spin-spin couplings: the direct and indirect couplings. The direct couplings are the interactions between the electric or magnetic moments of the two spins, e.g., the magnetic dipole-dipole interaction $\overleftrightarrow{D}$ and it is a special case of the Fermi contact interaction $\overleftrightarrow{A}$. The indirect coupling

includes the spin exchange coupling $\overleftrightarrow{J}$.

Hyperfine interaction We start the spin-spin coupling section from the hyperfine interaction as it the usually the strongest spin-spin interaction for group V donors in silicon. The hyperfine interaction Hamiltonian is given by

$$\mathcal{H}_{\mathrm{HF}} = \boldsymbol{S}^{\mathrm{T}} \overleftrightarrow{A} \boldsymbol{I}, \tag{2.17}$$

where $\overleftrightarrow{A}$ is the hyperfine interaction tensor. It can be written as the sum of an isotropic component and a traceless tensor,

$$\overleftrightarrow{A} = h\, A_{\mathrm{DD}} + h\, A_{\mathrm{iso}} \mathbb{1}. \tag{2.18}$$

In this equation, $h\, A_{\mathrm{DD}}$ is the interaction assuming that one of the spins is a point magnetic dipole and has no spatial expansion. To take into account the finite extent of the nucleus, one has to consider the interaction corresponding to the overlap of the wave function A_{iso}. It is called the Fermi contact hyperfine interaction.

$$A_{\mathrm{iso}} = \frac{\mu_0}{4\pi} \int \mathrm{d}v \left| \langle \psi_S | \psi_I \rangle \right|^2 \tag{2.19}$$

$$= \frac{\mu_0}{4\pi}\, g_e\, \mu_e\ g_n\, \mu_n\ \left| \psi_S(\vec{r}_I) \right|^2 \tag{2.20}$$

In Eq. (2.18), A_{DD} is the magnetic dipole-dipole interaction of the donor electron spin and nuclear spin, assuming the nuclear spin as a point magnetic dipole. Therefore, this interaction vanishes in the case of a donor in silicon with a T_d symmetry. Thus,

the hyperfine spin Hamiltonian is simply

$$\mathcal{H}_{\mathrm{HF}} = h\,A\,\boldsymbol{S}\,\cdot\,\boldsymbol{I}. \tag{2.21}$$

The numerical values of the hyperfine interaction for group V donor in silicon are listed in Table 2.5.

Dipole-dipole interaction The magnetic dipole-dipole interaction of the donor electron spin and nuclear spin vanishes due to the electron wave function symmetry. On the other hand, "distant" paramagnetic species or nuclear spin may have a finite magnetic dipole-dipole interaction with the donor electron spin,

$$\mathcal{H}_{\mathrm{DD}} = \boldsymbol{S}^{\mathrm{T}}\ \overleftrightarrow{D}\ \boldsymbol{S_2}, \tag{2.22}$$

with $\overleftrightarrow{D}$ the dipole-dipole interaction tensor

$$\overleftrightarrow{D} = \frac{\mu_0}{4\pi}\,g_e\,\mu_e\ g_2\,\mu_n\left(\frac{3\ (\boldsymbol{S}\vec{r})\ (\vec{r}\boldsymbol{S_2})}{r^5} - \frac{\boldsymbol{S}\,\cdot\,\boldsymbol{S_2}}{r^3}\right), \tag{2.23}$$

where $\vec{r} = \vec{r_1} - \vec{r_2}$ is the relative position vector of the two spins.

Two electron spins exchange interaction

$$J_{i,j} = \int_{\mathbb{R}^3} \mathrm{d}v\ \ \Phi^*_{b,j}\,\frac{e^2}{4\pi\epsilon\epsilon_0 r_{a,b}}\,\Phi_{a,i}, \tag{2.24}$$

where $\Phi_{a,i}$ ($\Phi_{b,j}$, resp.) is the one electron spin-orbital wave function of the electron a (b) in the spin state i (j).

$$\mathcal{H}_{\mathrm{Exch}} = \boldsymbol{S}^{\mathrm{T}}\ \overleftrightarrow{J}\ \boldsymbol{S}. \tag{2.25}$$

Table 2.5: Principal spin properties of the group V donors in silicon [25]: electron g factor (g_e), nuclear spin (I), nuclear g factor (g_n) and hyperfine interaction (A).

	^{31}P	^{75}As	^{121}Sb	^{123}Sb	^{209}Bi
g_e	1.9985(1)	1.9984(1)	1.9986(1)	1.9986(1)	2.0032(1)
I	1/2	3/2	5/2	7/2	9/2
g_n	2.26320	0.95965(5)	1.3454(2)	0.7285(1)	0.91347(4)
A (MHz)	117.53(2)	198.35(2)	186.802(5)	101.516(4)	1475.4(1)

This interaction is particularly large for two strongly overlapping electrons, such as two nearby shallow donor electrons. Interaction strength as large as 38 meV for a donor separation $d = a_0$ and 1 meV for a separation of $d = 4\,a_0$ have been estimated by Wu and Fischer [19, 20]. This coupling strongly depends on the relative position of the donors in a silicon crystal [21]. On the other hand, for weakly overlapping electrons, this coupling rapidly vanishes and can be neglected in the case of a shallow donor interacting with a point defect (^{31}P$-$P$_{b0}$) [22].

2.2.2 Special case of bismuth donors in silicon

Bismuth is the deepest group V donor in silicon. It has a remarkably strong electron nuclear hyperfine coupling when compared to other group V donors and, together with its large nuclear spin, these properties make it suitable for quantum information application, as explained in section 1.1. The spin system of an isolated Bi donor in a static magnetic field B_0 (electron spin $S = 1/2$ and ^{209}Bi nuclear spin $I = 9/2$) can be represented by the spin Hamiltonian:

$$\mathcal{H} = g\mu_B B_0 S_z - g_n \mu_n B_0 I_z + hA\boldsymbol{S}\cdot\boldsymbol{I}, \tag{2.26}$$

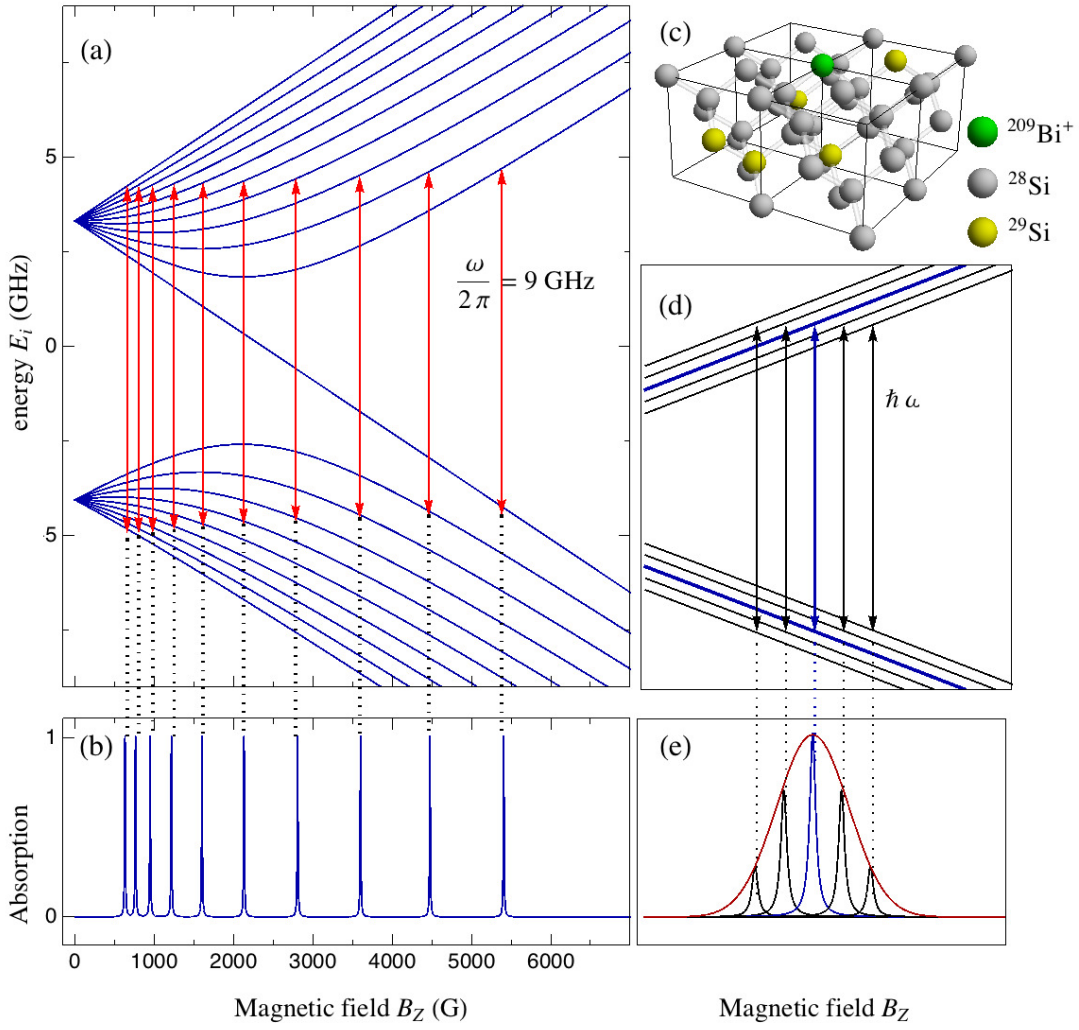

Figure 2-3: (a) Bi donor eigenvalues as a function of the magnetic field. The red arrows indicates the electron spin resonance transitions at X-band (9 GHz). (b) The resulting field sweep EPR absorption spectrum of Bi donor. (c) Schematic representation of four unit cell of a silicon crystal. The central Bi donor is shown in green and 4.7 % of the silicon atoms are ^{29}Si in yellow. The hyperfine interaction of the donor electron spin with close ^{29}Si nuclear spin [23, 24] is the origin of the inhomogeneous broadening of the EPR lines. Different configurations of the nearby ^{29}Si lead to variations of the resonant frequency of an EPR line, shown as black lines in (d). The resulting absorption peak shape takes Gaussian shape as in (e).

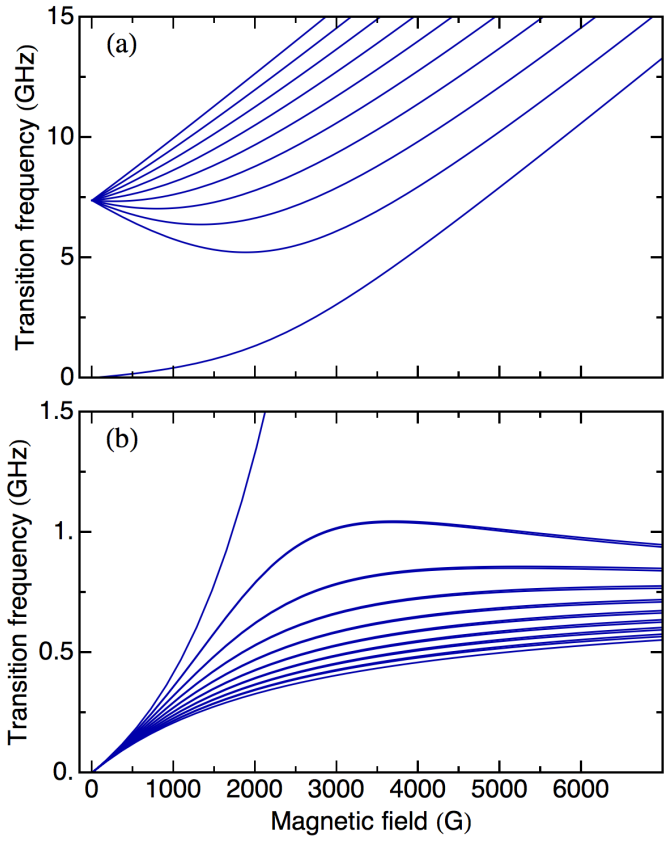

Figure 2-4: Transition frequency of the ten EPR (a) and eighteen NMR (b) allowed transitions of Bi donors in Si. The apparent eight thick lines in (b) correspond to eight groups of two lines, as for a given couple $(m_{_F}, m_{_{F+1}})$, the NMR transition frequency depends only weakly on the quantum number F. The two remaining single lines are the transition involving the pure spin states $|F = 5, m_{_F} = 5\rangle = |m_{_S} = 1/2, m_{_I} = 9/2\rangle$ and $|F = 5, m_{_F} = -5\rangle = |m_{_S} = -1/2, m_{_I} = -9/2\rangle$. The spin Hamiltonian parameters used for the simulations are listed in Table 2.5.

where μ_B and μ_n are the Bohr and nuclear magnetons, and $g = 2.0003$ (Ref. [25]) and $g_n = 0.914$ (Ref. [26]) are Bi electron and nuclear g-factors, respectively. Under magnetic resonance, the magnetic dipole operator $\cos\omega t\ S_{_X}$ $(\cos\omega t\ I_{_X})$ has to be included in the spin Hamiltonian of Eq. (2.26) in order to compute the frequency of the EPR (NMR) transitions. The EPR and NMR transition frequencies of Bi donors are plotted in Fig. 2-4 as functions of the magnetic field. The large nuclear spin of

Table 2.6: Summary of the clock transition (CT) and hyperfine clock transition (HCT) resonance conditions for Bi donors in silicon [27]. $F = S + I$ denotes the total spin and m_F its projection.

	$\Delta F = +1$, $m_F =$	$-1 \leftrightarrow 0$	$-2 \leftrightarrow -1$	$-3 \leftrightarrow -2$	$-4 \leftrightarrow -3$
CT	Resonant field (G)	266	798	1333	1878
	Resonance frequency (MHz)	7338	7032	6372	5214
	$\Delta m_S = +1$, $m_I =$	-1/2	-3/2	-5/2	-7/2
HCT	Resonant field (G)	26070	8680	5190	3690
	Resonance frequency (MHz)	72640	23180	12570	7305

Bi generates ESR resonance conditions that can be either robust against magnetic field fluctuations at the clock transition (flat points in Fig. 2-4) and against electric field perturbation at the hyperfine clock transition [27]. These resonance conditions are summarized in Table 2.6.

Bibliography

[1] S. Lloyd, Science **261**, 1569 (1993). (Cited on pages 16.)

[2] B. E. Kane, Nature **393**, 133 (1998). (Cited on pages 16.)

[3] D. Loss and D. DiVincenzo, Phys. Rev. A **57**, 120 (1998). (Cited on pages 16.)

[4] T. D. Ladd, D. Maryenko, Y. Yamamoto, E. Abe, and K. M. Itoh, Phys. Rev. B **71**, 014401 (2005). (Cited on pages 16.)

[5] W. Kohn and J. M. Luttinger, Phys. Rev. **98** (1955). (Cited on pages 16.)

[6] R. A. Faulkner, Phys. Rev. **184**, 713 (1969). (Cited on pages 16.)

[7] J. C. Phillips, Phys. Rev. **112**, 685 (1958). (Cited on pages 17.)

[8] M. L. Cohen and T. K. Bergstresser, Phys. Rev. **141**, 789 (1966). (Cited on pages 17 and 18.)

[9] J. S. Shah and M. E. Straumanis, Solid State Commun. **10**, 159 (1972). (Cited on pages 18 and 74.)

[10] C. D. Salzberg and J. J. Villa, Journal of the Optical Society of America **47**, 244 (1957). (Cited on pages 20.)

[11] E. B. Hale and R. L. Mieher, Phys. Rev. **184**, 751 (1969). (Cited on pages 22.)

[12] R. L. Aggarwal and A. K. Ramdas, Phys. Rev. **140**, 1246 (1965). (Cited on pages 22.)

[13] R. A. Faulkner, Bull. Am. Phys. Soc. **14**, 394 (1969). (Cited on pages 22.)

[14] J. Schwinger, Phys. Rev. **73**, 416 (1947). (Cited on pages 23.)

[15] R. H. Garstang, Rep. Prog. Phys. **40**, 105 (1977). (Cited on pages 23.)

[16] A. Thilderkvist, M. Kleverman, G. Grossmann, and H. G. Grimmeiss, Phys. Rev. B **49** (1994). (Cited on pages 23.)

[17] D. K. Wilson and G. Feher, Phys. Rev. **124**, 1068 (1961). (Cited on pages 26 and 72.)

[18] P. Y. Yu and M. Cardona, *Fundamentals of Semiconductors*, Springer (2010). (Cited on pages 26.)

[19] P. R. Cullis and J. R. Marko, Phys. Rev. B **1**, 632 (1970). (Cited on pages 29.)

[20] W. Wu and A. J. Fisher, Phys. Rev. B **77**, 045201 (2008). (Cited on pages 29.)

[21] B. Koiller, R. B. Capaz, X. D. Hu, and S. Das Sarma, Phys. Rev. B **70**, 115207 (2004). (Cited on pages 29.)

[22] J. M. Lu, F. Hoehne, A. R. Stegner, L. Dreher, M. Stutzmann, M. S. Brandt, and H. Huebl, Phys. Rev. B **83**, 235201 (2011). (Cited on pages 29 and 71.)

[23] E. B. Hale and R. L. Mieher, Phys. Rev. **184**, 739 (1969). (Cited on pages 30 and 78.)

[24] J. L. Ivey and R. L. Mieher, Phys. Rev. B **11**, 822 (1975). (Cited on pages 30.)

[25] G. Feher, Phys. Rev. **114**, 1219 (1959). (Cited on pages 29, 31, 46, 65, and 68.)

[26] G. W. Morley, M. Warner, A. M. Stoneham, P. T. Greenland, J. van Tol, C. W. M. Kay, and G. Aeppli, Nat. Mater. **9**, 725 (2010). (Cited on pages 7, 31, 46, 50, 65, 68, and 69.)

[27] G. Wolfowicz, A. M. Tyryshkin, R. E. George, H. Riemann, N. V. Abrosimov, P. Becker, H. J. Pohl, M. L. W. Thewalt, S. A. Lyon, and J. J. L. Morton, Nat. Nanotechnol. **8**, 561 (2013). (Cited on pages 8, 32, 65, 66, 68, 69, and 75.)

Chapter 3

Methodology and experiments

This chapter describes the spin dependent recombination spectroscopy technique and the experimental setup. A description of the sample preparation is also provided.

3.1 Spin dependent recombination technique

The continuous illumination provided by an above band-gap light generats photoexcited electrons in the sample [see Fig. 3-1]. The capture of photocarriers by the ionized donors of the donor-readout center (D-R) pairs takes place on a time scale τ_{ec} of the order of 10 to 100 μs for an illumination of 635 nm of 20 mW/cm^2 at 5 K [1]. For the phosphorus donor coupled to a dangling bond readout center, the expected recombination time for the antiparallel electron spin pair is typically $\tau_{\mathrm{ap}} \approx 10$ μs whereas for the parallel spin pair, the recombination time $\tau_{\mathrm{p}} \approx 1$ ms is much longer [1]. Preliminary time-resolved electrically detected magnetic resonance (EDMR) measurements of Bi-R pairs in $^{\mathrm{nat}}$Si:Bi shows dynamics similar to the donor coupled to a dangling bond defect situating at the Si/SiO_2 interface even though the readout centers R created by the implantation are situated around 90 nm deep. As a consequence, only the parallel spin pairs remain in the steady state under illumination without external induction of the magnetic resonance. Therefore, flipping the donor electron spins by the external magnetic resonance irradiation breaks this steady-state

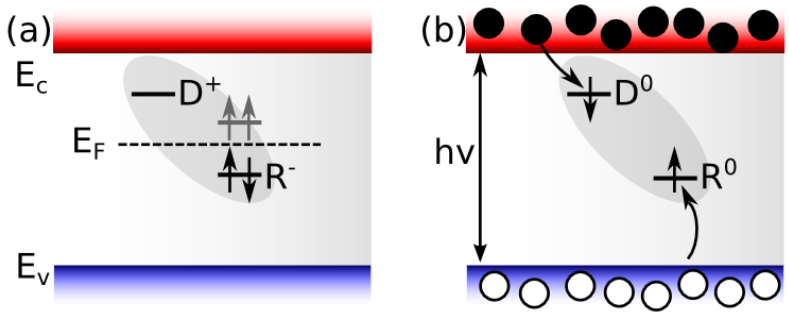

Figure 3-1: Schematic representation of the donor and readout center energy levels within the Si band gap. The valence (conduction) band is represented in blue (red). The energy levels of the ionized donor D^+ and negatively charged readout center (R^-) are represented relatively to the expected Fermi level in (a). The above band gap illumination photo neutralizes the donor and the readout centers (b).

constant current situation and decreases the photocurrent by the enhancement of the spin-dependent recombinations [2]. Such a change of the sample photoconductivity leads to a decrease in the absorption of the microwave electric field by the sample and the photocarriers generated. The decrease in the microwave absorption by the sample then leads to an enhancement in the Q factor of the EPR cavity. The defect utilized as a readout center in this study has a g factor of $g \approx 2.005$ measured by the cross-relaxation R($|1\rangle \leftrightarrow |2\rangle$)-Bi($|8\rangle \leftrightarrow |13\rangle$) (Ref. [3]) but its microstructure is unknown. A small coil placed near the sample within the EPR cavity is used to excite the magnetic resonance. On the other hand, the X-band ($\approx$ 9.08 GHz) irradiation and reflection are used for probing the change in the sample conductivity. Since the additional coil near the sample can apply an arbitrary microwave frequency, it is possible to reduce the frequency along with the static magnetic field [3]. The second derivative of the reflected X-band intensity with respect to the field modulation is recorded as an SDR signal to reduce the broad cyclotron resonance lines and the background change of the sample conductivity during the magnetic field scan. All the SDR measurements are performed at 16 K.

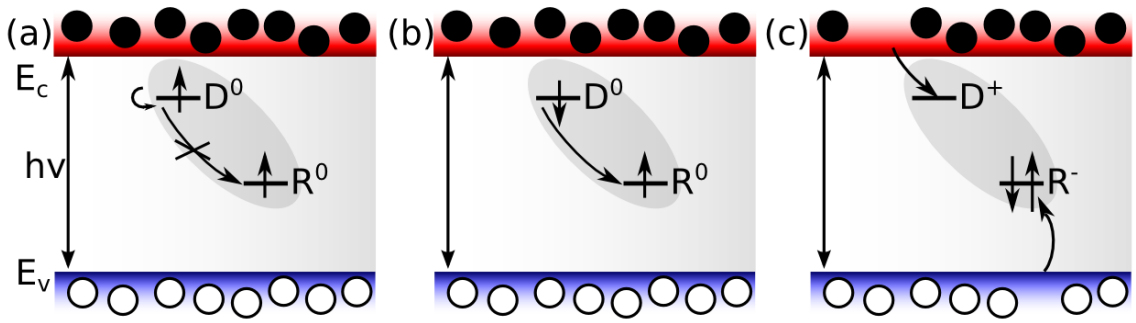

Figure 3-2: Donor-readout center pair recombination process. (a) In the steady state, the spin pair is in the parallel configuration (spin blockade). Under magnetic resonance, the donor electron spin flips and the spin pair becomes in the antiparallel configuration (b). The donor electron can then recombine via the readout center and a free electron can be capture by the ionized donor (c).

3.2 Experimental setup

The SDR-MR spectra are recorded at 16 K with a commercial continuous wave EPR spectrometer (JEOL JES-RE3X) working at X-band (9 GHz microwave) with a home-made coil for radio frequency ($20 - 400$ MHz) and microwave (7.304 and 8.141 GHz) irradiation to induce magnetic resonance at low field ($6 - 110$ mT). Figure 3-3 shows the schematic representation of the experimental setup and Fig. 3-4 shows the pho-

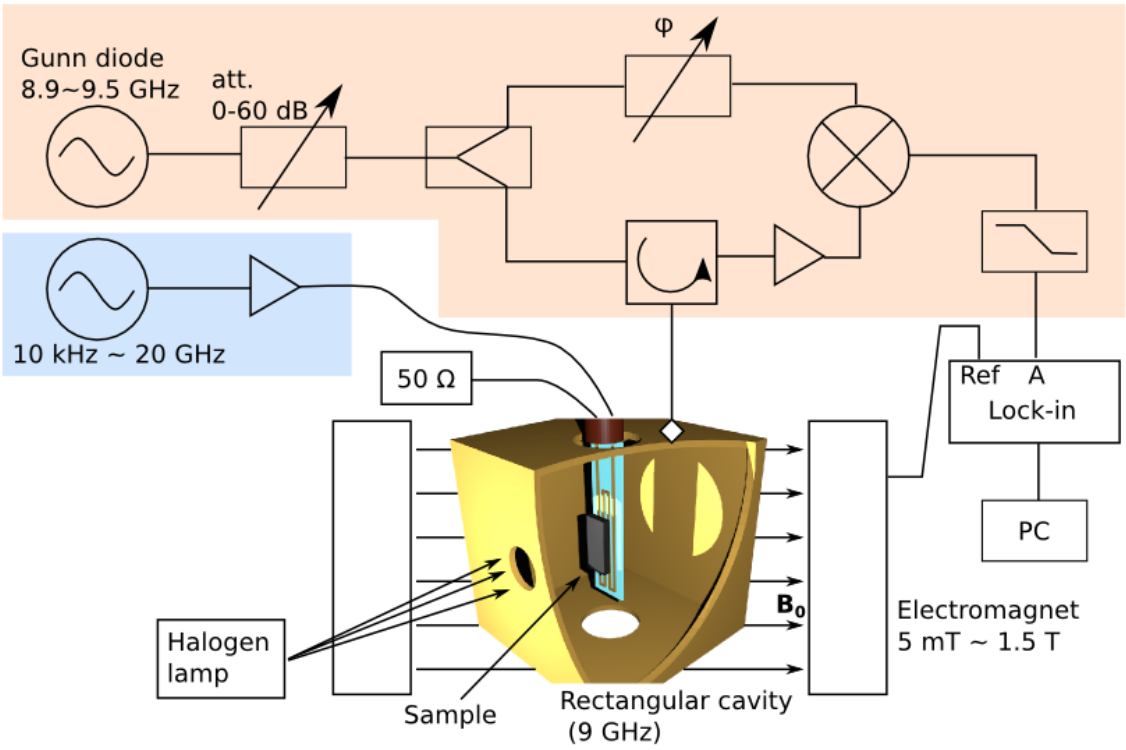

Figure 3-3: Experimental setup for cw SDR or ESR. The sample is attached to a sample holder made in oxygen-free quartz and placed into a microwave cavity, at an antinode of the magnetic field $\boldsymbol{B_1}$. The mw cavity is designed so that the ^{4}He cryostat (not represented on the schematics) can fit inside. This system is situated between the two coils of an electromagnet (Helmholtz configuration). The cw SDR or ESR signal is measured by the bridge as the reflected mw intensity from the cavity. Using the phase shifter, one can adjust the phase of the detected complex susceptibility χ of the sample. The output signal of the mw detection diode is fed into a lock-in amplifier for more sensitivity.

tographs of the spectrometer (a) and the sample and mounted on the sample holder (b).

Continuous above band-gap illumination of 100 mW/cm^{-2} (measured outside the EPR cavity) provided by a 100-W halogen lamp generates photocarriers in the sample. Magnetic resonance can enhance the spin-dependent recombination, which decreases the density of photocarriers. Then, the absorption of the microwave electric field by the photocarriers is decreased, leading to an enhancement in the Q-factor of the cavity. Thus, the effect of magnetic resonance can be detected simply as the change in the X-band microwave reflection from the cavity. The second derivative of the reflected intensity with respect to the field modulation was recorded as an SDR signal to reduce the broad cyclotron resonance lines and the background change of the

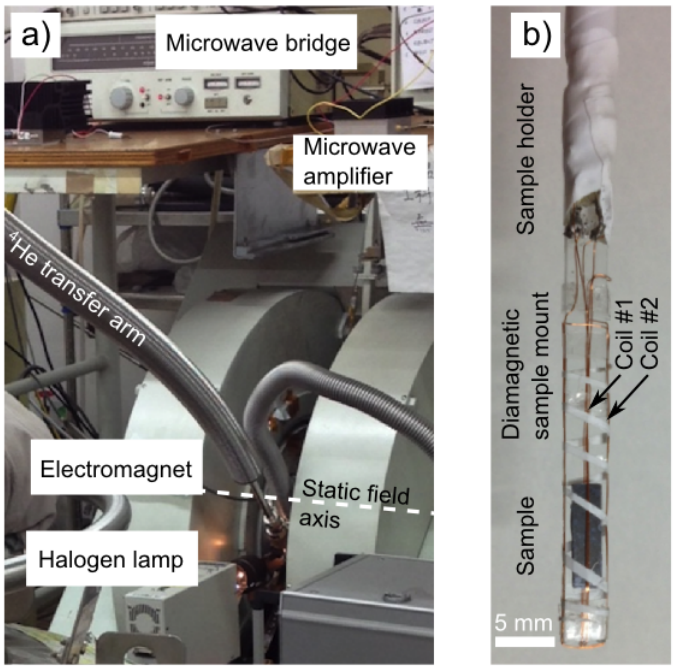

Figure 3-4: (a) Experimental setup used in this work. The Oxford Instrument ^{4}He cryostat is located between the two coils of the electromagnet. (b) Sample and sample holder used for the multifrequency experiment (see Chapters 4 and 4).

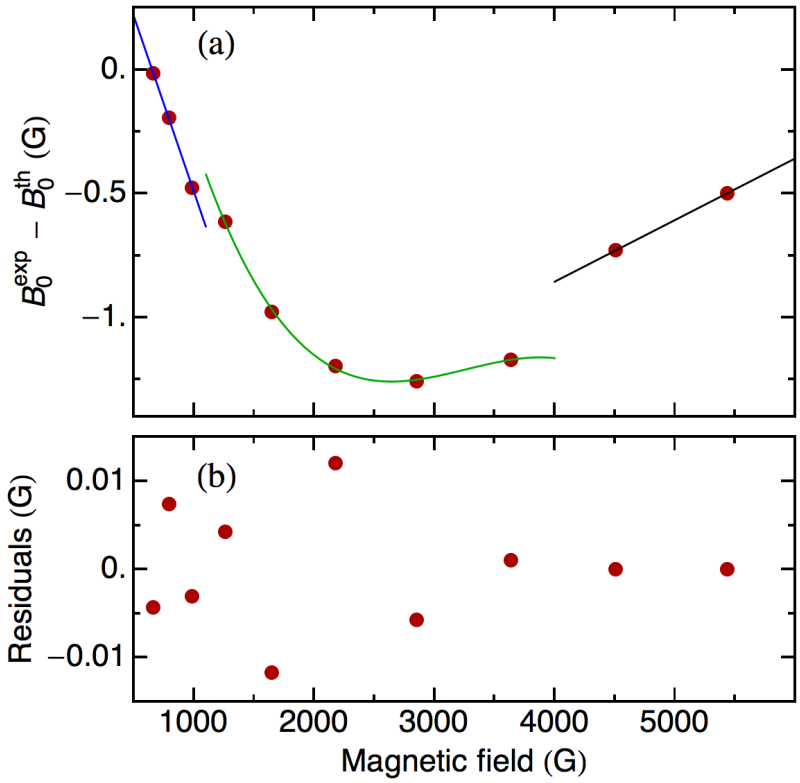

Figure 3-5: (a) Error in the measurement of the magnetic field experimentally determined over a large magnetic field range (600 − 5500 G). The experimental errors are shown in red points and the polynomial interpolations in blue, green and black. (b) Error residuals after magnetic field correction.

sample resistivity during the magnetic field scan. Note that because of our high power (80 mW) saturating excitation, i. e., making the populations of the ground- and excited-states the same, the conventional EPR absorption signal is suppressed. Such saturation is necessary to flip one of the spins in a pair of Bi and defect to induce SDR as we will discuss later.

Let us now discuss whether the experimental conditions we employed are sufficient to achieve the intrinsic linewidth and shape of the Bi donor spin transitions. In the duration of a single measurement, the microwave frequency of the EPR spectrometer drifts typically by ±5 kHz. The signal generated at 7 GHz by an Agilent 8257D

microwave source in series with a 3-W MiniCircuits ZVE-8G+ amplifier exhibits a frequency stability of ± 1.5 kHz for the same duration. These fluctuations in the applied microwaves lead to a maximum line broadening of $\pm 2.5 \times 10^{-3}$ G at 9 GHz and $\pm 1 \times 10^{-3}$ G at 7 GHz, which is negligibly small compared to the estimated $\gtrsim 10^{-2}$ G precision in magnetic field and its inhomogeneity.

A typical calibration curve of the magnetic field meter is shown in Fig. 3-5. The error in the measurement of the magnetic field [Fig. 3-5(a)] is determined over a large magnetic field range ($600 - 5500$ G), using a bulk doped ^{28}Si:Bi reference sample at 16 K. It is defined as the difference between the measured B_0^{exp} and the expected B_0^{th} resonant fields of the ten cw-EPR transitions of Bi donors. The three polynomial interpolation curves correspond to the three regimes of the magnetic field sensor [A: $500 - 1100$ G (blue), B: $1100 - 4000$ G (green) and C: $4000 - 6000$ (black)]. The residuals [Fig. 3-5(b)] are defined by the difference between the measured errors and the interpolation curves. The estimated $\gtrsim 10^{-2}$ G precision in magnetic field is deduced from the maximum value of the residuals.

3.3 Samples preparation

Two types of samples are employed; a silicon crystal enriched to 99.983% in ^{28}Si ([^{29}Si] = 90 ppm and [^{30}Si] = 80 ppm) with a resistivity $\approx$ 10 Ω·cm and a highly resistive (> 3 kΩ·cm) float-zone ^{nat}Si. These two substrates are ion-implanted with Bi and are labeled ^{28}Si:Bi and ^{nat}Si:Bi, respectively. The ion implantations are performed at room temperature with the total fluence of 2×10^{13} cm^{-2}. The implantation energies are 300 and 550 keV with the doses of 0.7×10^{13} and 1.3×10^{13} cm^{-2}, respectively. These conditions yield a maximum bismuth concentration of 1.8×10^{18} cm^{-3} (above the solubility limit [4]) in the depth of 90 to 150 nm from the surface. The distribution

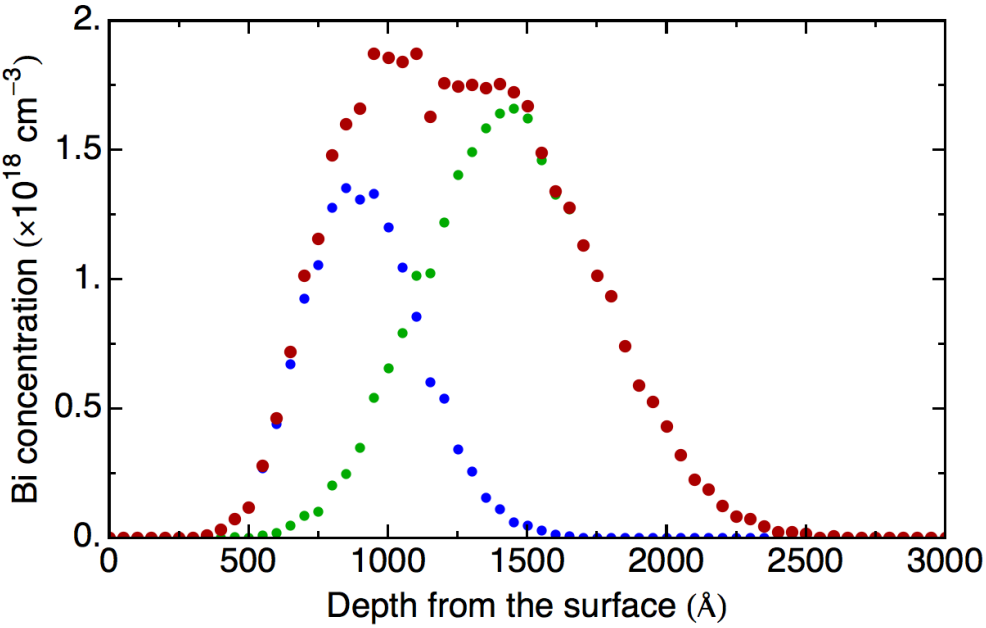

Figure 3-6: Simulated Bi atom concentration resulting from the ion implantation process described in section 3.3 shown as a function of the depth from the silicon surface. For the simulation, 2×10^4 atoms were used. The blue dots correspond to the distribution of Bi atoms implanted at 300 keV and the green dots to 550 keV. The total distribution is represented by red dots. The simulations were performed using the "the stopping and range of ions in matter" software (SRIM).

of the Bi atom concentration is plotted in Fig. 3-6 as a function of the depth. The post-implantation annealing, performed at 650 °C for 30 min in an evacuated quartz tube, leads to an activation efficiency [5, 6, 7, 8] below 60%, resulting in the Bi donor concentration less than 1.1×10^{18} cm^{-3} (below the metal-insulator transition [9]). This process is designed to maximize the number of the D-R pairs, instead of fully activating the implanted Bi atoms [10].

Bibliography

[1] F. Hoehne, L. Dreher, M. Suckert, D. P. Franke, M. Stutzmann, and M. S. Brandt, Phys. Rev. B **88**, 155301 (2013). (Cited on pages 36.)

[2] D. J. Lepine, Phys. Rev. B **6**, 436 (1972). (Cited on pages 37 and 66.)

[3] P. A. Mortemousque, T. Sekiguchi, C. Culan, M. P. Vlasenko, R. G. Elliman, L. S. Vlasenko, and K. M. Itoh, Appl. Phys. Lett. **101**, 082409 (2012). (Cited on pages 37, 66, 88, and 93.)

[4] F. A. Trumbore, Bell Syst. Tech. **39**, 205 (1960). (Cited on pages 42.)

[5] O. J. Marsh, R. Baron, G. A. Shifrin, and J. W. Mayer, Appl. Phys. Lett. **13**, 199 (1968). (Cited on pages 43.)

[6] R. Baron, G. A. Shifrin, O. J. Marsh, and J. W. Mayer, J. Appl. Phys. **40**, 3702 (1969). (Cited on pages 43.)

[7] J. P. de Souza and P. F. P. Fichtner, J. Appl. Phys. **74**, 119 (1993). (Cited on pages 43.)

[8] C. D. Weis, C. C. Lo, V. Lang, A. M. Tyryshkin, R. E. George, K. M. Yu, J. Bokor, S. A. Lyon, J. J. L. Morton, and T. Schenkel, Appl. Phys. Lett. **100**, 172104 (2012). (Cited on pages 43, 46, and 65.)

[9] E. Abramof, A. Ferreira da Silva, B. E. Sernelius, J. P. de Sousa, and H. Boudinov, Phys. Rev. B **55**, 9584 (1997). (Cited on pages 43.)

[10] P. Studer, S. R. Schofield, C. F. Hirjibehedin, and N. J. Curson, Appl. Phys. Lett. **102**, 012107 (2013). (Cited on pages 43.)

Chapter 4

Spin dependent recombination based magnetic resonance detection of bismuth donors in silicon

In this chapter, I show the results of SDR spectroscopy of Bi in ^{nat}Si. In section 4.2, I show the spectroscopy of the ESR lines recorded at X-band. The spectroscopy of Bi-readout center cross-relaxations is shown and analyzed in section 4.3. Following this, I show the results of the SDR detection of the NMR transitions in section 4.4. Then, in section 4.5, I explain the subtleties of the SDR processes in the low magnetic field regime. Further, I demonstrate the simultaneous detection of the donor electron spin (ESR transitions) and nuclear spins (NMR transitions) in section 4.6.

4.1 Introduction

Among a variety of qubits investigated for the realization of solid-state quantum computers, superconducting qubits are the leading candidates for quantum processors because of their fast operation capabilities ($\pi/2$ pulse shorter than 10 ns) [1]. However, the shortcoming of their relatively fast decoherence time needs to be overcome by connecting to memory qubits that can store quantum information throughout the course of computation. This requires memory qubits working under low magnetic field, typically below 50 Oe for aluminum(Al)-made superconducting qubits [2, 3], since they cannot operate at higher fields.

In this context, the bismuth (Bi) donor in silicon (Si) has attracted much attention recently. Its large hyperfine interaction $a/h = 1.4754$ GHz (Ref. [4]) and the ^{209}Bi nuclear spin $I = 9/2$ give a large zero-field splitting of 7.4 GHz. This splitting is comparable to the typical energy splitting between $|R\rangle$ and $|L\rangle$ states of superconducting flux qubits [1, 5]. Thus, coupling between a Bi spin qubit and a superconducting flux qubit on Si is in principle possible via a microwave photon through a waveguide. A proposal of such an application [6] has prompted extensive research on the Bi donor spins in Si very recently [6, 7]. Starting from the spectroscopic analysis of the electron paramagnetic resonance (EPR) [7, 8], the electron spin relaxation time T_1 [6, 9], decoherence time T_2 [6, 9, 8], and superhyperfine interaction with nearby ^{29}Si nuclear spins [9] were investigated. Moreover, the coherent transfer between electron and ^{209}Bi nuclear spins [7] and dynamic nuclear polarization of ^{209}Bi [6, 10] were achieved. Yet all of these EPR studies were performed at 9 GHz (around 320 mT) and at 240 GHz (around 8.6 T) excitation frequency.

In this chapter, I report on low-field ($6-110$ mT) radio frequency ($20-400$ MHz) and microwave (8.141 GHz) magnetic resonance, as well as X-band (9 GHz) magnetic

resonance, of ion-implanted Bi donors in Si using a highly sensitive, spin dependent recombination based magnetic resonance (SDR-MR) method [11, 12, 13, 14].

4.2 Spin dependent recombination spectroscopy of bismuth donors at X-band

The SDR method requires a coupled pair of electron spins [15, 16, 17]. In the present study, the partner of the Bi donor electron spin is the electron spin of a deep paramagnetic readout center (R) which is supposed to be created during the implantation process and not completely removed by controlling the annealing conditions [18]. I have attempted to identify the symmetry of the deep PRC by tracing the angular dependence of the EPR peaks. However, the peaks were too broad to draw conclusions.

The X-band (9.076 GHz) SDR-MR spectrum measured without radio frequency excitation is presented in Fig. 4-1(b). The peaks labeled as Bi-X and R indicate ten EPR-"allowed" transitions of the Bi donors and one EPR transition of a readout center, respectively, corresponding to the intersections with the 9.076 GHz excitation in Fig. 4-1(a). Here the EPR transition frequencies of the Bi donor (blue lines) [19] were calculated as functions of the static magnetic field B_0 using the spin Hamiltonian in Eq. (2.26) and that of R (green line) was calculated as an isotropic, nuclear spin free, paramagnetic center $S = 1/2$ and $g \approx 2.005(3)$. The same notation as in Ref. [19] for labeling Bi eigenstates is used; the spin levels are labeled from 1 to 20, in increasing order of energy.

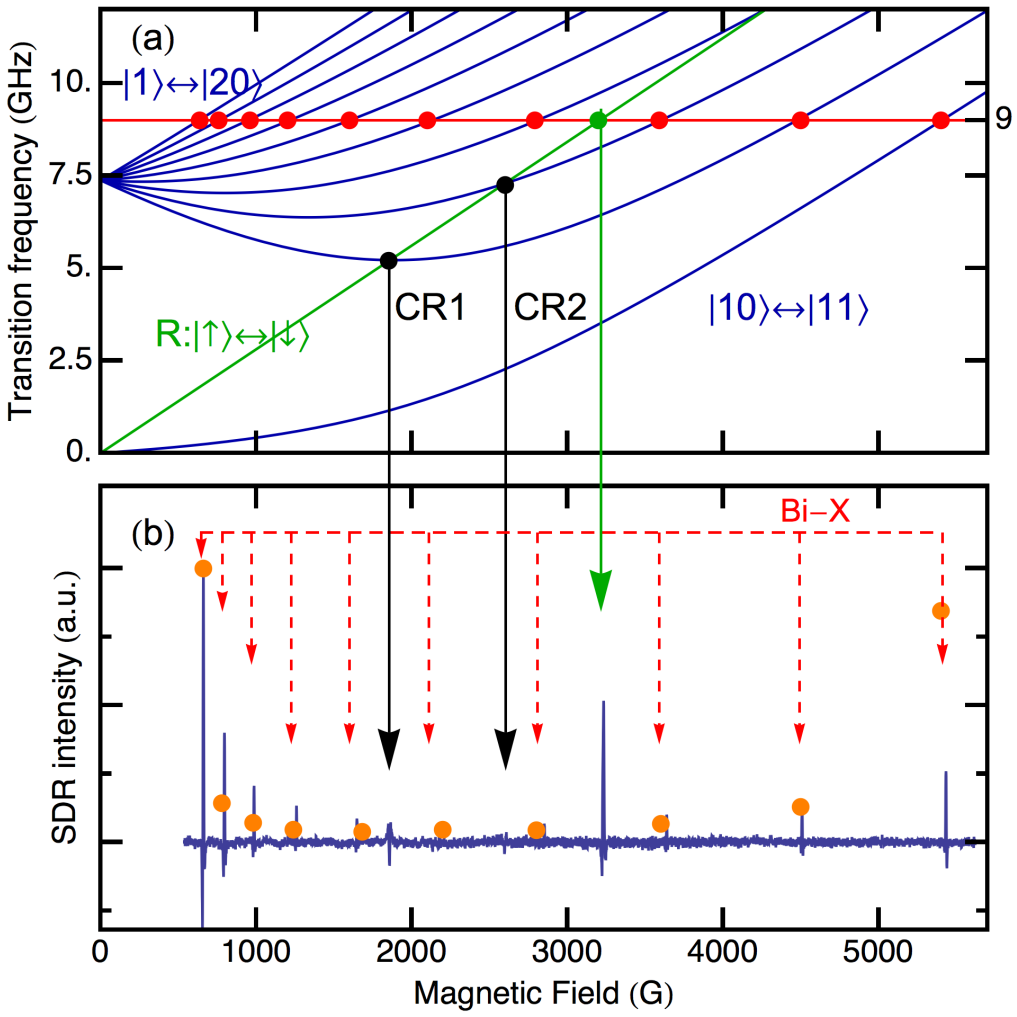

Figure 4-1: (a) Calculated EPR transition frequencies of Bi donors (blue lines) and deep paramagnetic readout center (R) (green line) with 9.076 GHz microwave excitation frequency (red line). The intersections of the readout center transition energy with bismuth donor transitions (black points) and with the 9.076 GHz microwave (green point) are also shown. (b) An SDR-MR spectrum of Bi donors in Si recorded at 16 K under illumination. The 9.076 GHz microwave is used both to induce Bi EPR transition and to probe the change in the sample photoconductivity. CR1 and CR2 are the signal detected at the cross relaxation signals between Bi and PRC. The orange points in (b) indicate simulated intensities using the SDR model described in the text with the parameter value of $R_{\mathrm{p}}/R_{\mathrm{ap}} = 0.01$.

4.3 Donor−readout center pair cross relaxations

In addition, two lines labeled as CR1 (186 mT) and CR2 (259 mT) arise due not to the resonance with the 9.076 GHz microwave but to cross relaxation (CR) between particular Bi donor transitions and the PRC transitions, in a way very similar to the cross relaxation between phosphorus donors and SL1 centers in Si observed by electrically detected magnetic resonance [20]. This assignment of CR1 and CR2 is further justified in Fig. 4-2. Even with the decrease in the microwave excitation frequency, the position of these lines remains the same whereas the Bi EPR line positions shift to lower fields. This proves the presence of coupling between the Bi donor and PRC electron spins, which is requisite for the SDR detection method.

I should emphasize that even at the same X-band resonance of the Bi donor, the observed SDR-MR line intensity distribution is clearly different from that observed in the conventional EPR spectra [6, 7, 19, 9]. The intensity differs for the ten different transitions in the present SDR-MR whereas it is practically the same in conventional EPR, reflecting simply the thermal equilibrium population difference between the involved levels. Furthermore, the observed line-dependence of the SDR-MR intensity is distinctively stronger than the line dependence in the EPR transition [19]. Actually, the signal intensity observed in EPR spectroscopy is a function only of geometric parameters (microwave cavity Q factor and filling factor), number of spins, the sample temperature and the detection frequency. At thermal equilibrium, the last two parameters define the electron spin polarization. (In the case of continuous wave EPR spectroscopy, the signal intensity also depends on the electron spin relaxation rate and the modulation parameters of the spectrometer.)

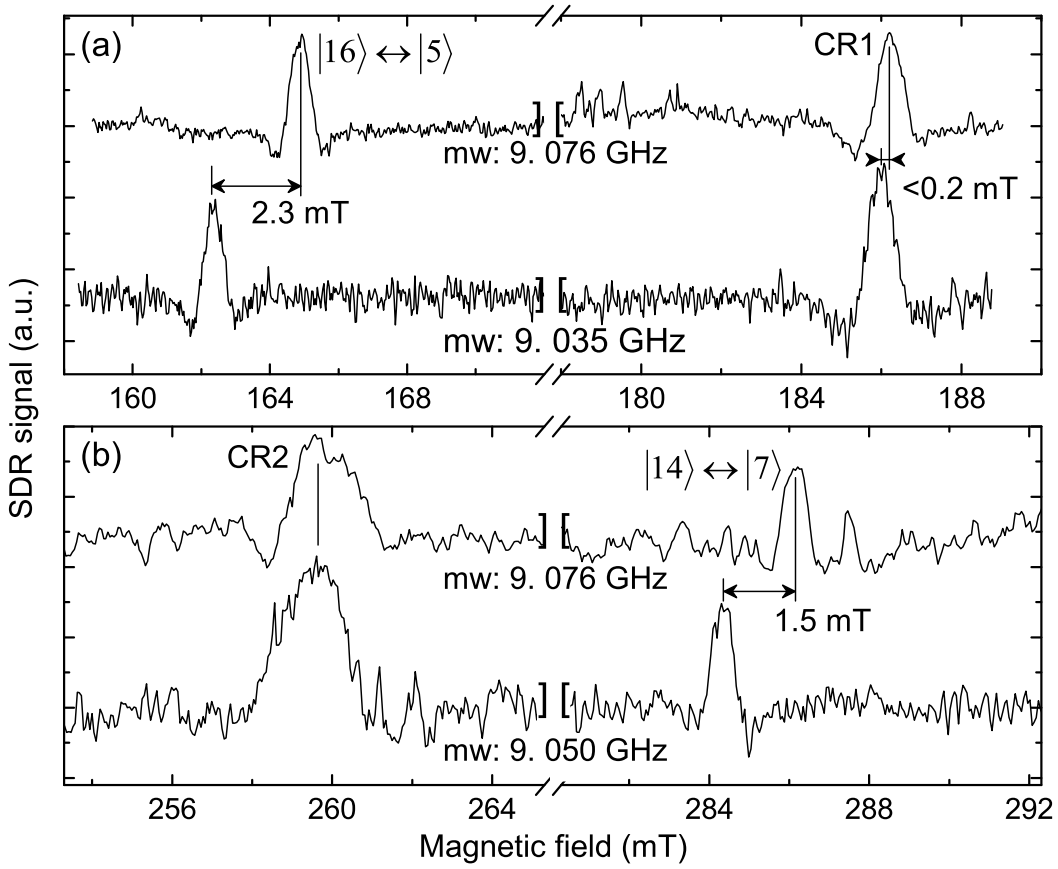

Figure 4-2: Cross relaxation lines CR1 (a) and CR2 (b) together with SDR-MR Bi lines detected at different microwave frequencies. The Bi EPR lines labeled as $|16\rangle \leftrightarrow |5\rangle$ in (a) and $|14\rangle \leftrightarrow |7\rangle$ in (b) shift with the resonant frequency whereas the lines CR1 and CR2 do not. Additionally, the CR1 line (full-width half-maximum FWHM = 1.0(2) mT) is narrower than CR2 (FWHM = 2.6(2) mT) because, as shown in Fig. 4-1(a), the difference in the field-derivative of the transition frequency between the readout center and resonant Bi transition is larger.

4.4 Spectroscopy of NMR transitions

Figure 4-3(a) shows the observed SDR-MR line positions (green and red points) for radio frequency excitation ranging from 20 to 400 MHz together with the calculated magnetic resonance transition frequencies for the Bi donor (blue lines). All of these simulated Bi magnetic resonance transitions are the ^{209}Bi NMR transitions in the high field limit. While the number of calculated Bi NMR lines in (a) appears ten, all but the lowest- and highest-field lines are nearly-degenerate doublets, i.e., each is composed of two lines separated by exactly twice the nuclear Zeeman splitting energy. Figure 4-3(b) shows the SDR-MR spectra probed by the same X-band microwave but with additional radio frequency excitation of 200 MHz. Therefore, among the eighteen NMR transitions of the Bi donor excited by these radio frequencies, we observed clearly the two non-degenerate lines labeled as Bi-RF in Fig. 4-3. The remaining eight doublets are too weak to be observed with the current experimental conditions.

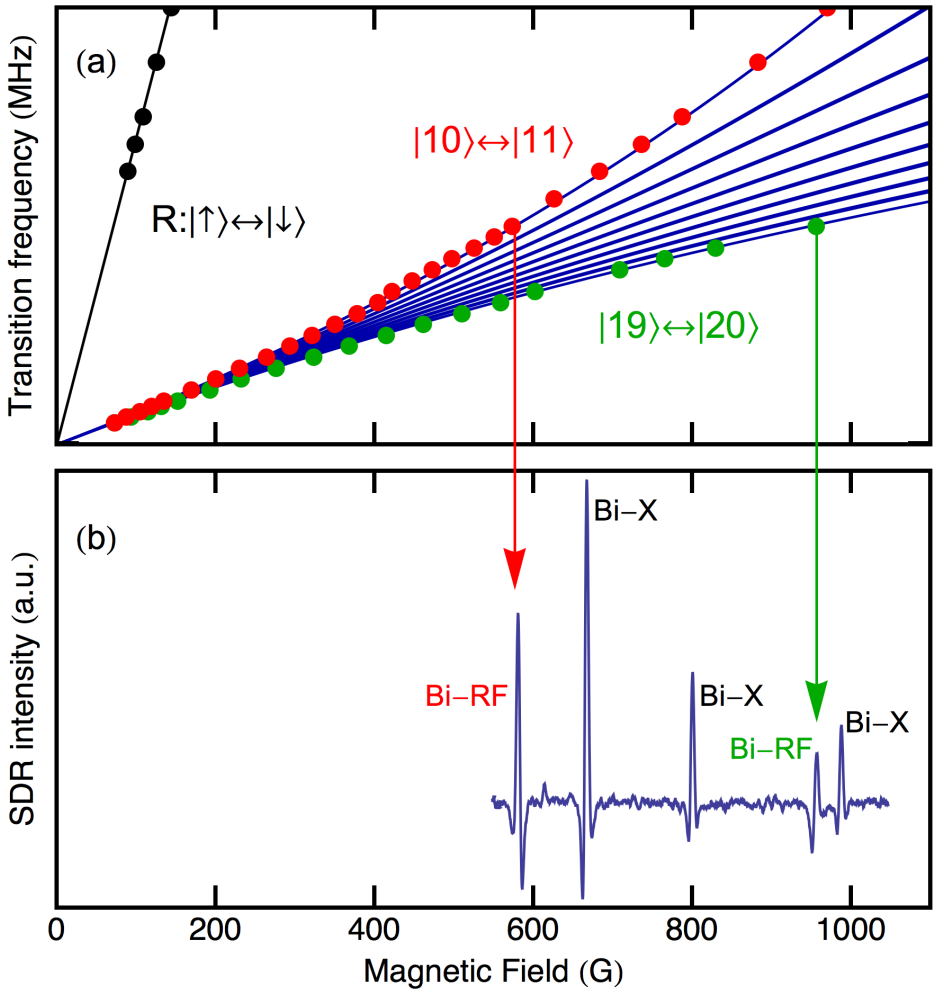

Figure 4-3: (a) The Bi-RF line positions observed at various resonant frequencies (green points for the transition $|19\rangle \leftrightarrow |20\rangle$ and red points for $|10\rangle \leftrightarrow |11\rangle$) together with calculated resonant fields (blue lines). (b) Low-field SDR-MR spectra with 50 and 200 MHz resonance frequencies together with simulation of the 200 MHz spectrum. The transitions excited by the radio frequencies and X-band 9.076 GHZ microwave are labeled as Bi-RF and Bi-X, respectively.

4.5 Signal intensity model

As mentioned above, considering only the EPR transition probabilities [19] is not sufficient to correctly describe the intensity of SDR-MR. In the following, I shall present a model, based on the SDR model developed in Refs. [21, 22, 23], to simulate the SDR-MR spectra that are shown in Fig. 4-1(a) and Fig. 4-3(a). The SDR signal intensity, measured by probing the microwave intensity reflected by the cavity, is linear to the sample photoconductivity σ. Its change by magnetic resonance through SDR process can be written as:

$$\Delta\sigma \propto -\sum_{i,\mu} R_{i,\mu} \left[N_{i,\mu}(w \to \infty) - N_{i,\mu}(w = 0) \right], \tag{4.1}$$

where the subscripts i and μ denote the Bi donor and PRC spin states, respectively. $R_{i,\mu}$ and $N_{i,\mu}$ are the recombination rate and the population of the specified pair. Here the square bracket represents the change in the population from off-resonance ($w = 0$) to saturated magnetic resonance ($w \to \infty$) conditions where w is the excitation rate. Equation (4.1) is valid when the recombination rates can be assumed dominant over the pair generation and dissociation rates as well as the spin-lattice relaxation and spin decoherence rates. Furthermore, if only one transition between two Bi states i and j is selectively excited, the change in photoconductivity becomes:

$$\begin{aligned} \Delta\sigma(i,j) \approx -\sum_{\mu} \quad & [R_{i,\mu}N_{i,\mu}(\infty) + R_{j,\mu}N_{j,\mu}(\infty) \\ & -(R_{i,\mu}N_{i,\mu}(0) + R_{j,\mu}N_{j,\mu}(0))]. \end{aligned} \tag{4.2}$$

Using the rate equations described in Ref. [16], Eq. (4.2) simplifies to:

$$\Delta\sigma(i,j) \approx -\sum_{\mu}\left[\frac{4}{R_{i,\mu}+R_{j,\mu}} - \left(\frac{1}{R_{i,\mu}}+\frac{1}{R_{j,\mu}}\right)\right]. \tag{4.3}$$

The first term of Eq. (4.3) corresponds to the number of recombining pairs $-4/(R_{i,\mu}+R_{j,\mu})$ when the resonance is saturated whereas the second $1/R_{i,\mu}$ and third $1/R_{j,\mu}$ terms are the off-resonance terms. Thus, a large change in SDR signal should be obtained when either $R_{i,\mu}$ or $R_{j,\mu}$ is much smaller than the other. Finally, to evaluate the recombination rates $R_{i,\mu}$ and $R_{j,\mu}$, the product state of the Bi donor and the PRC is considered:

$$\begin{aligned} |i\rangle\,|\mu\rangle = \quad & (\cos\phi_i(B_0)\,|1/2, M-1/2\rangle \\ & + \sin\phi_i(B_0)\,|-1/2, M+1/2\rangle)\,|\mu\rangle\,. \end{aligned} \tag{4.4}$$

In the right-hand side, the Bi state ($i \in [1,20]$) is represented by the product of the electron ($m_S = \pm 1/2$) and nuclear spin ($-9/2 \leq m_I \leq 9/2$) states with the total spin z-component of $-5 \leq M \leq 5$ is represented on the basis of the electron (m_S) and nuclear (m_I) spin z-component eigenstates [24]. Note that there are two different Bi eigenstates for one particular M, except for $M = \pm 5$. The mixing angle $\phi_i(B_0)$ depends on the Bi state and is a function of the parameters in the Hamiltonian, Eq. (2.26), as explicitly described in Ref. [19]. Depending on the state of PRC ($\mu = \pm 1/2$, denoted by $\mu = \uparrow, \downarrow$), each term in Eq. (4.4) gives contribution to the recombination rate in terms of spin parallel (R_{p}) or anti-parallel (R_{ap}) pair:

$$R_{i,\uparrow}(B_0) = R_{\mathrm{p}}\cos^2\phi_i(B_0) + R_{\mathrm{ap}}\sin^2\phi_i(B_0), \tag{4.5}$$

$$R_{i,\downarrow}(B_0) = R_{\mathrm{p}} \sin^2 \phi_i(B_0) + R_{\mathrm{ap}} \cos^2 \phi_i(B_0). \tag{4.6}$$

Then, only the recombination associated with the pure states, $i = 10$ ($M = -5$) and $i = 20$ ($M = +5$), have single components that are strictly parallel or anti-parallel, while the other states have a mixture of the two components. This, in combination with Eq. (4.4), is the reason why the highest- and lowest-field lines, which involve the Bi state $|10\rangle$ or $|20\rangle$, are stronger than the other lines at X-band

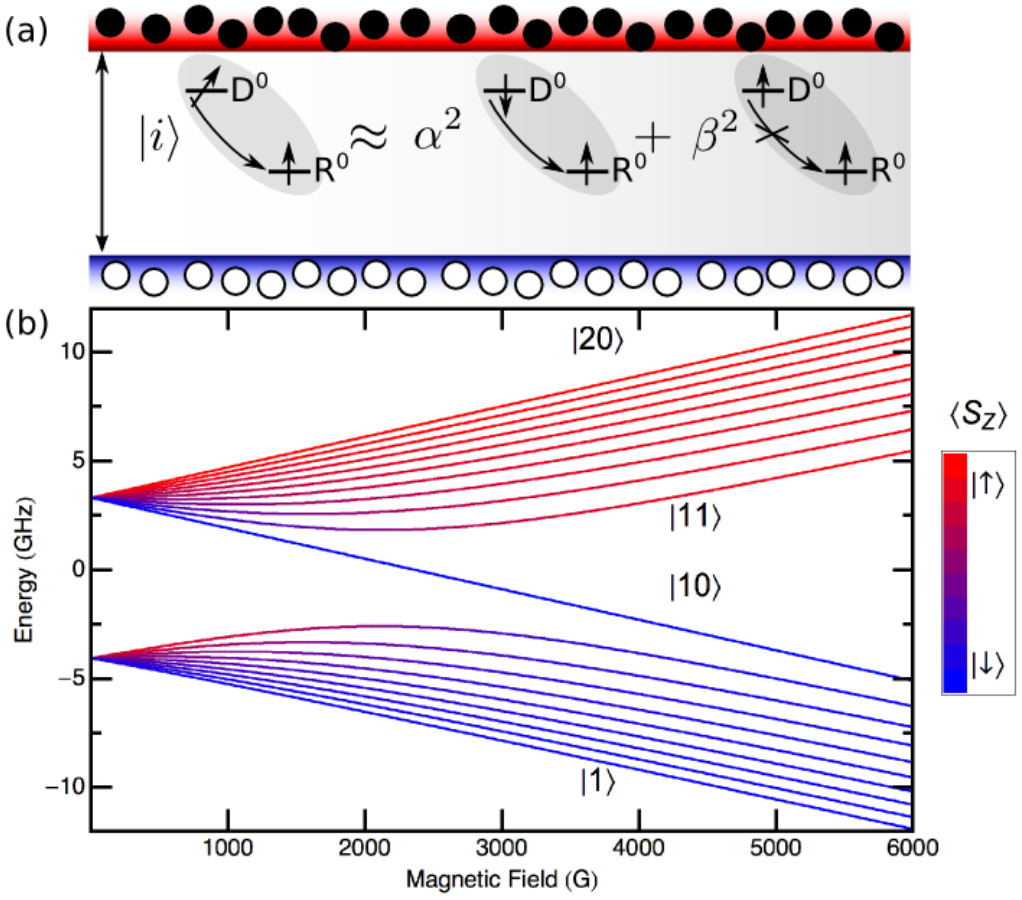

Figure 4-4: (a) Representation of the two competing recombination processes (parallel and antiparallel spin configurations) for an arbitrary donor electron spin state $|i\rangle$. α and β are the so called mixing coefficients described in Eq. (4.4). (b) Color plot of the expected value of the donor electron spin $\langle S_z \rangle$ for the twenty eigenvalues of the Bi donor spins.

resonance and exclusively strongest at the radio frequency resonance. I used this model to perform the simulation of the X-band spectrum in Fig. 4-1(b). The ratio $R_{\mathrm{p}}/R_{\mathrm{ap}} = 0.01$ has led to good agreement with the experiments and is comparable to the recently reported value $15\,\mu\mathrm{s}\,/\,2\ \mathrm{ms} = 0.0075$ for the phosphorus donor in Si [25]. Note that, for the X-band spectrum we also take into account that an EPR transition line that is "forbidden" in the high-field limit overlaps with each EPR-"allowed" one ($|1\rangle \leftrightarrow |20\rangle$, the lowest-field line that involves one pure state, has no overlapping forbidden transition [19]).

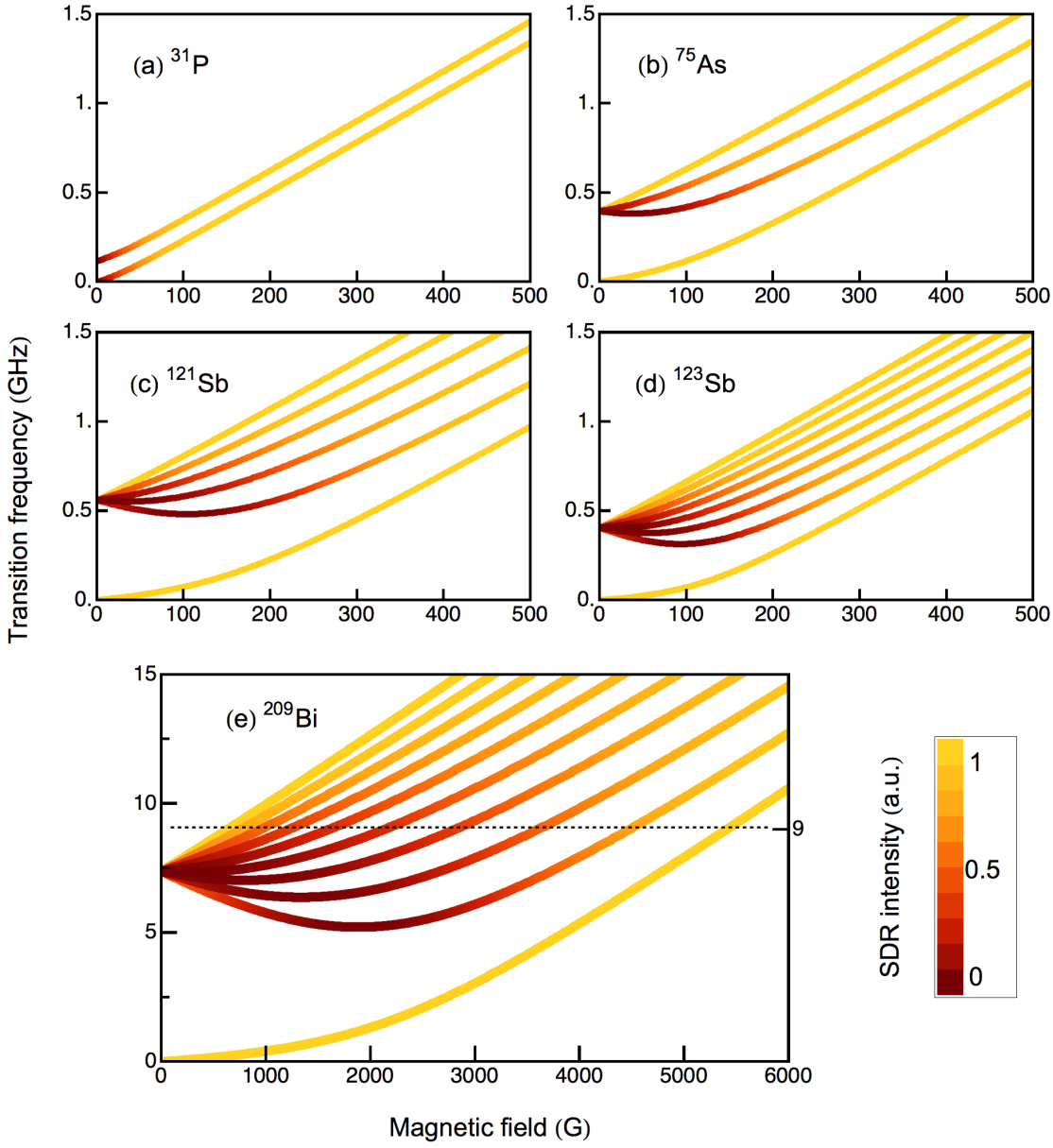

Figure 4-5: EPR transition frequencies of group-V donors in silicon, (a) ^{31}P, (b) ^{75}As, (c) ^{121}Sb, (d) ^{123}Sb and (e) ^{209}Bi. The color represents the expected SDR intensity for a conventional continuous wave measurement. Our model shows that the SDR intensity of the hyperfine clock transition HCT_{9-12} line for Si:Bi (defined in Chapt. 5) is much weaker than the intensities for the X-band $|1\rangle \leftrightarrow |20\rangle$ and $|10\rangle \leftrightarrow |11\rangle$ lines (see Chapter 5). This was observed experimentally in Fig. 5-1. The frequency scale for ^{209}Bi is ten times larger than the others.

4.6 Electron and nuclear spin resonance

Finally, I shall demonstrate the tunability of the resonance conditions of such "pure-state" transitions to the energy comparable to the superconducting qubits. As shown in Fig. 4-6(a), an additional 8.141 GHz microwave excitation in the same SDR method allows for successful excitation and detection of the EPR transition between Bi $|1\rangle$ and $|20\rangle$ levels at low field ($B_0 = 30$ mT). Although it is preferred to achieve $B_0 < 10$ mT for the coupling with the superconducting qubit, Fig. 4-6 shows clearly the flexibility to tune the energy difference between up and down states of the Bi electron spin. It is also possible to tune the superconducting flux qubit to match the energy between $|R\rangle$ and $|L\rangle$ states with the Bi transition frequency separating $|1\rangle$ and $|20\rangle$ states. The coupling strength between the flux qubit and Bi is expected in the range of $1 - 100$ kHz [5]. Figure 4-6(b) shows a result of a similar experiment but with two excitation frequencies generated by two coils perpendicular to each other. The second coil was used to irradiate 100-MHz excitation frequency. The Bi-RF and Bi-8 GHz resonance lines are observed together. Hence, this experimental setup allows us to perform SDR-MR with two arbitrary excitation frequencies.

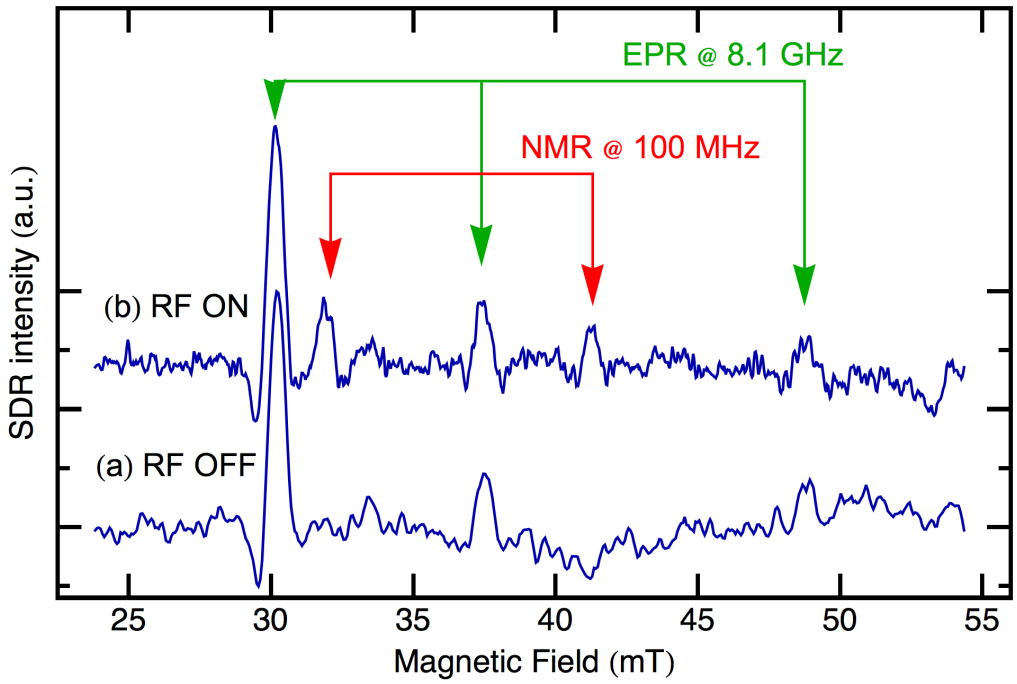

Figure 4-6: Low-field SDR-MR spectra probed by the 9.076 GHz X-band reflection (a) with a single 8.141 GHz excitation frequency and (b) with the same 8.141 GHz excitation plus an additional 100 MHz radio frequency. The lines resonant with the 8.141 GHz microwave and the 100 MHz radio frequency are labeled as EPR and NMR, respectively.

4.7 Conclusion

In summary, I have obtained the electron paramagnetic resonance spectra of a small number (5×10^{11}) of Bi donors in Si at low magnetic field ($6 - 110$ mT). The detection was based on the measurement of the sample photoconductivity which changed significantly at the time of resonance due to specific spin-dependent-recombination phenomena. The spin-dependent-recombination process takes place via coupling of the electron spins between Bi donors and nearby readout centers. The relative intensity of each resonance line has been described well by a spin-dependent-recombination model based on the mixing of Bi donor electron and nuclear spins.

Bibliography

[1] I. Chiorescu, Y. Nakamura, C. Harmans, and J. E. Mooij, Science **299**, 1869 (2003). (Cited on pages 2, 46, and 65.)

[2] J. F. Cochran and D. E. Mapother, Phys. Rev. **111**, 133 (1958). (Cited on pages 7, 46, and 65.)

[3] C. Reale, Acta Physica Academiae Scientiarum Hungaricae **37**, 53 (1974). (Cited on pages 7, 46, and 65.)

[4] G. Feher, Phys. Rev. **114**, 1219 (1959). (Cited on pages 29, 31, 46, 65, and 68.)

[5] X. B. Zhu, S. Saito, A. Kemp, K. Kakuyanagi, S. Karimoto, H. Nakano, W. J. Munro, Y. Tokura, M. S. Everitt, K. Nemoto, M. Kasu, N. Mizuochi, and K. Semba, Nature **478** (2011). (Cited on pages 4, 46, and 59.)

[6] G. W. Morley, M. Warner, A. M. Stoneham, P. T. Greenland, J. van Tol, C. W. M. Kay, and G. Aeppli, Nat. Mater. **9**, 725 (2010). (Cited on pages 7, 31, 46, 50, 65, 68, and 69.)

[7] R. E. George, W. Witzel, H. Riemann, N. V. Abrosimov, N. Noetzel, M. L. W. Thewalt, and J. J. L. Morton, Phys. Rev. Lett. **105**, 067601 (2010). (Cited on pages 7, 46, 50, 65, and 69.)

[8] C. D. Weis, C. C. Lo, V. Lang, A. M. Tyryshkin, R. E. George, K. M. Yu, J. Bokor, S. A. Lyon, J. J. L. Morton, and T. Schenkel, Appl. Phys. Lett. **100**, 172104 (2012). (Cited on pages 43, 46, and 65.)

[9] M. Belli, M. Fanciulli, and N. V. Abrosimov, Phys. Rev. B **83**, 235204 (2011). (Cited on pages 46, 50, and 65.)

[10] T. Sekiguchi, M. Steger, K. Saeedi, M. L. W. Thewalt, H. Riemann, N. V. Abrosimov, and N. Notzel, Phys. Rev. Lett. **104**, 137402 (2010). (Cited on pages 46 and 65.)

[11] R. L. Vranch, B. Henderson, and M. Pepper, Appl. Phys. Lett. **53**, 1299 (1988). (Cited on pages 47.)

[12] L. S. Vlasenko, Y. V. Martynov, T. Gregorkiewicz, and C. A. J. Ammerlaan, Phys. Rev. B **52**, 1144 (1995). (Cited on pages 47.)

[13] R. Laiho, L. S. Vlasenko, and M. P. Vlasenko, Mater Sci Forum **196-** (1995). (Cited on pages 47.)

[14] R. Laiho, L. S. Vlasenko, and M. P. Vlasenko, Mater. Sci. Forum **196**, 517 (1995). (Cited on pages 47.)

[15] D. Kaplan, I. Solomon, and N. F. Mott, Journal De Physique Lettres **39** (1978). (Cited on pages 48.)

[16] R. T. Cox, D. Block, A. Herve, R. Picard, C. Santier, and R. Helbig, Solid State Commun. **25**, 77 (1978). (Cited on pages 48, 55, and 71.)

[17] H. Morishita, L. S. Vlasenko, H. Tanaka, K. Semba, K. Sawano, Y. Shiraki, M. Eto, and K. M. Itoh, Phys. Rev. B **80**, 205206 (2009). (Cited on pages 48.)

[18] V. Miksic, B. Pivac, B. Rakvin, H. Zorc, F. Corni, R. Tonini, and G. Ottaviani, Nucl Instrum Meth B **186** (2002). (Cited on pages 48.)

[19] M. H. Mohammady, G. W. Morley, and T. S. Monteiro, Phys. Rev. Lett. **105**, 067602 (2010). (Cited on pages 48, 50, 54, 55, 57, and 66.)

[20] W. Akhtar, H. Morishita, K. Sawano, Y. Shiraki, L. S. Vlasenko, and K. M. Itoh, Phys. Rev. B **84**, 045204 (2011). (Cited on pages 50.)

[21] C. Boehme and K. Lips, Appl. Phys. Lett. **79** (2001). (Cited on pages 54.)

[22] C. Boehme and K. Lips, Phys. Rev. B **68**, 245105 (2003). (Cited on pages 54.)

[23] C. Boehme and K. Lips, *Charge transport in disordered solids*, Wiley (2006). (Cited on pages 54.)

[24] A. Abragam and B. Bleaney, *Electron paramagnetic resonance of transition ions*, Oxford University Press, Oxford, UK (1970). (Cited on pages 55.)

[25] L. Dreher, F. Hoehne, M. Stutzmann, and M. S. Brandt, Phys. Rev. Lett. **108**, 027602 (2012). (Cited on pages 57.)

Chapter 5

Hyperfine clock transition of bismuth donors in silicon

This chapter is dedicated to the spectroscopic study of the hyperfine clock transition of Bi donors in ^{28}Si and in ^{nat}Si. In section 5.2, I experimentally demonstrate the existence of such hyperfine clock transition for Si:Bi. Then, in section 5.2, the experimental results are modeled quantitatively by molecular orbital theory for a coupled pair consisting of a bismuth donor and a spin dependent readout center, including the effect of contact hyperfine and Zeeman interactions. In the section 5.5, I extend our simulation results of section 5.4 to other group V donors in silicon.

5.1 Introduction

Among a variety of physical systems investigated for quantum information processing, superconducting qubits are one of the promising candidates as quantum processors because of their fast operation capabilities and their potential for scalability [1]. However, because of their relatively fast decoherence rate which might be insufficient for maintaining quantum information throughout the course of computation, development of quantum memories that could support the operation of the superconducting processors are desired. Such memory qubits have to be addressable at low magnetic field (< 50 Oe for aluminum [2, 3]), since superconducting qubits become unoperable at magnetic fields higher than their critical fields.

Within this context, a bismuth (Bi) donor in silicon (Si) has attracted much attention recently. Its large hyperfine interaction $A = 1.4754$ GHz (Ref. [4]) and the ^{209}Bi nuclear spin $I = 9/2$ give rise to a large zero-field splitting of 7.4 GHz that is comparable to the typical energy splitting between $|R\rangle$ and $|L\rangle$ states of superconducting flux qubits [5]. Thus, coherent coupling between a Bi spin qubit in Si and a superconducting flux qubit on Si is in principle possible via a microwave photon traveling through a waveguide placed between the two qubits [6, 7]. The proposal to couple Bi in Si with a superconducting qubit [7] have triggered extensive fundamental studies of the Bi donor in Si very recently. Starting from the spectroscopic analysis of the electron paramagnetic resonance (EPR) [7, 8], the electron spin relaxation time T_1 [6, 9], decoherence time T_2 [6, 9, 8, 10, 11], and superhyperfine interaction with nearby ^{29}Si nuclear spins [9, 12] were investigated. Moreover, the coherent coupling between the Bi electrons and ^{209}Bi nuclear spins [7] and dynamic nuclear polarization of ^{209}Bi were achieved [6, 13]. Hybrid nuclear-electronic qubits consisting of superpositions of electronic and nuclear spin states have been used to demonstrate five

orders of magnitude longer coherence times than the manipulation times [14]. In order to extend the coherence time of Bi donor electrons, magnetic field-insensitive clock transitions can be used [11, 15, 12]. Also, at low temperatures, the presence of 4.7% ^{29}Si (I=1/2) in naturally available silicon (^{nat}Si) limits the coherence time of donors [16, 17] so that the use of isotopically purified ^{28}Si is helpful [18, 19, 11]. The fact that most of aforementioned Si:Bi studies were performed in the past three years shows how rapidly developing this field is. However, one aspect that has been scarcely studied is the investigation of Si:Bi at low-fields to enable the coupling to superconducting qubits. In order to fill in this gap, I have shown recently [20] that magnetic resonance spectroscopy with detection based on spin dependent recombination [21] (SDR) allows to manipulate and detect spins at low magnetic fields.

In the present study, using such a capable SDR technique, I perform spectroscopy of bismuth implanted in both ^{nat}Si and isotopically enriched ^{28}Si samples and observe a significant line narrowing at the hyperfine clock transition (HCT), where the transition frequency ν is insensitive to the change in A induced by variations in charge distribution ($\partial\nu/\partial A = 0$). While existence of optimal working points (e. g., gate voltages) at which superconducting qubits are immune to the electric charge noise has been demonstrated [22], observation of HCT in solid state systems has never been reported to our knowledge. The HCT is different from the conventional clock transition, which is insensitive to magnetic noise ($\partial\nu/\partial B_z = 0$). The conventional clock transitions are routinely employed in the operation of atomic clocks [23, 24] utilizing ^{133}Cs and trapped ions [25]. A similar clock transition of bismuth donors in silicon has been adopted to achieve extremely long donor electron spin coherence time [11]. HCT investigated in this study is more involved in the sense that the hyperfine interaction of a donor can be affected by both strain and electric field fluctuations. Away from

the HCT point, the interaction of a donor (D) electron with a nearby implantation defect, which is used in SDR spectroscopy as a readout center (R), causes an asymmetric broadening of the spectral line shapes. This interaction is equivalent to an effective electric perturbation. Thus I propose a theoretical model that describes the change of the donor wave function due to the presence of this readout center. This model makes it possible to simulate the SDR spectra and estimate the associated change in the hyperfine interaction. Finally, I compare the line position and the line shape measured by SDR spectroscopy with our calculation and extend the theoretical model for other donors in silicon.

5.2 Experimental observation of the change in hyperfine interactions

Lets recall from Chapt. 2, Eq. (2.26), the Bi donor spin Hamiltonian

$$\mathcal{H}_1 = g_e \mu_B B_z S_z - g_n \mu_N B_z I_z + hA\mathbf{S}\cdot\mathbf{I}, \tag{5.1}$$

where g_e and g_n are the donor electron and nuclear g-factors, respectively, and A the value of the isotropic hyperfine interaction in units of frequency. We label the i-th eigenstate in order of increasing energy as $|i\rangle$. The Breit-Rabi diagram of the bismuth donor is shown in Fig. 5-1(a). The Hamiltonian parameters used are summarized in Table 5.1, together with the ones extracted from the SDR data of this study. The sensitivity of the resonant magnetic field to a parameter p for a given resonant

Table 5.1: Magnetic resonance parameters of ^{28}Si:Bi and ^{nat}Si:Bi. The fractional changes in g-factor and in hyperfine interaction, are calculated as $(g_e^{\mathrm{SDR}} - g_e^{\mathrm{EPR}})/g_e^{\mathrm{EPR}}$ and $(A^{\mathrm{SDR}} - A^{\mathrm{EPR}})/A^{\mathrm{EPR}}$. The values for SDR[b,c] i.e., A^{SDR} (b, c) and g_e^{SDR} (c) are obtained from the fitting of the SDR peak positions by Eq. (5.1), assuming Gaussian distributed resonance peaks. SDR[b] is obtained using g-factor and A fitting parameters and SDR[c], utilizing the g factor determined at HCT_{9-12}, and A as fitting parameter.

^{28}Si:Bi	g_e	$\Delta g_e/g_e$ (ppm)	g_n	A (MHz)	$\Delta A/A$ (ppm)
EPR[a] [11]	2.00032	Ref.	0.9135	1475.17	Ref.
SDR[b]	2.00036(4)	+19(22)		1475.31(7)	+95(50)
SDR[c] [4]	2.00038(2)	+29(10)		1475.29(7)	+84(50)
^{nat}Si:Bi					
EPR[d, e] [4, 6]	2.0003	Ref.	0.914	1475.4	Ref.
SDR[c]	2.00049(5)	+93(25)		1475.05(17)	−240(120)

frequency ν is defined as $\delta B_z/\delta p$, which satisfies

$$\delta\nu = \frac{\partial\nu}{\partial p}\delta p + \frac{\partial\nu}{\partial B_z}\delta B_z = 0 \tag{5.2}$$

which leads to $\partial\nu/\partial A = -(\partial\nu/\partial B_z)(\delta B_z/\delta A)$. For $\partial\nu/\partial A$ to be zero, $\delta B_z/\delta A$ must be zero since when $\partial\nu/\partial B_z = 0$, $\delta A = 0$ (Ref. [11]) so that $\partial\nu/\partial A$ takes a finite value.

Figures 5-1(b−d) and 5-1(e−g) show cw SDR spectra of ^{nat}Si:Bi and ^{28}Si:Bi. The spectra recorded at the Bi donor HCT for $m_I = -7/2$ (7.3043 GHz for ^{nat}Si:Bi and 7.3054 GHz for ^{28}Si:Bi) between the states $|9\rangle$ and $|12\rangle$ [Figs. 5-1(c, f)] have a symmetric line shape whereas the X-band spectra of the $|1\rangle \leftrightarrow |20\rangle$ transition ($m_I = 9/2$) and the $|10\rangle \leftrightarrow |11\rangle$ transition ($m_I = -9/2$), shown in Figs. 5-1(b, e) and in Figs. 5-1(d, g), respectively, are asymmetric. At the HCT, the resonant field sensitivity to the hyperfine value $\delta B_z/\delta A$ is zero so that one can probe the Si:Bi linewidth and line shape not subject to such electric perturbations. The measured FWHM linewidth of the HCT lines are 6.7 G and 1.3 G for ^{nat}Si:Bi and for ^{28}Si:Bi, respectively. These values are significantly larger than the measured linewidth at X-band of 4.1 G for ^{nat}Si:Bi [6, 7] and the theoretical prediction of 0.08 G at the HCT_{9-12} for ^{28}Si:Bi [10]. In contrast, the X-band $|1\rangle \leftrightarrow |20\rangle$ transitions are asymmetrically broadened (FWHM linewidths of 7.7 G and 1.6 G) toward high field and the $|10\rangle \leftrightarrow |11\rangle$ transitions toward low field (7.0 G and 1.4 G). m_I dependent asymmetry directions can be described by an (inhomogeneous) distribution of the hyperfine interaction but is inconsistent with any distribution of the Zeeman interaction.

The asymmetric line broadening of the $|1\rangle \leftrightarrow |20\rangle$ and $|10\rangle \leftrightarrow |11\rangle$ transitions is consistent with a distribution of the donor hyperfine interaction with a long tail

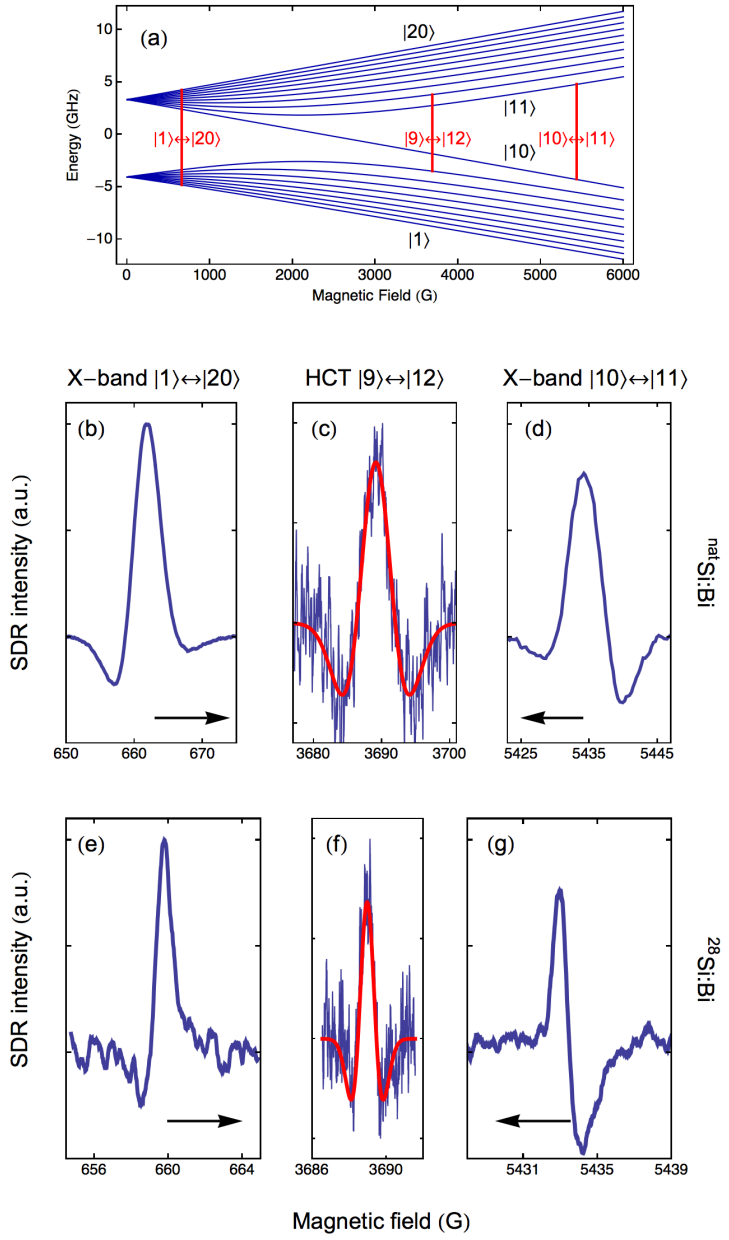

Figure 5-1: (a) Breit-Rabi diagram of the bismuth donor spins. The three vertical red lines correspond to the transitions shown in (b−g). cw SDR spectra of ^{nat}Si:Bi (b−d) and ^{28}Si:Bi (e−g). The FWHM linewidths of the HCT_{9-12} (c) and (f), obtained from the double integration of the fitting Gaussians (red lines), are 6.7 G for ^{nat}Si:Bi and is 1.3 G for ^{28}Si:Bi. Arrows indicate the direction of the asymmetric broadening directions. The signal-to-noise (S/N) ratios for $|9\rangle \leftrightarrow |12\rangle$ are worse than the others since the HCT_{9-12} line intensity for Si:Bi is much weaker than the intensities for the X-band $|1\rangle \leftrightarrow |20\rangle$ and $|10\rangle \leftrightarrow |11\rangle$ lines as will be shown theoretically in Fig. 5-12.

toward low hyperfine couplings. From the line shapes of the spectra in Figs. 5-1 (b, d, e and g), the asymmetric part of the line broadening can be estimated roughly to 1 G, corresponding to a distribution of the hyperfine constant A toward lower values by 3 MHz. I can exclude the distribution in the donor g-factor as a cause of this asymmetric broadening, because the sensitivity $\delta B_z/\delta g_e$ is negative for both transitions so that the broadening for both $|1\rangle \leftrightarrow |20\rangle$ and $|10\rangle \leftrightarrow |11\rangle$ transitions would be in the same direction. The spin exchange interaction $J\,\boldsymbol{S_D}\cdot\boldsymbol{S_R}$ (Ref. [26]) between the two electrons of the SDR pair can also be ruled out as it would yield a symmetric line broadening for low enough couplings, estimated by Lu *et al.* [27] to

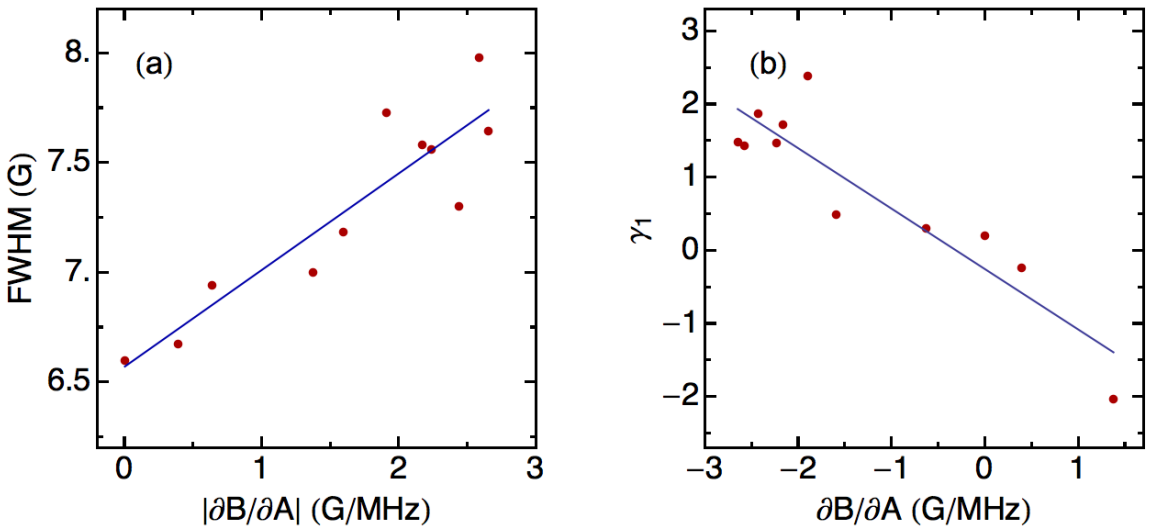

Figure 5-2: (a) Experimentally measured FWHM of the ten X-band peaks of ^{nat}Si:Bi plotted as a function of the hyperfine interaction sensitivity $\left|\partial B/\partial A\right|$ of each transition (dark red points). The linear fit (blue line) is a guide for the eye. The minimal linewidth is measured at the HCT where the absolute sensitivity of the resonant field to the hyperfine interaction is zero. The transitions with the largest sensitivity shows a linewidth 20 % larger than at the HCT. (b) Experimentally determined skewness (3rd standard moment) [see Eq. (5.10)] of the ^{nat}Si:Bi peaks as a function of $\partial B/\partial A$ (dark red points). The blue line is a linear fit of the experimental points. The peak asymmetry is canceled at the HCT, whereas at other transitions, it agrees with an asymmetric distribution of the hyperfine interaction.

be below 5 MHz for phosphorus donor coupled to a surface dangling bond (^{31}P$-$P$_{b0}$) and below 10 kHz for separations larger than one donor Bohr radius a_B [28]. The values of $|\delta B_z/\delta J|$, $\delta B_z/\delta A$ and $\delta B_z/\delta g_e$ corresponding to each spectrum in Fig. 5-1 are summarized in Table 5.2. Figure 5-3 shows the simulation of the resonant field (x-axis) as a function of the exchange coupling intensity J ranging from 0 to 1000 MHz. The symmetric splitting at low J-coupling (below 400 mT) is confirmed. Also, the transition probability in the two branches of each transition is equal for low couplings.

Other possible causes for the observed asymmetric broadening would be the strain induced by the implantation damage that was not recovered fully by the post-implantation annealing process [29]. For shallow donors (P, As, Sb) in silicon, Wilson and Feher [30] and Dreher *et al.* [31] have shown that uniaxial macroscopic strain decreases the hyperfine interaction mainly through the valley repopulation of the ground-state Bloch function. Recently, the same sample as ^{nat}Si:Bi, Dreher (Ref. [32]) has shown that, despite the fact that Bi has a large electron binding energy of 71 meV, the strain decreases its hyperfine interaction in the manner similar to other shallow donors, by mixing the ground state A_1 with E-symmetry states. I have

Table 5.2: The resonant field (B_z) sensitivity to the g-factor g_e and to the hyperfine A for the Si:Bi transitions shown in Fig. 5-1. m_I represents the nuclear spin projection of the EPR transitions but is not a good quantum number for all these levels, expect for $|10\rangle$ and $|20\rangle$. The calculation was performed using the EPR magnetic resonance parameters shown in Table I.

Transition (spectrum in Fig. 5-1)	m_I	$\lvert\delta B_z/\delta J\rvert$ [G/MHz]	$\delta B_z/\delta g_e$ [10^3 G]	$\delta B_z/\delta A$ [G/MHz]
$\lvert 1\rangle \leftrightarrow \lvert 20\rangle$ (b, e)	9/2	0.08	-0.3	-1.9
$\lvert 9\rangle \leftrightarrow \lvert 12\rangle$ (c, f)	$-7/2$	0.06	-1.8	0
$\lvert 10\rangle \leftrightarrow \lvert 11\rangle$ (d, g)	$-9/2$	0.08	-2.7	1.4

further confirmed this experimental fact using ^{28}Si:Bi [see Fig. (5-4)]. To generate a uniaxial strain, the implanted side of the sample was glued to the quartz rod of the sample holder using a varnish resisting to low-temperature (GE 7031). The thin

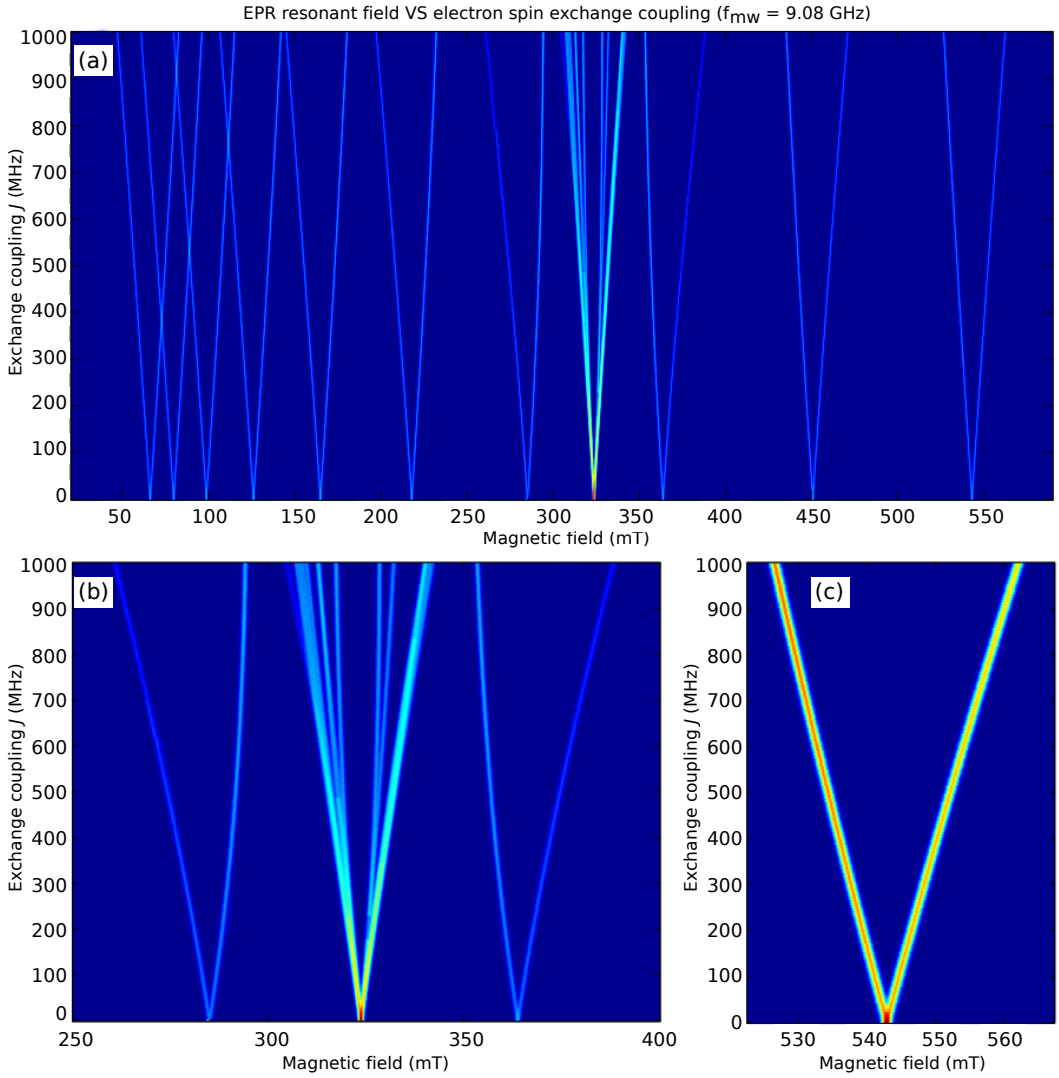

Figure 5-3: (a) Simulation of the resonant field of the two-electron and one nuclear spins system: Bi donor and readout center electrons. The simulation was performed for a microwave resonant frequency of 9.08 GHz. The ESR transition probability is plotted as a color scale (a.u.). Magnified views of the region between 250 and 400 mT (b), and of the region between 525 and 570 mT (c).

layer of varnish was transparent to light and the half cylindrical quartz rod was used as an optical lens to focus light on the implanted region of the sample. The ratio of the thermal expansion coefficients of quartz over silicon is $\alpha_{\text{quartz}}/\alpha_{\text{Si}} \approx 10$ for the temperature range $16 - 300$ K [33, 34]. As the glue is dried at room temperature, when cooling the sample down to 16 K, the resulting maximal uniaxial strain in the sample due to the thermal expansion coefficients is $\epsilon_{33} \approx 10^{-4}$ along the normal to

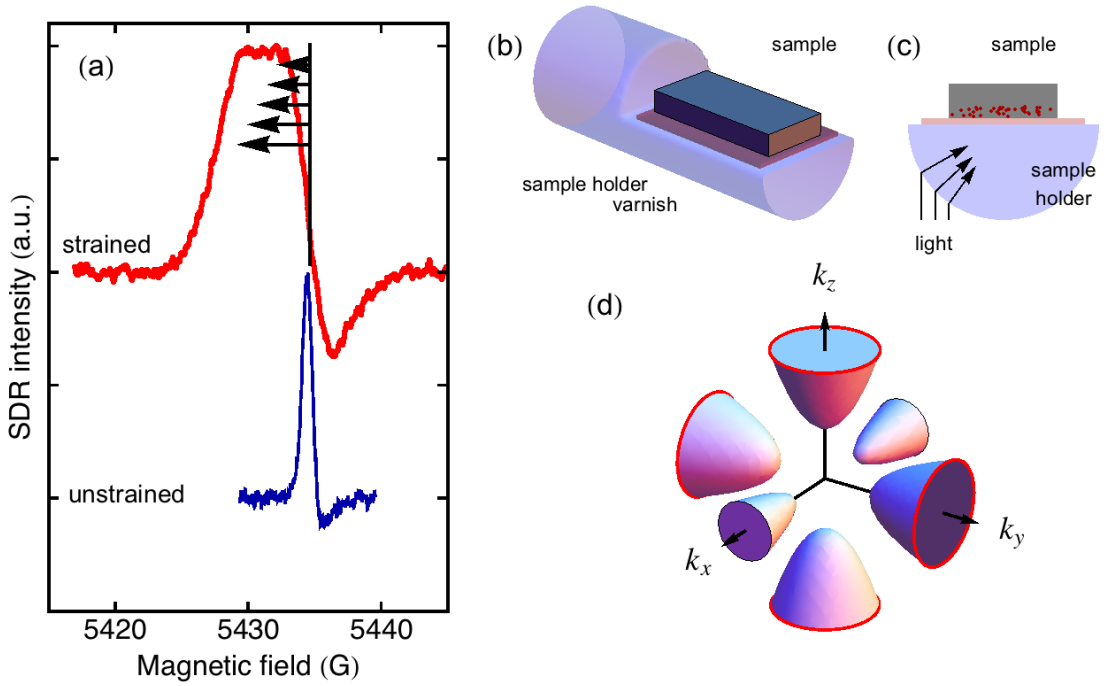

Figure 5-4: (a) cw SDR spectra of ^{28}Si:Bi without strain (blue) and with strain (red, see text). The vertical black line represents the resonant magnetic field of the $|10\rangle \leftrightarrow |11\rangle$ transition without strain and the horizontal arrow represents the peak distribution shift under strain uniaxial strain. The largest shift of the peak at 16 K is 5 G. (b) Schematic representation of the sample glued to the sample hold quartz rod. (c) Cross-sectional view of the schematic representation of (b). (d) Illustration of the valley repopulation process under uniaxial [100] strain. The A_1 symmetry of the Bloch wave function is broken. The donor electron wave function is mixed with E-symmetry wave functions (see section 2.1), decreasing the electron density at the donor nucleus, which in turns reduces the hyperfine interaction of the donor.

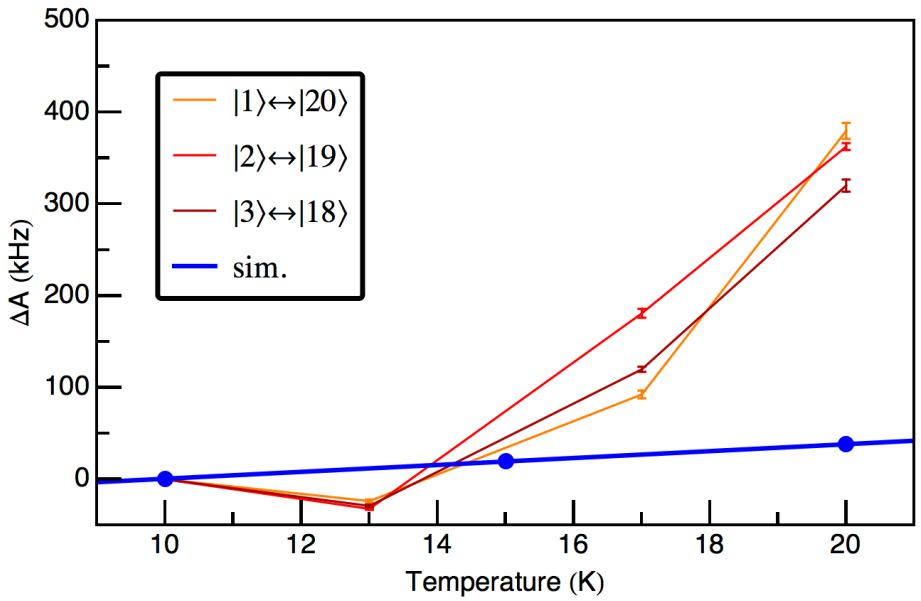

Figure 5-5: Change in hyperfine interaction estimated from cw SDR spectra of ^{nat}Si:Bi for the transitions $|1\rangle \leftrightarrow |20\rangle$, $|2\rangle \leftrightarrow |19\rangle$ and $|3\rangle \leftrightarrow |18\rangle$, for different temperatures. The lines between the experimental points are only a guide for the eye. The blue line is the simulated change in hyperfine due to the change in the Si lattice constant wight the temperature. This simulation includes only the change of the Bloch wave functions, calculated using the pseudo potential method (see section 2.1).

the sample surface. The measured SDR spectrum of the $|10\rangle \leftrightarrow |11\rangle$ in ^{28}Si:Bi under strain is shifted by about 5 G toward low magnetic field [Fig. 5-4(a)], corresponding to a decrease in the Bi donor hyperfine of 3.6 MHz. The peak broadening is due to the inhomogeneity in the applied stress.

However, the effective hyperfine of the Bi donors in ^{28}Si, obtained from the peak positions in the SDR spectra, is +84 ppm higher than the reported value for EPR measurements at the clock transition [11]. Thus the macroscopic strain cannot account for the observed positive shift in effective hyperfine interaction. This positive shift could be explained by a temperature difference of 3 K between the ESR measurement of the calibration ^{28}Si:Bi sample and the SDR measurement [see Fig. 5-5].

We ruled out this hypothesis as our control of the temperature was much more precise than this difference of 3 K (see section 3.2). In fact, the positive shift suggests that orbitals of the donor and the readout center electrons are coupled and their densities are redistributed. In this study, I thus describe the SDR pair in terms of a model based on the coupling between the electron orbitals of the pair in this study.

5.3 Calculation of the line shape with the spin dependent recombination model

One Bi donor electron and one readout center electron form a spin pair. In section 5.3.1, I introduce a theoretical model to describe this electron pair. Then, I evaluate the effect of the readout center on the donor hyperfine properties (section 5.3.2) and I discuss the influence of the model parameters on the line shape (section 5.3.3).

5.3.1 Wave function of the donor-readout center pair

The one-electron molecular orbitals corresponding to the neutral donor in the presence of an ionized readout center (D^0-R^+) and to a neutral readout center close to an ionized donor (D^+-R^0) are denoted by ϕ_D and ϕ_R, respectively. In a simplified picture, ϕ_D and ϕ_R can be expressed as a linear combination of the wave functions of the electron of an isolated donor χ_D and an isolated center χ_R so that $\phi_D = a_1\chi_D + a_2\chi_R$ and $\phi_R = b_1\chi_D + b_2\chi_R$. The linear coefficients $a_{1,2}$ and $b_{1,2}$ are calculated by applying

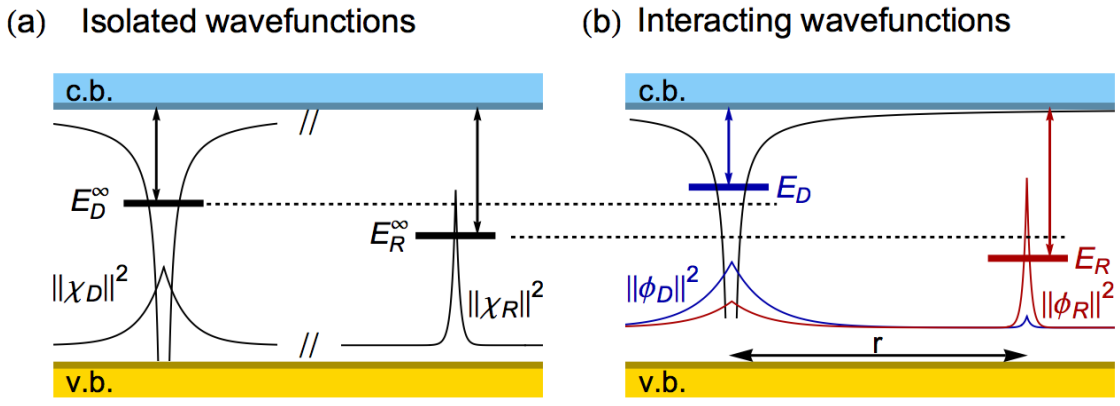

Figure 5-6: Energy diagrams of the donor and readout center in the silicon band gap for the isolated states (a) and for the molecular orbitals (b). The corresponding electron densities are also plotted, together with the Coulomb potential of the ionized donor.

the variational method to the one-electron Hamiltonian $\mathcal{H}_0 = K^* + V_D^* + V_R^*$ where K^* is the effective kinetic energy of the electron, V_D^* is the screened Coulomb potential of the donor, and V_R^* is the effective potential of the readout center. The difference in energy between these molecular states ϕ_i and the isolated states χ_i is small, even for a small spatial separation. This is due to the significant difference in the two orbitals

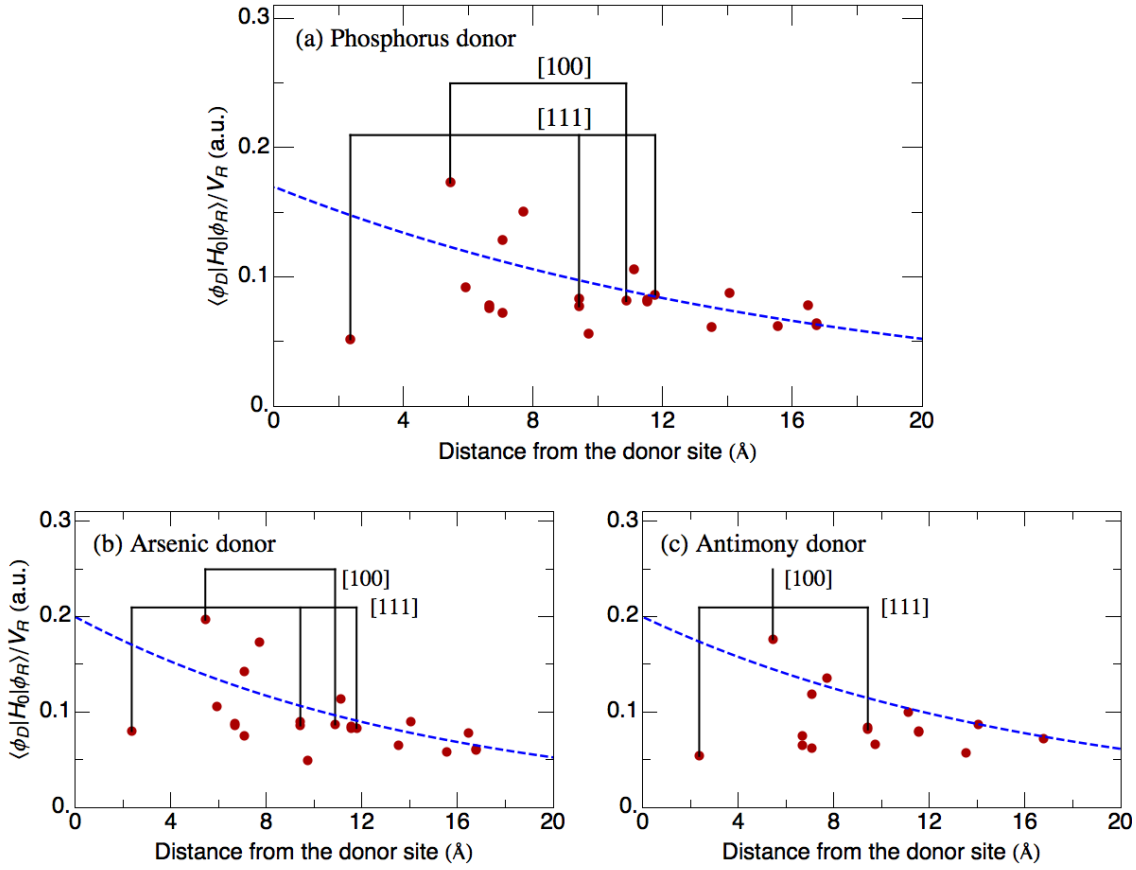

Figure 5-7: Estimated hopping probability of the donor electron to the readout center as a function of the spatial separation r between the donor D and the readout center R. The readout center is model as a point defect located at a Si lattice site and the donor electron wave function was experimentally measured by Hale and Mieher [35] for phosphorus (a), arsenic (c) and antimony (c) in silicon. The dotted blue line is the calculated hopping probability assuming only the 1s envelope wave function with the Bohr radii of Table 2.3. For separations larger than the donor Bohr radii, the envelope functions suffice to predict the experimentally estimated hopping probability.

χ_D and χ_R. The electron densities $|\chi_D|^2$ and $|\chi_R|^2$ are plotted in Fig. 5-6(a), and those of the one-electron molecular orbitals $|\phi_D|^2$ and $|\phi_R|^2$ in Fig. 5-6(b).

For readout centers close to the donor nucleus, a D-R pair cannot be formed: the more favorable energy levels of the readout center together with the large hopping probability of the electron from the donor site to the readout center prevent a free electron to be captured by the ionized donor. Therefore, in this model, we consider only the lattice sites far enough from D ($r > a_0$) as possible readout centers. This condition allows us to neglect the spatial oscillations of the electron density due to the Bloch wave functions as, far away from the donor site, its electron wave function is correctly modeled by the 1s envelop [see Fig. (5-7)], and central cell corrections do not have to be taken into account [36].

Antisymmetrized wave functions of the two-electron system, including the spin part, are constructed using the Slater determinant of the one-electron molecular orbitals:

$$\psi_1 = \phi_R \ \phi_R \, |0,0\rangle \otimes |m_I\rangle \tag{5.3a}$$

$$\psi_+ = 2^{-1/2} \left(\phi_D \ \phi_R + \phi_R \ \phi_D\right) |0,0\rangle \otimes |m_I\rangle \tag{5.3b}$$

$$\psi_- = 2^{-1/2} \left(\phi_D \ \phi_R - \phi_R \ \phi_D\right) |1,m_\sigma\rangle \otimes |m_I\rangle \tag{5.3c}$$

$$\psi_4 = \phi_D \ \phi_D \, |0,0\rangle \otimes |m_I\rangle \, . \tag{5.3d}$$

In the above, the spin states are denoted as $|\sigma, m_\sigma\rangle$ with $\sigma = S_D \pm S_R$ and the orbital products of the ϕ_i correspond, from left to right, to the first and the second electrons of the system. One notices that the spin singlet state ψ_+ (triplet ψ_-) behaves like a bonding (antibonding) orbital. Note that these states correspond to the charge states $D^+ - R^-$, $D^0 - R^0$ (σ=0), $D^0 - R^0$ (σ=1) and $D^- - R^+$, respectively.

Furthermore, the charge repulsion $1/r_{12}$ can be included. The corrected two-electron molecular orbitals Ψ_i are then written as linear combinations of ψ_i. Thus, the bonding orbital is $\Psi_+ = N_+^{-1}\big(\psi_+ + c_1\psi_1 + c_4\psi_4\big)$, where the coefficients are $c_1 = \frac{\langle\psi_1|1/r_{12}|\psi_+\rangle}{E_+ - E_1}$ and $c_4 = \frac{\langle\psi_4|1/r_{12}|\psi_+\rangle}{E_+ - E_4}$. Then, assuming a negatively charged donor (D^-) with an energy $\approx E_4 \gg E_+, E_1$, the coefficient c_4 tends to zero and the contribution of ψ_4 to Ψ_+ can be neglected. It follows that

$$\Psi_+ = N_+^{-1}\Big(\psi_+ + c_1\psi_1\Big). \tag{5.4}$$

In the coefficient c_1, the term $\langle\psi_1|1/r_{12}|\psi_+\rangle$ can be approximated as $\approx \sqrt{2}\,\theta\,E_{\rm corr}$ where $E_{\rm corr}$ is the two-electron correlation energy taken as the Coulomb repulsion of the electrons in the R^- state. In this model, $E_{\rm corr}$ is included in the parameter $\epsilon_{\rm corr} = E_{\rm corr}/(E_+ - E_1) \approx E_{\rm corr}/(E_+ - E_{R-})$. On the other hand, the antibonding spin triplet state ψ_- does not mix with either of the spin singlet states $\psi_{1,+,4}$, i. e., we have $\Psi_- = \psi_-$.

5.3.2 Change in hyperfine interaction

The Fermi hyperfine interaction for the two electrons is

$$\mathcal{H}_{\rm hyp} = -\frac{2}{3}\,\mu_0\;\boldsymbol{\mu}_{\rm Bi}\cdot\sum_{i=1}^{2}\boldsymbol{\mu}_i\rho_i(\boldsymbol{r}_{\rm Bi}), \tag{5.5}$$

where $\rho_i(\boldsymbol{r}_{\rm Bi})$ is the one-electron density at the bismuth nucleus. The electron magnetic dipolar moment $\boldsymbol{\mu}_i$ depends on the electron orbital function. As the two-electron orbitals can be expressed as functions of χ_D and χ_R, only two operators $\boldsymbol{\mu}_D = -g_D\,\mu_B\boldsymbol{S}_D$ and $\boldsymbol{\mu}_R = -g_R\,\mu_B\boldsymbol{S}_R$ are relevant, where g_D and g_R are the g-

factors of the isolated donor and readout center electrons, respectively. In order to simulate the SDR line shape, we only consider the change in the electron distribution while assuming the g-factor of the isolated centers. However, due to the confined nature of the readout center, only the χ_D component has a significant electron density at the bismuth nucleus. Then, in the rest of this section, the subscript of ρ_D is dropped.

Now, if one considers the hyperfine interaction A_{m_R} for a given spin projection

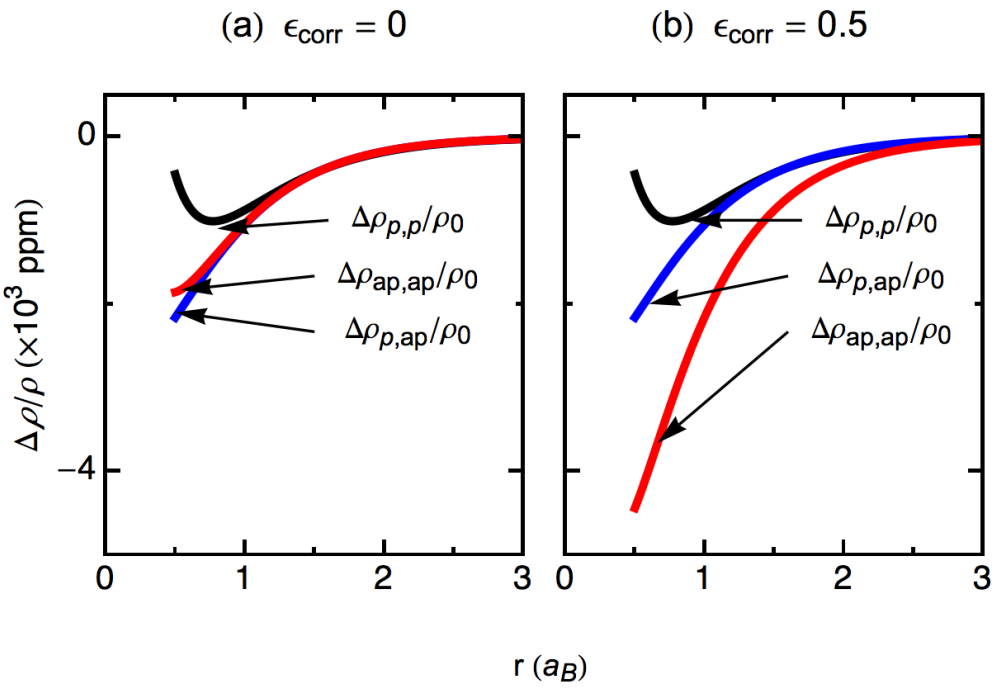

Figure 5-8: Fractional changes in the electron density ρ for three different electron spins configurations plotted as a function of the separation r between the donor and the readout center in units of a_B. ρ_0 corresponds to the isolated bismuth donor. A typical fractional change of -2×10^3 ppm corresponds to a change of the Bi hyperfine interaction of -3 MHz.

m_R of the readout center, one finds that

$$\left\langle m_R = 1/2 \middle| \mathcal{H}_{\text{hyp}} \middle| m_R = 1/2 \right\rangle = \begin{pmatrix} \mathcal{A}_{p,p} & \mathcal{A}_{p,ap} \\ \mathcal{A}_{ap,p} & \mathcal{A}_{ap,ap} \end{pmatrix} \tag{5.6}$$

$$\left\langle m_R = -1/2 \middle| \mathcal{H}_{\text{hyp}} \middle| m_R = -1/2 \right\rangle = \begin{pmatrix} \mathcal{A}_{ap,ap} & \mathcal{A}_{p,ap} \\ \mathcal{A}_{ap,p} & \mathcal{A}_{p,p} \end{pmatrix} \tag{5.7}$$

where each $\mathcal{A}_{j,k}$ on the right-hand side is a block matrix of dimension $2I+1$, calculated using the electron density $\rho_{j,k}$ with subscripts indicating the parallel and antiparallel electron spin configurations: $\mathcal{A}_{p,p} = \left\langle \Psi_- \middle| \mathcal{H}_{\text{hyp}} \middle| \Psi_- \right\rangle$, $\mathcal{A}_{p,ap} = \left\langle \Psi_- \middle| \mathcal{H}_{\text{hyp}} \middle| (\Psi_- - \Psi_+)/\sqrt{2} \right\rangle = \left\langle \Psi_- \middle| \mathcal{H}_{\text{hyp}} \middle| (\Psi_- + \Psi_+)/\sqrt{2} \right\rangle$ and $\mathcal{A}_{ap,ap} = \left\langle (\Psi_- - \Psi_+)/\sqrt{2} \middle| \mathcal{H}_{\text{hyp}} \middle| (\Psi_- - \Psi_+)/\sqrt{2} \right\rangle = \left\langle (\Psi_- + \Psi_+)/\sqrt{2} \middle| \mathcal{H}_{\text{hyp}} \middle| (\Psi_- + \Psi_+)/\sqrt{2} \right\rangle$. On the other hand, the off-diagonal blocks $\left\langle m'_R \middle| \mathcal{H}_{\text{hyp}} \middle| m_R \right\rangle$ for $m'_R \neq m_R$ give a contribution only at the second and higher orders, which are neglected in this model. The simulation of the fractional change in the electron density at the donor nucleus $\Delta\rho/\rho_0$ was performed using a single exponential envelope function characterized by the Bohr radius $a_B = 8.1$ Å for the Bi donor electron and a Dirac function for the readout center. $\Delta\rho/\rho_0$ is plotted in Fig. 5-8 for a readout center energy of -0.55 eV, and repulsion energy parameters $\epsilon_{\text{corr}} = 0$ (a) and $\epsilon_{\text{corr}} = 0.5$ (b). One notices that a large repulsion energy parameter decreases the hyperfine interaction for the electron spin pair in the triplet configuration.

5.3.3 Spin dependent recombination model parameters

The present model contains three physical parameters for a given donor in silicon: the concentration of readout centers N_R, and two parameters E_R and ϵ_{corr} related to

the energy levels of the readout center. In order to discuss the effect of the model parameters on the spectral line shapes, it is required to know how much each SDR pair contributes to the detected SDR signal as a function of the pair separation distance.

Among all the readout centers interacting with a donor, we assume that the closest one exclusively forms the most efficient recombination pair. Then, in the ensemble measurement, each donor has a different separation r to the nearest readout center and, therefore, a different recombination time in the anti-parallel spin configuration, τ_{ap}. However τ_{ap} is much shorter than the pair creation time τ_{ec}, i. e., $\tau_{ap} \ll \tau_{ec} \ll \tau_p$, the signal intensity from a single D-R pair is determined by the electron capture time τ_{ec} and thus independent of r in cw SDR measurements. Then, the total intensity from an ensemble of D-R pairs should be determined directly by the distribution function of the D-R separation r. Here, I identify the concentration of the pair having the pair separation r as follows.

First, I assume that the SDR intensity is proportional to the probability $\mathcal{P}(r)\,dr$ of a Bi donor to find the nearest readout center at a distance between r and $r + dr$. This distribution can be written as[37]

$$\mathcal{P} = \frac{3}{\langle r_{RR} \rangle} \left(\frac{r}{\langle r_{RR} \rangle} \right)^2 \exp\left(-\frac{r^3}{\langle r_{RR} \rangle^3} \right) \tag{5.8}$$

where $\langle r_{RR} \rangle = (3V/4\pi N_R)^{1/3}$ is the average distance between the readout center and its nearest neighbor. Such distributions are plotted in Fig. 5-9(a), as a function of r in the unit of a_B, for three different concentrations N_R of the readout centers. By combining Eq. (5.8) with the dependence of the hyperfine A on the D-R separation r obtained in section 5.3.2, the distribution in resonant magnetic field for the transition $|10\rangle \leftrightarrow |11\rangle$ is calculated and shown by thin curves in Figs. 5-9 (b, c). Since the peak

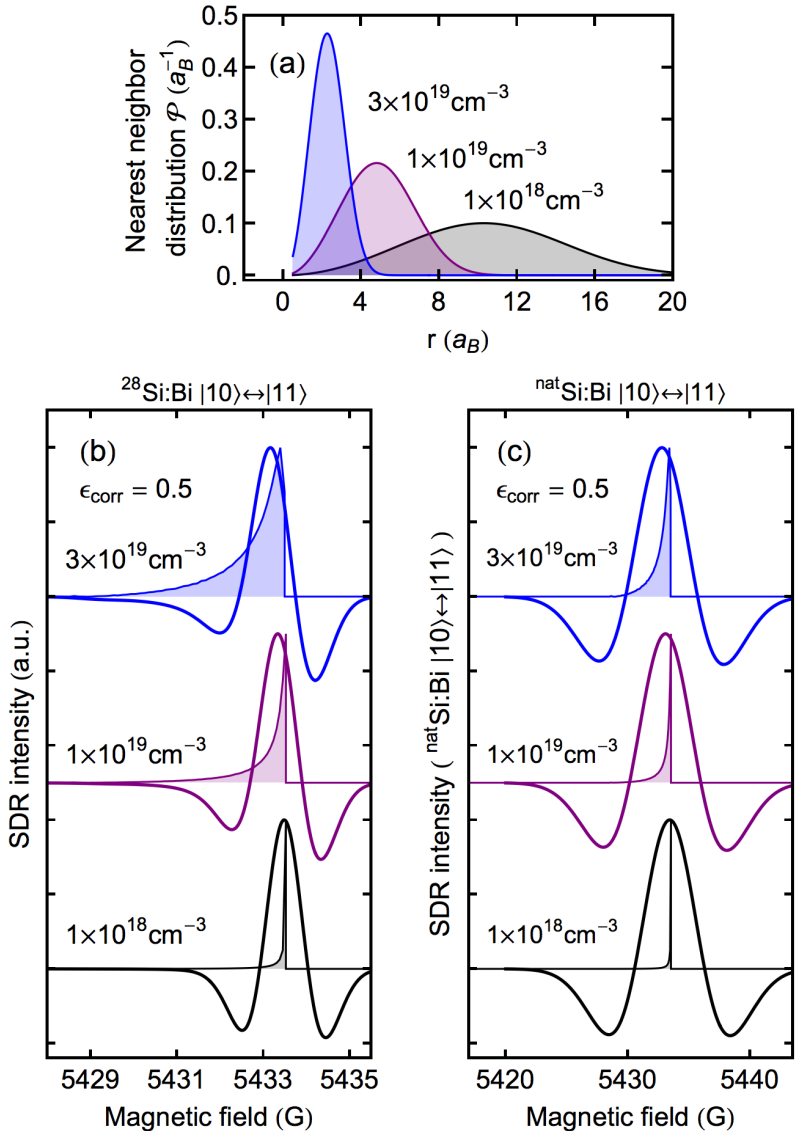

Figure 5-9: (a) Distributions of the separation r between the donor and its nearest readout center for various concentrations N_R. (b, c) Simulated distributions of the $|10\rangle \leftrightarrow |11\rangle$ transition taking into account only the SDR pair distribution (thin filled lines) and its convolution with the second derivative of a Gaussian (thick lines) for ^{28}Si:Bi (b) and ^{nat}Si:Bi (c). The donor and readout center pair with the small enough separation r have strong interaction and thus contribute to the low-field tail in the distribution of resonant magnetic fields (thin solid lines). The FWHMs of the HCT_{9-12} lines are 6.7 G for ^{nat}Si:Bi (c) and 1.3 G for ^{28}Si:Bi (f), each of which is obtained from the width parameter of the 2nd derivative of a Gaussian function fitted to the HCT line (red curves). Due to such linewidth difference, the shift of the peak position to low field is much larger in ^{nat}Si:Bi (larger field scale), while the degree of line shape asymmetry is more apparent in ^{28}Si:Bi, as N_R is increased.

for each r should be accompanied by a symmetric broadening due to inhomogeneous distribution of ^{29}Si nuclear spins in ^{nat}Si:Bi and of other Bi-donor and readout-center electron spins in ^{28}Si:Bi [as observed in Figs. 1(c) and 1(f)], the thin curves are convoluted with the second derivative of a Gaussian function to simulate the SDR spectra. The simulated spectra are shown as the thick curves in the same figures.

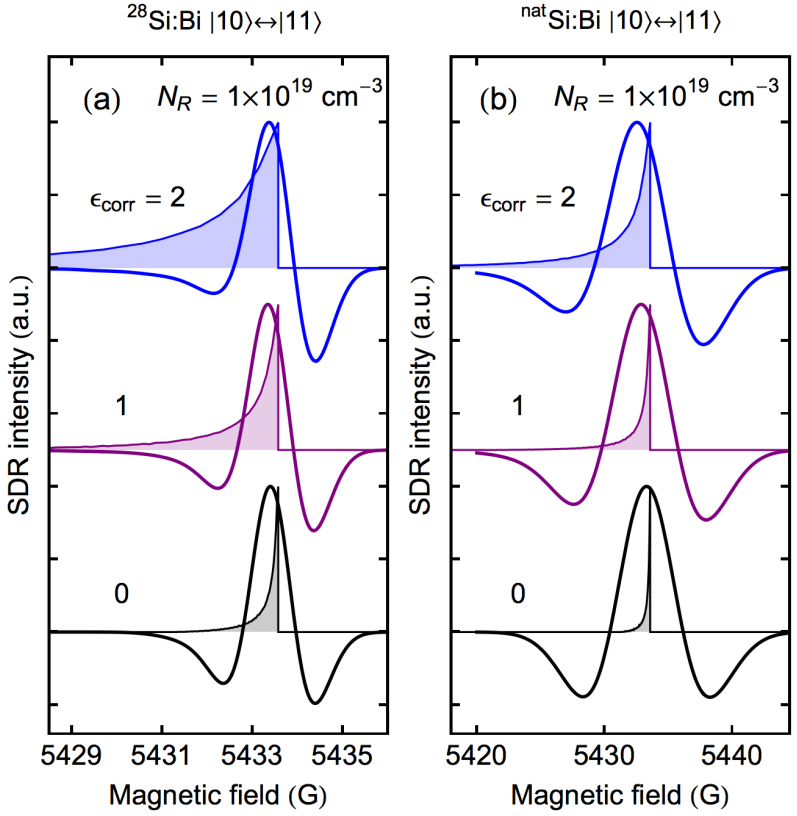

Figure 5-10: Simulated distribution of the $|10\rangle \leftrightarrow |11\rangle$ transition in ^{28}Si:Bi (a) and ^{nat}Si:Bi (b) taking into account only the SDR pair distribution (thin lines) and its convolution with the second derivative of a Gaussian (thick lines) for various two-electron correlation parameters ϵ_{corr}. A larger ϵ_{corr} decreases the hyperfine interaction more in the anti-parallel spin pair configuration, which in turns broadens the distribution of the resonant magnetic field toward low field. The same procedure as for Fig. 5-9 was used for these simulations.

The mixing of atomic orbitals in the present model is assumed to be driven by the long range Coulomb potential of the ionized donor, and the readout center energy

E_R is set at -0.55 eV from the silicon conduction band. The remaining parameter of this model is the two-electron correlation parameter ϵ_{corr} defined in section 5.3.1. It characterizes the mixing of the two-electron molecular orbitals in the spin singlet configuration Ψ_+. The dependence on ϵ_{corr} of the resonant magnetic field is plotted in Fig. 5-10 for the $|10\rangle \leftrightarrow |11\rangle$ transition.

5.4 Comparison of experimental results with simulations

5.4.1 Line positions

At low magnetic field that we employed, the line positions are determined by the two parameters, $g_{_D}$ and A. In section III, I have shown the dependence of the resonant field on the electron density at the donor nucleus, ρ, through the hyperfine interaction. The donor electron g-factor further influences the line positions through both the Zeeman and the hyperfine [Eq. (5.5)] interactions. Because the resonant magnetic field of the HCT_{9-12} is robust against fluctuations in hyperfine A, it allows a precise determination of the g-factor of the donor electron. We measured an effective shift in the donor electron g-factor of +29 ppm in ^{28}Si:Bi (see Table 5.1), which can be qualitatively explained by the second order perturbation theory as follows. For a donor electron non interacting with any readout center, the deviation $\delta g_{_D}^{\infty}$ from the free electron g-factor resulting from the spin-orbit coupling is given by:

$$\delta g_{_D}^{\infty}\mu_B B_z S_z = \sum_{n\neq\chi_{_D}^{\infty}} \frac{\left\langle \chi_{_D}^{\infty}\left|\mathcal{H}_2\right|n\right\rangle \left\langle n\left|\mathcal{H}_2\right|\chi_{_D}^{\infty}\right\rangle}{E_{\chi_{_D}^{\infty}} - E_n} \tag{5.9}$$

where E_n are eigenvalues of the Hamiltonian $\mathcal{H}_0$ and $\mathcal{H}_2 = g_{\mathrm{fe}}\mu_B\, \boldsymbol{S}\cdot\boldsymbol{B} - \lambda\, \boldsymbol{S}\cdot\boldsymbol{l} + \mu_B\, \boldsymbol{l}\cdot\boldsymbol{B}$ with g_{fe} the free electron g-factor, and λ the spin-orbit coupling parameter. Here the electron ground state $\left|\chi_{_D}^{\infty}\right\rangle$ is an eigenstate of $\mathcal{H}_0$, neglecting the readout center potential $V_{_R}^{*}$. However, as shown in section 5.3.1, the electron wave function is modified due to the presence of the readout center. Therefore, the g-factor correction of the donor electron in an SDR pair is $\delta g_{_D} \approx a_1^2 \delta g_{_D}^{\infty} + a_2^2 \delta g_{_R}^{\infty}$ where $\delta g_{_D}^{\infty}$ and $\delta g_{_R}^{\infty}$ are the spin-orbit corrections of the isolated donor and readout center, respectively, and

$a_{1,2}$ are defined in section 5.3.1. Since the g-factor of the isolated readout center $g_R^\infty = 2.005(3)$ (Ref. [20]) is larger than the g-factor of the isolated donor $g_D^\infty = 2.00032$ (see Table 5.1), the weighted average g_D must satisfy $g_D^\infty < g_D < g_R^\infty$. This qualitatively explains the larger effective g-factor of the donor in an SDR pair $g_D = 2.00038(2)$. Moreover, since the hyperfine interaction is proportional to the donor g-factor [Eq. (5.5)], the positive change of +29 ppm in g-factor measured in the SDR spectroscopy of ^{28}Si:Bi can be partly accounted for by the increase in effective hyperfine interaction of +84 ppm. On the other hand, the linewidth of a transition in $^{\text{nat}}$Si:Bi is much larger than in ^{28}Si:Bi due to the inhomogeneous hyperfine interaction with the ^{29}Si nuclear spins. Therefore, the line position where the SDR intensity has a maximum, is shifted toward the mean of the resonant field distribution, away from its maximum (see Fig. 5-9 and 5-10). Thus, the decrease in effective hyperfine of −240 ppm for $^{\text{nat}}$Si:Bi is attributed to a combination of the line asymmetry from the distribution in resonant magnetic field and of the broad linewidth from the inhomogeneous broadening.

The excitation frequency of the HCT_{9-12} (Fig. 5-1) has been determined using the reference values of the donor electron g-factor g_e^{EPR} (Table 5.1). However, the g_e^{SDR} measured by SDR spectroscopy is different from g_e^{EPR}. The resulting deviations in resonant field $\text{HCT}_{9-12}^{\text{EPR}} - \text{HCT}_{9-12}^{\text{SDR}}$ are +0.11 G for ^{28}Si:Bi and +0.35 G for $^{\text{nat}}$Si:Bi. As a consequence, the spectra of Figs. 5-1(b) and 5-1(e) are not exactly at the $\text{HCT}_{9-12}^{\text{SDR}}$, and the sensitivity $\delta B_z/\delta A(B_z = B_{\text{HCT}}^{\text{EPR}})$ is finite: $+3 \times 10^{-8}$ G/MHz for ^{28}Si:Bi and $+8 \times 10^{-8}$ G/MHz for $^{\text{nat}}$Si:Bi. Nevertheless, the line broadening due to these finite sensitivities is much smaller than the magnetic field inhomogeneity and cannot be detected.

5.4.2 Line shapes

The experimental and simulated line shapes can be quantitatively compared in terms of moments m_n defined as:

$$m_n = \int (B - \langle B \rangle)^n \mathcal{I}(B)\, dB \tag{5.10}$$

where $\mathcal{I}$ is the normalized signal intensity and $\langle B \rangle$ is the mean field for this spectrum. The degree of broadening and asymmetry can be represented by the variance m_2 and skewness $\gamma_1 = m_3/m_2^{3/2}$. The simulated values of m_2 and γ_1 for ^{28}Si:Bi are plotted as functions of $N_{_R}$ and $\epsilon_{\rm corr}$ in Figs. 5-11(a) and 5-11(b), respectively. The experimental variance and skewness are, $m_2 = 0.62(5)$ G^2 and $\gamma_1 = -2.0(4)$ for the spin transition $|10\rangle \leftrightarrow |11\rangle$ in ^{28}Si:Bi. These are represented by the red surfaces in Figs. 5-11(a) and 5-11(b). The experimental uncertainties come mainly from a large background after the double-integration of the SDR signal, which is recorded as the second derivative of the sample photoconductivity, necessary for the intensity in Eq. (5.10) to evaluate the moments. The intersection in Fig. 5-11(c) represents the corresponding values for the correlation parameter and the readout center concentration: $\epsilon_{\rm corr} = 1$ and $N_{_R} = 2 \times 10^{19}$ cm^{-3}. Such a high readout center concentration is consistent with the high damage cross-section for energetic bismuth ions and the limited recovery of the crystallinity by the annealing process. The two-electron correlation parameter $\epsilon_{\rm corr} = 1$ obtained in this study is equal to the one estimated for ^{31}P-P$_{\rm b0}$ ($\epsilon_{\rm corr} \approx 1.0$, Ref. [38]), which confirms the localized wave function of the readout center.

For these numerical simulations, I used the experimental linewidth of ^{28}Si:Bi (1.3 G) measured at HCT$_{9-12}$. This rather large linewidth can be explained by the dipole-dipole interaction of the donor and the readout center electron spins for a concentra-

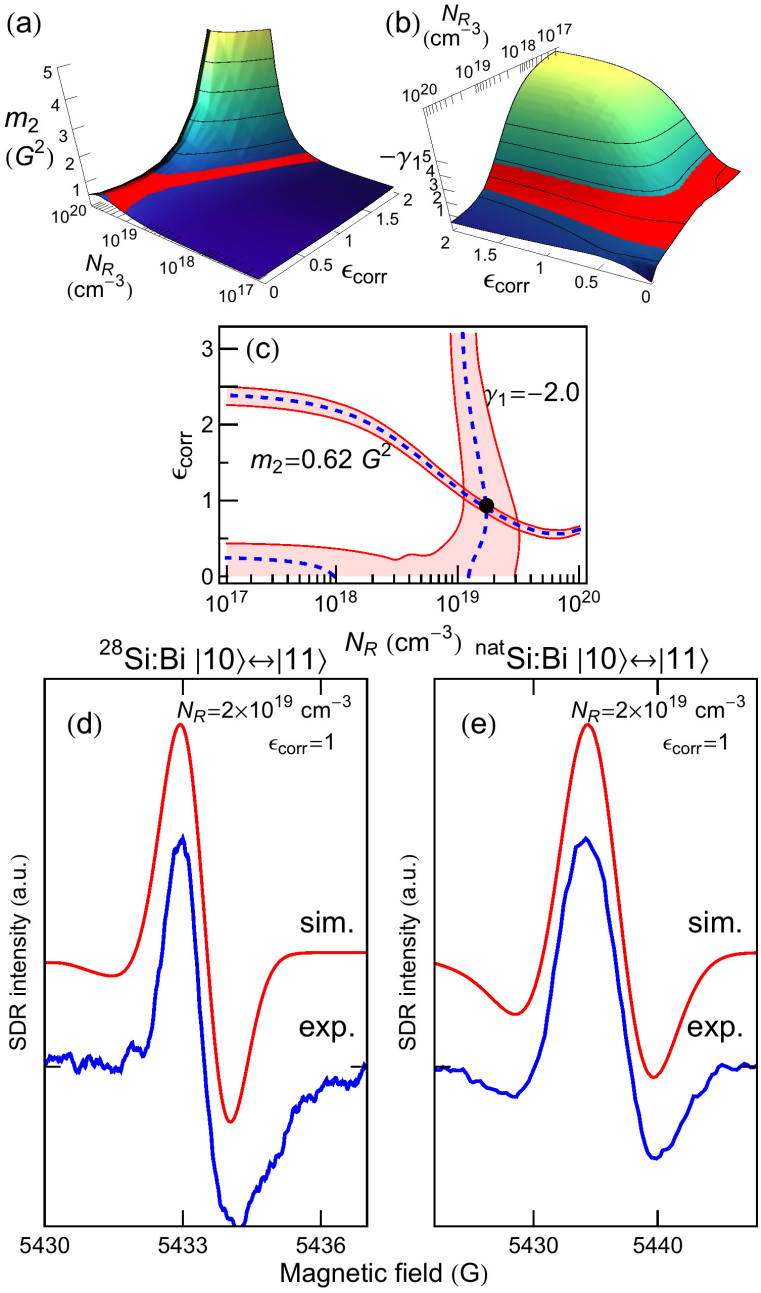

Figure 5-11: Second (a) and third (b) standardized moments (m_2 and γ_1) of the simulated fractional change in the photoconductivity for the transition $|10\rangle \leftrightarrow |11\rangle$. The simulation was performed for ^{28}Si:Bi using the same 1.35 G linewidth as for Fig. 5-9(b) and 5-10(a). The red regions in the both plots represent the experimental values of m_2 and γ_1 and their uncertainty. These two regions are superposed in (c). The intersection of the $m_2 = 0.62$ G^2 and $\gamma_1 = 2.0$ is shown by a filled circle. The simulated line shapes for the pinpointed parameters in (c) of ^{nat}Si:Bi and ^{28}Si:Bi are shown in (d) and (e) (red lines), and compared to the experimental data (blue lines).

tion $N_R \approx 5 \times 10^{18}$ cm^{-3}. Moreover, one can expect a spectral line broadening due to the distribution in the donor electron g-factor. Assuming that this distribution covers a range of ± 93 ppm around $g_D = 2.00049$ for ^{nat}Si:Bi (see Table 5.1), the broadening in the line FWHM, induced by the finite sensitivity $|\delta B_z/\delta g_e|$ (see Table II) at the HCT, should be +0.3 G. As a consequence, the distribution in the donor electron g-factor is negligible for ^{nat}Si:Bi and the FWHM linewidth of the Gaussian for the transition $|10\rangle \leftrightarrow |11\rangle$ is 5.7 G. For ^{28}Si:Bi however, even a smaller distribution of +29 ppm in g-factor is responsible for 0.1 G linewidth broadening (more than 10% of the linewidth measured at the HCT_{9-12}). The 0.1 G contribution of the g-factor distribution to the linewidth is multiplied by the sensitivity ratio $(\delta B_z/\delta g_e)_{|10\rangle\leftrightarrow|11\rangle} \,/\, (\delta B_z/\delta g_e)_{\mathrm{HCT}} = 1.5$. Thus, the Gaussian linewidth to be used in the simulations for ^{28}Si:Bi is 1.35 G. It can be noted that for close pairs ($r < 1\, a_B$), the strong exchange interaction [28] can be neglected since the corresponding SDR intensity for $N_R = 2 \times 10^{19}$ cm^{-3} is below 0.1 % of the total SDR intensity. The above mentioned linewidths together with the N_R and ϵ_{corr} parameters calculated for ^{28}Si:Bi lead to the simulated spectra shown in Fig. 5-11(d) for ^{28}Si:Bi and (e) for ^{nat}Si:Bi. The experimental spectra are also shown below the simulations. The line shapes of the transition $|10\rangle \leftrightarrow |11\rangle$ for both ^{28}Si:Bi and ^{nat}Si:Bi samples are well reproduced. This demonstrates the validity of the presented molecular model for the SDR detection of donors for a wide range of host isotope composition.

Before concluding this section, I would like to point out the work of Morishita *et al.* [39] in which the spectroscopy of ^{28}Si:P was performed using low-field electrically detected magnetic resonance (LFEDMR), a technique similar to SDR. In this work, the authors compared the linewidth of ^{28}Si:P probed by LFEDMR at 160 MHz and by EPR at 9 GHz. No difference in the linewidth (0.1 G) for the $|2\rangle \leftrightarrow |3\rangle$ transition

was observed and the authors concluded that the interaction of the phosphorus donor with the readout center is strong enough to allow the recombination process, but weak enough not to alter the transition linewidth. Yet, the hyperfine structure of the phosphorus donor is only 117 MHz so that its maximum change due to the interaction with the readout center is $\sim$ 13 times smaller for phosphorus than for bismuth. Moreover, the small phosphorus nuclear spin $I = 1/2$ makes the sensitivity $\delta B_z/\delta A$ relatively small: -0.10 G/MHz at 160 MHz for the $|2\rangle \leftrightarrow |3\rangle$. Thus, the effect of the phosphorus donor interaction with its readout center on the magnetic resonance is below the detection limit and the conclusions of Morishita do not contradict the present analysis.

5.5 Hyperfine clock transitions for other group-V donors in silicon

There is no HCT in the EPR transitions of phosphorus donors in silicon. Other group-V donors have $I - 1/2$ HCT. At such points, as discussed in section 5.4.1, the contribution of the g-factor distribution to the linewidth can be evaluated knowing the intrinsic EPR linewidth and extrapolated for an arbitrary transition. In fact, since the broadening due to the distribution in hyperfine (electron density at the donor nucleus) scales with $|\partial\nu/\partial A|$, the contribution to the linewidth calculated in this paper can be extrapolated for any points. The values of $|\partial\nu/\partial A|$ for EPR-allowed transitions of group-V donors in silicon (^{31}P, ^{75}As, ^{121}Sb, ^{123}Sb and ^{209}Bi) are plotted as the line thickness in Fig. 5-12. One can notice that for a given EPR transition, the high-field limit of $\partial\nu/\partial A$ is exactly m_I and, as a consequence, the field sensitivity to the hyperfine interaction is simply written as

$$\frac{\delta B_z}{\delta A} = \frac{h}{g_e\,\mu_e} m_I. \tag{5.11}$$

Also no polarization of the donor spins is required for SDR spectroscopy; only parallel spin pairs remain in the steady state under illumination. However, at low magnetic field, the donor eigenstates are not pure spin states. Thus, for one transition, the fraction of parallel and antiparallel electron spins of an SDR pair modified by magnetic resonance depends on the magnetic field.[20] With such considerations taken into account, the simulated SDR signal intensity for cw-SDR spectroscopy is plotted by the color scale in Fig. 5-12.

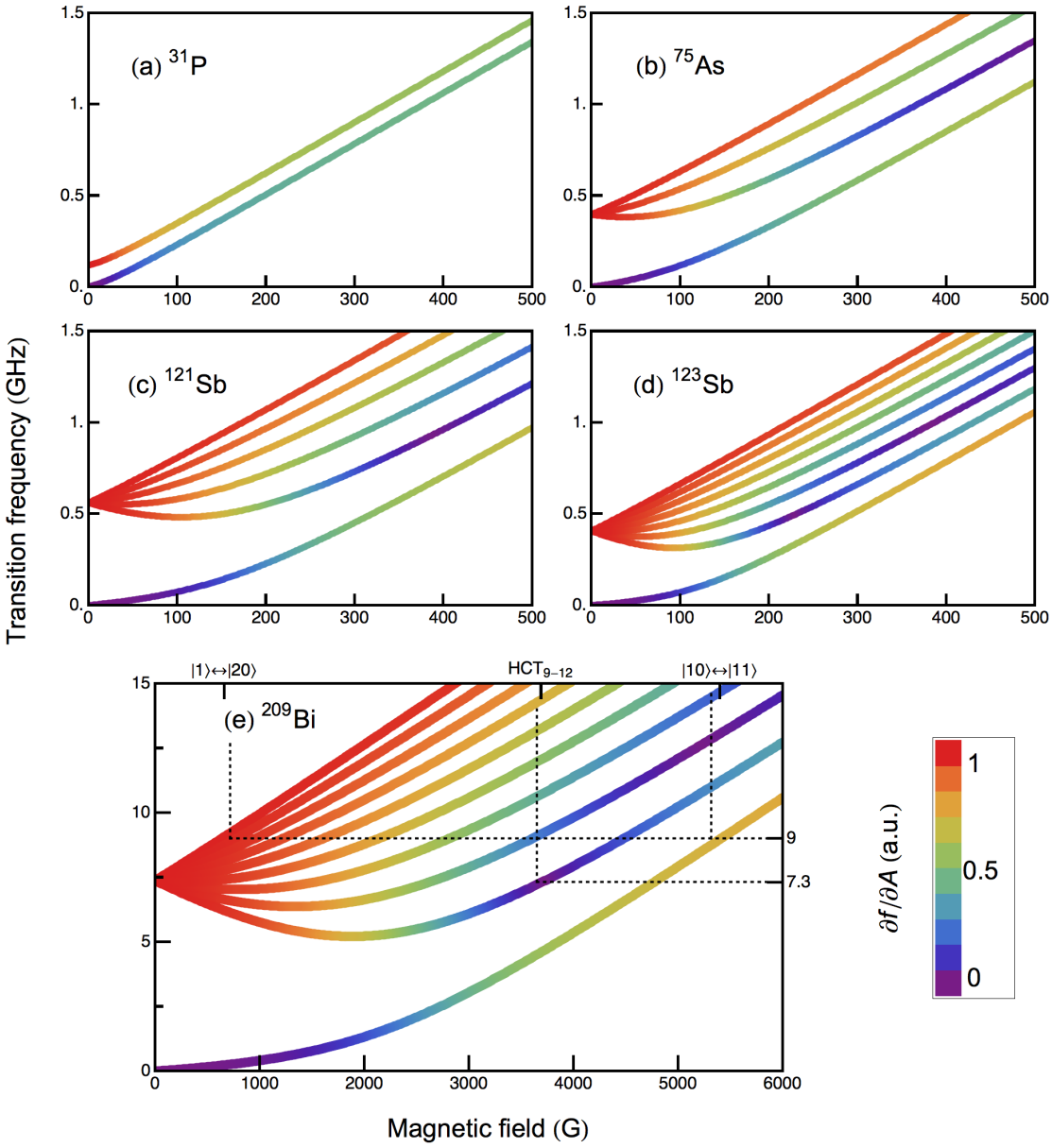

Figure 5-12: EPR transition frequencies of group-V donors in silicon, (a) ^{31}P, (b) ^{75}As, (c) ^{121}Sb, (d) ^{123}Sb and (e) ^{209}Bi. The color represents the absolute $|\partial\nu/\partial A|$ value.

5.6 Summary and conclusions

In summary, we have performed the cw SDR spectroscopy of ^{28}Si:Bi and ^{nat}Si:Bi at 9 and 7 GHz and observed a significant SDR line narrowing at the HCT. The theoretical model proposed in this study for the SDR pair electron distribution reproduces the experimentally obtained line shapes very well. By analyzing the line shape at the HCT, we have shown that the main broadening process in ^{28}Si:Bi is the dipole-dipole interaction between the bismuth donor and the surrounding readout centers. Our results illustrate fundamental properties of hyperfine clock transitions and serve as a stepping stone for further investigations of coupling between microwave circuits and donors in silicon.

Bibliography

[1] M. H. Devoret and R. J. Schoelkopf, Science **339**, 1169 (2013). (Cited on pages 65.)

[2] J. F. Cochran and D. E. Mapother, Phys. Rev. **111**, 133 (1958). (Cited on pages 7, 46, and 65.)

[3] C. Reale, Acta Physica Academiae Scientiarum Hungaricae **37**, 53 (1974). (Cited on pages 7, 46, and 65.)

[4] G. Feher, Phys. Rev. **114**, 1219 (1959). (Cited on pages 29, 31, 46, 65, and 68.)

[5] I. Chiorescu, Y. Nakamura, C. Harmans, and J. E. Mooij, Science **299**, 1869 (2003). (Cited on pages 2, 46, and 65.)

[6] G. W. Morley, M. Warner, A. M. Stoneham, P. T. Greenland, J. van Tol, C. W. M. Kay, and G. Aeppli, Nat. Mater. **9**, 725 (2010). (Cited on pages 7, 31, 46, 50, 65, 68, and 69.)

[7] R. E. George, W. Witzel, H. Riemann, N. V. Abrosimov, N. Noetzel, M. L. W. Thewalt, and J. J. L. Morton, Phys. Rev. Lett. **105**, 067601 (2010). (Cited on pages 7, 46, 50, 65, and 69.)

[8] C. D. Weis, C. C. Lo, V. Lang, A. M. Tyryshkin, R. E. George, K. M. Yu, J. Bokor, S. A. Lyon, J. J. L. Morton, and T. Schenkel, Appl. Phys. Lett. **100**, 172104 (2012). (Cited on pages 43, 46, and 65.)

[9] M. Belli, M. Fanciulli, and N. V. Abrosimov, Phys. Rev. B **83**, 235204 (2011). (Cited on pages 46, 50, and 65.)

[10] G. Wolfowicz, S. Simmons, A. M. Tyryshkin, R. E. George, H. Riemann, N. V. Abrosimov, P. Becker, H. J. Pohl, S. A. Lyon, M. L. W. Thewalt, and J. J. L. Morton, Phys. Rev. B **86**, 245301 (2012). (Cited on pages 65 and 69.)

[11] G. Wolfowicz, A. M. Tyryshkin, R. E. George, H. Riemann, N. V. Abrosimov, P. Becker, H. J. Pohl, M. L. W. Thewalt, S. A. Lyon, and J. J. L. Morton, Nat. Nanotechnol. **8**, 561 (2013). (Cited on pages 8, 32, 65, 66, 68, 69, and 75.)

[12] S. J. Balian, M. B. A. Kunze, M. H. Mohammady, G. W. Morley, W. M. Witzel, C. W. M. Kay, and T. S. Monteiro, Phys. Rev. B **86**, 104428 (2012). (Cited on pages 65 and 66.)

[13] T. Sekiguchi, M. Steger, K. Saeedi, M. L. W. Thewalt, H. Riemann, N. V. Abrosimov, and N. Notzel, Phys. Rev. Lett. **104**, 137402 (2010). (Cited on pages 46 and 65.)

[14] G. W. Morley, P. Lueders, M. H. Mohammady, S. J. Balian, G. Aeppli, C. W. M. Kay, W. M. Witzel, G. Jeschke, and T. S. Monteiro, Nat. Mater. **12**, 103 (2013). (Cited on pages 66.)

[15] M. H. Mohammady, G. W. Morley, and T. S. Monteiro, Phys. Rev. Lett. **105**, 067602 (2010). (Cited on pages 48, 50, 54, 55, 57, and 66.)

[16] E. Abe, A. M. Tyryshkin, S. Tojo, J. J. L. Morton, W. M. Witzel, A. Fujimoto, J. W. Ager, E. E. Haller, J. Isoya, S. A. Lyon, M. L. W. Thewalt, and K. M. Itoh, Phys. Rev. B **82**, 121201 (2010). (Cited on pages 5 and 66.)

[17] W. M. Witzel, M. S. Carroll, A. Morello, L. Cywinski, and S. Das Sarma, Phys. Rev. Lett. **105**, 187602 (2010). (Cited on pages 5 and 66.)

[18] A. M. Tyryshkin, S. Tojo, J. J. L. Morton, H. Riemann, N. V. Abrosimov, P. Becker, H. J. Pohl, T. Schenkel, M. L. W. Thewalt, K. M. Itoh, and S. A. Lyon, Nat. Mater. **11**, 143 (2012). (Cited on pages 5 and 66.)

[19] M. Steger, K. Saeedi, M. L. W. Thewalt, J. J. L. Morton, H. Riemann, N. V. Abrosimov, P. Becker, and H. J. Pohl, Science **336**, 1280 (2012). (Cited on pages 66.)

[20] P. A. Mortemousque, T. Sekiguchi, C. Culan, M. P. Vlasenko, R. G. Elliman, L. S. Vlasenko, and K. M. Itoh, Appl. Phys. Lett. **101**, 082409 (2012). (Cited on pages 37, 66, 88, and 93.)

[21] D. J. Lepine, Phys. Rev. B **6**, 436 (1972). (Cited on pages 37 and 66.)

[22] D. Vion, A. Aassime, A. Cottet, P. Joyez, H. Pothier, C. Urbina, D. Esteve, and M. H. Devoret, Science **296**, 886 (2002). (Cited on pages 4 and 66.)

[23] H. Lyons, Ann. New York Acad. Sci **55**, 831 (1952). (Cited on pages 66.)

[24] P. Kusch, Phys. Rev. **76**, 161 (1949). (Cited on pages 66.)

[25] S. A. Diddams, T. Udem, J. C. Bergquist, E. A. Curtis, R. E. Drullinger, L. Hollberg, W. M. Itano, W. D. Lee, C. W. Oates, K. R. Vogel, and D. J. Wineland, Science **293**, 825 (2001). (Cited on pages 66.)

[26] R. T. Cox, D. Block, A. Herve, R. Picard, C. Santier, and R. Helbig, Solid State Commun. **25**, 77 (1978). (Cited on pages 48, 55, and 71.)

[27] J. M. Lu, F. Hoehne, A. R. Stegner, L. Dreher, M. Stutzmann, M. S. Brandt, and H. Huebl, Phys. Rev. B **83**, 235201 (2011). (Cited on pages 29 and 71.)

[28] M. Suckert, F. Hoehne, L. Dreher, M. Kuenzl, H. Huebl, M. Stutzmann, and M. S. Brandt, Molecular Physics **111**, 2690 (2013). (Cited on pages 72 and 91.)

[29] S. Kimura, H. Ono, T. Ikarashi, and T. Ishikawa, Jpn. J. Appl. Phys. Part 1 - Letters **32**, L1074 (1993). (Cited on pages 72.)

[30] D. K. Wilson and G. Feher, Phys. Rev. **124**, 1068 (1961). (Cited on pages 26 and 72.)

[31] L. Dreher, T. A. Hilker, A. Brandlmaier, S. T. B. Goennenwein, H. Huebl, M. Stutzmann, and M. S. Brandt, Phys. Rev. Lett. **106**, 037601 (2011). (Cited on pages 8 and 72.)

[32] L. Dreher, Ph.D. thesis (2013). (Cited on pages 72.)

[33] J. S. Shah and M. E. Straumanis, Solid State Commun. **10**, 159 (1972). (Cited on pages 18 and 74.)

[34] G. A. Lager, J. D. Jorgensen, and F. J. Rotella, J. Appl. Phys. **53**, 6751 (1982). (Cited on pages 74.)

[35] E. B. Hale and R. L. Mieher, Phys. Rev. **184**, 739 (1969). (Cited on pages 30 and 78.)

[36] H. I. Ralph, G. Simpson, and R. J. Elliott, Phys. Rev. B **11**, 2948 (1975). (Cited on pages 79.)

[37] P. Hertz, Math. Ann. **67**, 387 (1909). (Cited on pages 83.)

[38] E. H. Poindexter, G. J. Gerardi, M. E. Rueckel, P. J. Caplan, N. M. Johnson, and D. K. Biegelsen, J. Appl. Phys. **56**, 2844 (1984). (Cited on pages 89.)

[39] H. Morishita, E. Abe, W. Akhtar, L. S. Vlasenko, A. Fujimoto, K. Sawano, Y. Shiraki, L. Dreher, H. Riemann, N. V. Abrosimov, P. Becker, H. J. Pohl, M. L. W. Thewalt, M. S. Brandt, and K. M. Itoh, Appl. Phys. Express **4**, 021302 (2011). (Cited on pages 91.)

Chapter 6

Conclusion

The main focus of the present thesis was to present the spectroscopy of bismuth donor spins in silicon in the low magnetic field regime, using the magnetic resonance technique namely spin dependent recombination (SDR). The higher sensitivity of this spectroscopic technique with respect to the conventional electron spin resonance (ESR) method allowed for detection of a number of electron spins as low as $< 10^{11}$ in natural silicon.

The damages in crystalline silicon introduced by the bismuth implantation were utilized in a projective spin-to-charge conversion to detect the donor electron and nuclear spins. The technique had an advantage of not requiring any initialization (polarization) step of the donor spins prior to the measurement. It allowed for the electrical readout of the coherent state. Such details were discussed in Chapter 4; the electrical detection of bismuth donor ESR and NMR at arbitrary combinations of magnetic fields and resonance frequencies. Also, the dipolar interaction between electron spins of the donors and readout partners led to the demonstration of SDR based detection of the cross relaxation where the electron spins of the two paramagnetic

centers flip-flopped adiabatically, causing macroscopic changes in photoconductivity of the sample.

The crucial requirement for applying the electrical readout by SDR to quantum information processing is the insensitivity of a donor spin transition to various sources of noise. Chapter 5 investigated the influence of the readout partner defect on the donor hyperfine interaction. To remove the inhomogeneous broadening of the resonance peak caused by the hyperfine interaction of the donor electron spins with ^{29}Si nuclear spins, the isotopically purified ^{28}Si bulk crystal was employed. The spectroscopy of this sample revealed that the donor hyperfine interaction was very sensitive to the electric field because the readout center located at a few donor Bohr radii away could shift the donor hyperfine interaction by 3 MHz (30 times the ESR linewidth in a defect-free crystal). This was confirmed by the molecular model of the electron spin pairs. The comprehension of this phenomenon allowed for cancelation of such perturbation by measuring at the hyperfine clock transition condition.

Unfortunately, the hyperfine clock transition condition did not exist for Bi donors in the low magnetic field regime. However, the thesis presented new tools to theoretically evaluate the effect of an electric field on the Bi donor hyperfine interactions. Understanding of the effect of the electronic noise on the Bi donor spin coherence represents a building stone toward the realization of a silicon-superconducting hybrid quantum computer.